DOCTORAL DISSERTATION

Applying Computational Methods for Processing Thermal Satellite Images of Urban Areas

by

Panagiotis Sismanidis

A dissertation submitted in fulfilment of the requirements
for the degree of Doctor of Philosophy

in the

Department of Process Analysis and System Design
School of Chemical Engineering
NATIONAL TECHNICAL UNIVERSITY OF ATHENS

July, 2018

Doctoral Dissertation

Applying Computational Methods for Processing Thermal Satellite Images of Urban Areas

by Panagiotis Sismanidis

Examined on July 12, 2018 in Athens, Greece and approved by:

Prof. Chris T. Kiranoudis, *School of Chemical Engineering, National Technical University of Athens, Greece*

Dr. Iphigenia Keramitsoglou, *Institute for Astronomy, Astrophysics, Space Applications and Remote Sensing, National Observatory of Athens, Greece*

Prof. Haralampos Sarimveis, *School of Chemical Engineering, National Technical University of Athens, Greece*

Assoc. Prof. Maria Hatzaki, *Faculty of Geology and Geoenvironment, National and Kapodistrian University of Athens, Greece*

Dr. Glynn Hulley, *Jet Propulsion Laboratory, California Institute of Technology, USA*

Dr. Jeffrey C. Luvall, *Marshall Space Flight Center, National Aeronautics and Space Administration, USA*

Assoc. Prof. Vassilios Vescoukis, *School of Rural and Surveying Engineering, National Technical University of Athens, Greece*

The opinions or assertions contained herein are the private opinions of the author and are not to be construed as official or reflecting the views of the School of Chemical Engineering of the National Technical University of Athens (Law 5343/1932, Article 202). — Η έγκριση της παρούσας διδακτορικής εργασίας από την Ανωτάτη Σχολή Χημικών Μηχανικών του Εθνικού Μετσόβιου Πολυτεχνείου δεν υποδηλώνει αποδοχή των απόψεων του συγγραφέα (Νόμος 5343/1932, Άρθρο 202).

"Fortune favours the prepared mind."

Louis Pasteur

Preface

This work was realised in the *Institute for Astronomy, Astrophysics, Space Applications and Remote Sensing* of the *National Observatory of Athens* in Greece. It was done wholly while in candidature for a doctoral degree at the *National Technical University of Athens* in Greece and is the author's own original work, unless stated otherwise. Any use of the works of any other author, in any form, is properly acknowledged at their point of use. Panagiotis Sismanidis was supported by two *A.G. Leventis Foundation* Educational Grants (2017, 2018) and a 2018 *German Academic Exchange Service* (DAAD) short-term Research Grant (Grant Number: 57378443). The research presented in this thesis has been financed by (i) the European Union's Seventh Framework Programme (FP7-REGPOT-2012-2013-1), in the framework of the project BEYOND, under Grant Agreement No. 316210 (BEYOND-Building Capacity for a Centre of Excellence for EO-based monitoring of Natural Disasters); (ii) the Greek Secretariat for Research and Technology (GSRT) Excellence Research Programme (2015-2017) ARISTOTELIS "Environment, Space and Geodynamics/Seismology 2015-2017"; and (iii) the European Union's Horizon 2020 research and innovation programme under grant agreement No. 723757 (PLANHEAT - Integrated tool for empowering public authorities in the development of sustainable plans for low carbon heating and cooling). Typesetting with LaTeX.

Abstract

The *land surface temperature* (LST) is the skin temperature of the boundary layer between the Earth's surface and atmosphere and a key variable in the physics of many terrestrial biophysical processes. Today the only practical way to acquire LST over extensive regions on the surface of the Earth is from space using *thermal remote sensing*. However, due to technical and physical constrains, satellite instruments cannot provide LST datasets with a spatial and temporal resolution that matches the *characteristic scale* of the LST diurnal cycle. A promising solution to this problem is to increase the spatial resolution of temporally-dense *geostationary* LST using *statistical downscaling* methods that rely on LST *disaggregation kernels* available at the desired fine spatial resolution. This thesis contributes to this body of research and is concerned with the identification of LST disaggregation kernels that perform robustly over various times-of-day, land covers and landscapes. To that end, this work demonstrates that multitemporal LST annual climatology data in the form of the *annual cycle parameters* (ACP)—namely the mean annual LST, the yearly amplitude of LST, and the LST phase shift from the spring equinox—offer these attributes. Such LST predictors provide information about the LST spatial distribution at different times-of-day and their use can improve the downscaled LST (DLST) spatial patterns, the DLST accuracy and the DLST diurnal range. This thesis also investigates how LST downscaling, when applied to continuous temporally-dense LST data, affects the *spatiotemporal interrelationships* of the DLST. To achieve this, a quarter-hourly, $4\,\mathrm{km} \times 5\,\mathrm{km}$, three-month long LST time series from SEVIRI (Spinning Enhanced Visible and Infrared Imager) is statistically downscaled to $1\,\mathrm{km} \times 1\,\mathrm{km}$ and (i) the accuracy, reliability, and consistency of the downscaling method; (ii) the shape, size, and location of the DLST spatial patterns; and (iii) the capability of the DLST time series to emulate the diurnal and seasonal characteristics of the original LST data are assessed. The results suggest that the downscaling process can operate consistently and generate DLST data that reproduce the *diurnal cycle* without any artefacts. However the results also reveal that LST downscaling can produce DLST time series

with increased *autocorrelation*. Finally, to facilitate the analysis of temporally-dense geostationary LST datasets, this thesis proposes a method for summarising a LST time series to a set of gap-free *climatological* cycle parameters that describe both the diurnal and annual LST cycles. The proposed method is based on the ACP sine-fitting method and is coupled with a *spatiotemporal fusion* scheme so as to increase the coarse spatial resolution of the geostationary ACP. The results suggest that the derived gap-free parameters are more informative than individual LST images and can provide an *observation-based* spatially consistent background for studying and characterising the thermal behaviour of the surface and also a dataset to support climate classification at a finer spatial resolution.

Περίληψη

Η *επιφανειακή θερμοκρασία εδάφους* είναι η θερμοκρασία του επιφανειακού οριακού στρώματος που διαχωρίζει το έδαφος από την ατμόσφαιρα της Γης. Η συγκεκριμένη μεταβλητή είναι καθοριστικής σημασίας για πολλές βιοφυσικές διεργασίες της Γήινης επιφάνειας και ο μόνος πρακτικός και οικονομικός τρόπος μέτρησής της είναι από το Διάστημα με τη χρήση *δορυφόρων τηλεπισκόπησης*. Εξαιτίας τόσο τεχνολογικών όσο και φυσικών περιορισμών, οι δορυφορικοί θερμικοί δέκτες που βρίσκονται σήμερα σε τροχιά γύρω από τη Γη αδυνατούν να παρέχουν δεδομένα υψηλής χωροχρονικής ανάλυσης, τα οποία είναι αναγκαία για τη μελέτη του ημερήσιου κύκλου της επιφανειακής θερμοκρασίας εδάφους. Μια πολλά υποσχόμενη λύση που έχει προταθεί για να ξεπεραστεί αυτό το πρόβλημα, είναι η χρήση γεωστατικών δορυφορικών δεδομένων υψηλής χρονικής ανάλυσης (1 εικόνα κάθε 15 ή 30 λεπτά της ώρας) και η ενίσχυση της χαμηλής διακριτικής ικανότητας αυτών (2-6 χλμ.), με χρήση στατιστικών μεθόδων χωρικής ενίσχυσης. Οι εν λόγω μέθοδοι έχουν ως στόχο να αναλύσουν τις τιμές επιφανειακής θερμοκρασίας εδάφους των εικονοψηφίδων χαμηλής ανάλυσης στις εικονοψηφίδες υψηλής ανάλυσης που εμπεριέχονται σε κάθε μια από αυτές. Αυτό γίνεται βάσει επικουρικών δεδομένων υψηλής χωρικής ανάλυσης, τα οποία συσχετίζονται στατιστικά με την επιφανειακή θερμοκρασία εδάφους. Η παρούσα διδακτορική εργασία ανήκει σε αυτή την ερευνητική περιοχή και εστιάζει στην αναγνώριση επικουρικών δεδομένων, η χρήση των οποίων δεν περιορίζεται σε συγκεκριμένους τύπους εδαφοκάλυψης και μορφολογίας ή σε ορισμένες χρονικές στιγμές της ημέρας. Ως προς αυτό το ζήτημα, η συγκεκριμένη εργασία υποστηρίζει ότι τα δεδομένα ACP (Annual Cycle Parameters) που αποδίδουν τα κλιματολογικά χαρακτηριστικά του ετήσιου κύκλου της επιφανειακής θερμοκρασίας (δηλαδή την ετήσια μέση επιφανειακή θερμοκρασία, το ετήσιο εύρος της επιφανειακής θερμοκρασίας και τη μετατόπιση φάσης ως προς την εαρινή ισημερία)

προσφέρουν αυτό το πλεονέκτημα. Τα εν λόγω δεδομένα παρέχουν πληροφορίες για τη χωρική κατανομή της επιφανειακής θερμοκρασίας σε διαφορετικές στιγμές της ημέρας και η χρήση τους μπορεί να βελτιώσει την ακρίβεια και τα πρότυπα των χωρικά ενισχυμένων δεδομένων, όπως και την εκτίμηση του ημερήσιου θερμοκρασιακού εύρους από αυτά. Η διατριβή αυτή διερευνά επίσης την επίδραση που έχει η χωρική ενίσχυση στις *χωροχρονικές αλληλοσυσχετίσεις* των παραγόμενων δεδομένων, όταν αυτή εφαρμόζεται σε εκτενείς χρονοσειρές. Η μελέτη του συγκεκριμένου θέματος γίνεται με χρήση μιας χρονοσειράς επιφανειακής θερμοκρασίας εδάφους από τον ευρωπαϊκό δορυφορικό δέκτη SEVIRI (Spinning Enhanced Visible and Infrared Imager), η οποία καλύπτει τρεις μήνες και έχει χρονική ανάλυση ίση με 15 λεπτά της ώρας. Για να μελετηθεί η επίδραση της μεθόδου στις χωροχρονικές αλληλοσυσχετίσεις των δεδομένων, η χωρική ανάλυση της χρονοσειράς ενισχύθηκε από 4 χλμ. σε 1 χλμ. και στη συνέχεια εξετάστηκαν: (α) η ακρίβεια, η αξιοπιστία και η συνέπεια της μεθόδου χωρικής ενίσχυσης· (β) το σχήμα, το μέγεθος και η θέση των χωρικά ενισχυμένων θερμικών προτύπων· και (γ) η ικανότητα της χρονοσειράς που προέκυψε να αναπαραγάγει τα χωροχρονικά χαρακτηριστικά (ημερήσια και εποχιακά) των αρχικών δεδομένων. Τα αποτελέσματα υποδεικνύουν ότι η χωρική ενίσχυση λειτουργεί αξιόπιστα και ότι παράγει δεδομένα που αποδίδουν τον *ημερήσιο κύκλο* της επιφανειακής θερμοκρασίας χωρίς θόρυβο. Ωστόσο, τα αποτελέσματα υποδεικνύουν επίσης ότι η συγκεκριμένη μέθοδος μπορεί να παράγει χρονοσειρές με υψηλή *αυτοσυσχέτιση*. Το τελευταίο μέρος της παρούσας διδακτορικής διατριβής εστιάζει στην ανάλυση χρονοσειρών επιφανειακής θερμοκρασίας από γεωστατικούς δορυφόρους και πιο συγκεκριμένα στην εξαγωγή *κλιματολογικών* παραμέτρων που να αποδίδουν τα χαρακτηριστικά του ετήσιου και του ημερήσιου κύκλου της επιφανειακής θερμοκρασίας. Η προτεινόμενη μέθοδος βασίζεται στη μέθοδο ACP για την εξαγωγή ετήσιων κλιματολογικών παραμέτρων επιφανειακής θερμοκρασίας σε συνδυασμό με μια μέθοδο *χωροχρονικής συγχώνευσης εικόνων*, ώστε η χωρική ανάλυση των τελικών παραγώγων να είναι ενισχυμένη. Τα αποτελέσματα από την εφαρμογή της προτεινόμενης μεθόδου υποδεικνύουν ότι οι κλιματολογικές παράμετροι που προέκυψαν παρέχουν περισσότερες πληροφορίες για τη θερμική συμπεριφορά της Γήινης επιφάνειας συγκρινόμενες με μεμονωμένες μετρήσεις επιφανειακής θερμοκρασίας, όπως και ότι αποτελούν ένα *χωρικά*

συνεχές υπόβαθρο, το οποίο μπορεί να συνδράμει στη μελέτη της Γήινης επιφάνειας και στην πιο λεπτομερή χαρτογράφηση του κλίματος της Γης.

Acknowledgements

This work would not have been possible without the support of my family, friends and colleagues, for which I am grateful. My family was always by my side providing a safe harbour every time I needed one and encouraging me to always try my best. My friends made me happier and eased my mind during stressful periods, while my colleagues encouraged me to constantly improve my skills. My deepest gratitude goes to Iphigenia for putting her trust in me and giving me the freedom to pursue my own research ideas, to Chris for offering me the opportunity to do this PhD, to Benjamin for his warm hospitality and the fruitful discussions we always have, to Kleanthis for his friendship and to Ioanna for her endless support, care, patience and encouragement. I would like also to thank the members of the examination committee for their valuable feedback.

Contents

List of Figures

List of Tables

List of Abbreviations

4A/OP	Automatised Atmospheric Absorption Atlas
ACP	Annual Cycle Parameters
ATC	Annual Temperature Cycle
AVHRR	Advanced Very High Resolution Radiometer
BRDF	Bidirectional Reflectance Distribution Function
CC	Cloud Cover
DEM	Digital Elevation Model
DLST	Downscaled Land Surface Temperature
DN	Digital Number
DOY	Day-of-Year
DTC	Diurnal Temperature Cycle
EM	Electromagnetic
EOSDIS	Earth Observing System Data and Information System
EVI	Enhanced Vegetation Index
FCI	Flexible Combined Imager
FIR	Far Infrared Radiation
GOES	Geostationary Environmental Satellite
GOES-R	Geostationary Environmental Satellite-R Series
GSD	Ground Sampling Distance
GSW	Generalized Split-Window
IAASARS	Institute for Astronomy, Astrophysics, Space Applications and Remote Sensing
IFOV	Instantaneous-Field-of-View
IRIS	Infrared Interferometer Spectrometer
LSA SAF	Land Surface Analysis Satellite Application Facility
LST	Land Surface Temperature
LTE	Local Thermal Equilibrium
MAE	Mean Absolute Error
MAST	Mean Annual Surface Temperature
MMD	Maximum-Minimum Difference
MODIS	Moderate Resolution Imaging Spectroradiometer
MODTRAN	MODerate resolution atmospheric TRANsmission
MSG	Meteosat Second Generation
MTG	Meteosat Third Generation
NASA	National Aeronautics and Space Administration
NCSA	Number of Clear-Sky Acquisitions
NDVI	Normalised Difference Vegetation Index
NEM	Normalised Emissivity Method
NOA	National Observatory of Athens
RMSE	Root-Mean-Square-Error
SEB	Surface Energy Balance
SEVIRI	Spinning Enhanced Visible and Infrared Imager
SRTM	Shuttle Radar Topography Mission
SUHI	Surface Urban Heat Island

SVM	Support Vector Regression Machine
SW	Split-Window
SWIR	Shortwave Infrared Radiation
SZA	Solar Zenith Angle
TIGR	Thermodynamic Initial Guess Retrieval
TIR	Thermal Infrared Radiation
TES	Temperature Emissivity Separation
TOA	Top-of-the-Atmosphere
UHI	Urban Heat Island
USGS	United States Geological Survey
UTC	Coordinated Universal Time
VI	Vegetation Index
VNIR	Visible and Near-Infrared Radiation
VZA	View Zenith Angle
WSA	White Sky Albedo
WVC	Water Vapor Content
YAST	Yearly Amplitude of Surface Temperature

List of Symbols

B, L	blackbody and non-black spectral radiance	$\mathrm{W\,m^{-3}\,sr^{-1}}$
d	day-of-year	
H	altitude	m
k	mass absorption coefficient	$\mathrm{m^2\,kg^{-1}}$
p	pressure	Pa
t	time-of-day	h
T	temperature	°C, K
u	optical depth	
α	absorbance	
ε	emissivity	
θ	zenith angle	°
λ	wavelength	m
Λ	longitude	°
ϱ	density	$\mathrm{kg\,m^{-3}}$
ρ	reflectance	
σ	standard deviation	
τ	transmittance	
ϕ	azimuth angle	°

Chapter 1

Introduction

1.1 Land Surface Temperature: A key surface state variable

The *Land Surface Temperature* (LST; measured in K or °C) is the skin temperature of the *boundary layer* between the Earth's surface and atmosphere and a key variable in the physics of many terrestrial biophysical processes from local through global scales [1]. It results from the physical interactions between the two systems—particularly by the exchange of energy and water between Earth's surface and atmosphere—and is sensitive to local weather conditions, incoming solar radiation (insolation), land cover, soil moisture and topography [2, 3, 4]. As such, knowledge of the LST provides information on the temporal and spatial variations of the *surface equilibrium state* [5] and is useful for measuring and modelling several boundary layer variables (e.g. heat fluxes) and their partitioning across the surface of the Earth [6, 7]. Hence LST data are of fundamental importance in many fields, among which are meteorology, climatology, hydrology, landscape ecology and urban climate [8, 9, 10, 11, 12, 13]; and an essential parameter in land surface models for diagnosing the Earth system behaviour, for constraining the model predictions and also as initialisation and evaluation data [14, 15, 16].

Today the importance of LST is widely recognised by the scientific community and thus there is a strong need for global, consistent and accurate (± 1 K or better) LST datasets that can adequately characterise the LST spatial distribution and temporal evolution [1, 17]. Given the strong heterogeneity of the Earth's surface, which makes the LST to rapidly vary in space and time, the only practical way to acquire such data is from space using *remote sensing* [1, 18]. Lillesand et al. [19] broadly define remote sensing as:

> The science, technology and art of obtaining information about a physical body, area, or phenomenon through the analysis of data acquired by a device that is *not* in contact with the body, area or phenomenon under investigation.

In *Earth science*, remote sensing generally refers to the use of images acquired by instruments onboard spaceborne and airborne platforms (e.g. satellites and aircrafts) that *sense* (i.e measure)—from an overhead perspective—the electromagnetic (EM) radiation emitted or reflected by the surface of the Earth, so as to derive information about its land and water surfaces [20]. To that end, using satellite remote sensing, the LST is inferred from measurements of the surface-emitted EM radiation that are carried out by satellite instruments orbiting the Earth in polar or geostationary orbits. In this context the LST is defined as:

> The mean radiative skin temperature derived from the EM radiation emitted by all the bodies comprising the surface of the Earth into the direction of the satellite instrument.

The history of retrieving the LST from space observations dates back to the 1970s and over the years considerable understanding of the physics of this problem has been achieved [1]. The retrieval of LST from space observations is the subject of the following section, where the theoretical background of this thesis is provided.

1.2 Retrieval of Land Surface Temperatures from Space

1.2.1 Blackbody Radiation and Spectral Emissivity

All physical bodies[1] that comprise the surface of the Earth emit EM radiation. This is because every body that has a *thermodynamic temperature*[2] above $0\,\mathrm{K}$ (equal to $-273.15\,^{\circ}\mathrm{C}$) emits EM radiation due to the random motion[3] of its molecules [23, 24]. The amount of energy and the wavelengths at which it is emitted depend on the temperature of the body and the most effective way to understand this relationship

[1] In this thesis the terms physical body, or simply body, and physical object, or simply object, are used interchangeably.

[2] The thermodynamic temperature is the absolute measure of temperature. It arises from the kinetic energy of the body's molecules (it's zero when these molecules are as close as possible to complete rest) and for an isothermal body it be directly measured by placing a thermometer in physical contact with the body [21, 22].

[3] The random motion of the body's molecules results in excitation (electronic, vibrational, or rotational) due to collisions that is followed by random emission of EM radiation due to decay [23].

is by using the theoretical concept of the *blackbody* [25]. A blackbody is a hypothetical body that absorbs all the radiation it receives and under *thermal equilibrium* conditions emits EM radiation with perfect efficiency and with a spectral distribution (Figure 1.1) that obeys *Planck's law*:

$$B_\lambda(T) = \frac{2hc^2}{\lambda^5} \frac{1}{e^{ch/\lambda kT} - 1} \tag{1.1}$$

where: $B_\lambda(T)$ = blackbody spectral radiance ($\mathrm{W\,m^{-3}\,sr^{-1}}$)
T = thermodynamic temperature (K)
λ = wavelength (m)
h = Planck's constant (equal to $6.626 \times 10^{-34}\,\mathrm{W\,s^2}$)
c = velocity of light (equal to $2.9979 \times 10^{8}\,\mathrm{m\,s^{-1}}$)
k = Boltzmann's constant (equal to $1.38 \times 10^{-23}\,\mathrm{W\,s\,K^{-1}}$)

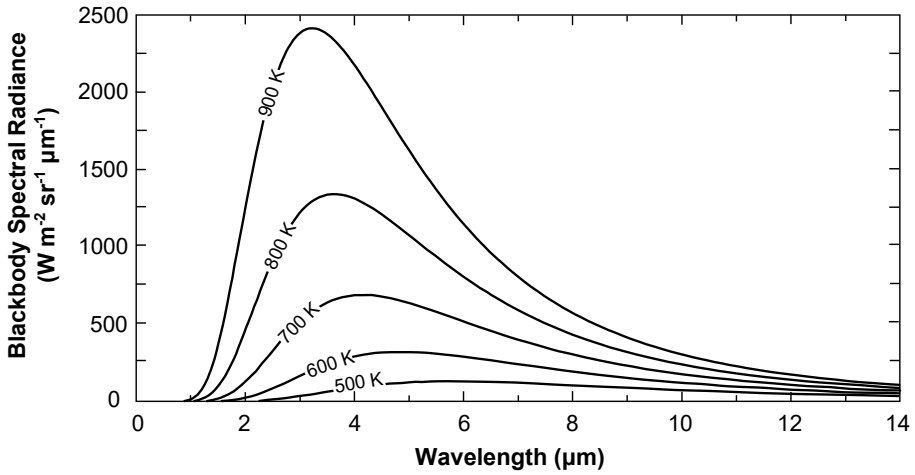

Figure 1.1: Blackbody spectral radiance for various temperatures.

To make this law applicable to real physical bodies, which are not perfect emitters, Eq. 1.1 has to be modified with a wavelength-depended emission efficiency factor called *spectral emissivity* (Eq. 1.2). This factor is defined as the ratio of the *spectral radiance*[4] $L_\lambda(T)$ emitted by a non-black body at temperature T to the radiation $B_\lambda(T)$ emitted by a blackbody at the same temperature and it is unitless.

$$\varepsilon_\lambda(T) = \frac{L_\lambda(T)}{B_\lambda(T)} \tag{1.2}$$

[4]The spectral radiance is a directional quantity and is the radiant flux (i.e. the radiant energy per time) per unit solid angle that crosses a differential surface element that is perpendicular to the axis of the radiation beam. It is usually measured in $\mathrm{W\,m^{-2}\,sr^{-1}\,\mu m^{-1}}$.

Under thermal equilibrium at temperature T, the spectral emissivity of a body is equal to its spectral absorptivity (α_λ), i.e. the fraction of the incident radiation of wavelength λ that it absorbs (for blackbodies $\alpha_\lambda = 1$):

$$\varepsilon_\lambda(T) = \alpha_\lambda(T) \tag{1.3}$$

This equation (Eq. 1.3) is known as *Kirchhoff's law* and describes the intimate relationship between emission and absorption (i.e. good absorbers are good emitters and vice versa) [26]. Kirchhoff's law applies for most common terrestrial surfaces [27] and if coupled with the *energy conservation law* it can relate a body's spectral emissivity to its spectral reflectance (ρ_λ) [3, 28]. In particular, when EM radiation of wavelength λ is incident upon a body, a fraction of it is reflected by its surface (ρ_λ), while the rest is transmitted through it (τ_λ) or absorbed by it (α_λ). Due to the energy conservation law these three fractions must sum to 1:

$$\rho_\lambda + \tau_\lambda + \alpha_\lambda = 1 \tag{1.4}$$

Hence, for an opaque (i.e. $\tau_\lambda = 0$) non-black body, which is in thermal equilibrium with its surroundings, the relationship between its spectral emissivity and reflectance is:

$$\rho_\lambda + \alpha_\lambda = 1 \implies \rho_\lambda + \varepsilon_\lambda = 1 \implies \varepsilon_\lambda = 1 - \rho_\lambda \tag{1.5}$$

Overall the spectral emissivity of a body can range from 0 to 1, with 1 signifying an object with thermal behaviour identical to that of a blackbody and 0 of a perfect reflector (i.e. a whitebody) [20]. Other types of bodies are the *greybodies*, where spectral emissivity is constant and less than 1, and the *selective radiators*, where spectral emissivity varies as a function of wavelength [23]. The physical bodies comprising Earth's surface are mostly selective radiators, where the $8\,\mu m$ to $14\,\mu m$ emissivity ranges between 0.90 and 0.99 (Table 1.1) [29]. Besides wavelength, the emissivity of real bodies also[5] varies with the direction of emission [27]. This is due to the inherent anisotropic[6] emissivity of real bodies and the thermal heterogeneity of complex three-dimensional structures [27].

[5] In addition to wavelength and emission direction, emissivity also depends on the body's temperature T. However for the Earth's environment the dependence on T is usually very small and can be ignored [30].

[6] The maximum amount of emitted radiation is perpendicular to the body's surface and zero tangentially to its surface [6].

Table 1.1: Average 8 µm to 14 µm emissivity for various materials. Source: [19].

Materials	Average emissivity
Clear water	0.98 - 0.99
Healthy green vegetation	0.96 - 0.99
Dry vegetation	0.88 - 0.94
Asphaltic concrete	0.94 - 0.97
Basaltic rock	0.92 - 0.96
Granitic rock	0.83 - 0.87
Dry mineral soil	0.92 - 0.96
Polished metals	0.06 - 0.21

1.2.2 Earth-Emitted Radiation at the Top-of-the-Atmosphere

The Earth's surface has a skin temperature that typically ranges from 258 K to 318 K (the climatological mean is 288 K) and thus emits EM radiation [2, 7]. The surface-emitted radiation covers the *thermal infrared* (TIR; 4 µm to 50 µm) and *far infrared* (FIR; 50 µm to 100 µm) wavelengths and is maximum[7] at about 10 µm [24]. Depending on their emissivity and temperature, different objects on the earth's surface have different radiance spectra. Nevertheless, for the 8 µm to 14 µm TIR wavelengths, where spectral emissivity is mostly uniform and close to unity (Table 1.1), the corresponding spectra resemble very well the spectral radiance of blackbodies. Favourably, these wavelengths coincide with two major *atmospheric windows* that allow surface-emitted TIR radiation to reach the Earth's *top-of-the-atmosphere* (TOA) and escape to space [7]. These atmospheric windows cover the wavelengths between 8.0 µm to 9.2 µm and 10.2 µm to 12.4 µm (Figure 1.2), but clouds[8] and increased air pollution can make them opaque [2, 20].

The TIR radiation emitted over the remaining wavelengths is partially or completely absorbed by various gases in Earth's atmosphere, as shown in Figure 1.2 (scattering in TIR wavelengths is negligible [1]). Among these gases the most important are water vapor (H_2O, it absorbs over all TIR wavelength and especially at 6.5 µm), ozone (O_3, it absorbs strongly at 9.6 µm) and carbon dioxide (CO_2, it absorbs strongly at 15 µm) and to a lesser extent carbon monoxide (CO), nitrous oxide

[7] According to *Wien's displacement law*, the peak emission wavelengths for 258 K, 288 K and 318 K are at 11.23 µm, 10.06 µm and 9.11 µm, respectively.

[8] Clouds absorb much of the surface-emitted TIR radiation and re-emit it downwards almost as blackbodies [2, 7]. Their emission is in accordance with *Stefan-Boltzmann's law* and depends on the cloud-base temperature. This implies that clouds located higher in the atmosphere, such as Altus and Cirrus, emit at lower temperatures than clouds located at lower levels of the atmosphere, such as Stratus and Cumulus [2]. In addition clouds reduce the local amount of incoming solar radiation that reaches Earth's surface. This results in spatially varying heating that is manifested as patchy warm and cool areas in TIR images [23].

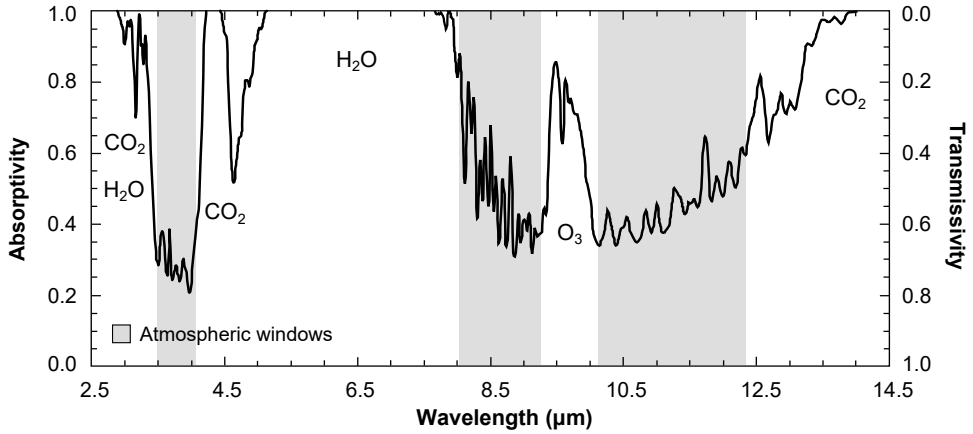

Figure 1.2: Atmospheric transmittance in the $2.5\,\mu\text{m}$ to $14.5\,\mu\text{m}$ spectral region. Source: [25].

(N_2O), methane (CH_4) and nitric oxide (NO) [24]. These gases are primarily found in the lower layers[9] of the atmosphere, namely the *troposphere* ($0\,\text{km}$ to $10\,\text{km}$) and the *stratosphere* ($10\,\text{km}$ to $50\,\text{km}$), which contain together 99.9% of the atmosphere's mass [31]. This implies that the atmospheric absorption of surface-emitted TIR radiation is strongest at these altitudes [2].

EM radiation is not only emitted by the Earth's surface but also by all the levels of the Earth's atmosphere [2]. The spectral distribution of the emitted radiation follows Planck's law (Eq. 1.1) and is consistent with the temperature and spectral emissivity of each atmospheric level [2, 25]. Quantitatively though, the atmospheric emission of EM radiation is most important at the troposphere and stratosphere where the concentration of atmospheric constituents is greatest [2]. The temperature of these two layers is of similar magnitude to the temperature of the Earth's surface and thus the atmospherically-emitted radiation covers the same TIR and FIR wavelengths as the surface-emitted. In particular, the climatological mean tropospheric temperature is approximately $288\,\text{K}$ near the Earth's surface and decreases steadily with height to a temperature of $220\,\text{K}$ at the tropopause (at about $10\,\text{km}$), while the stratospheric temperature is stable from the tropopause to about $20\,\text{km}$ and from that altitude it gradually increases to $270\,\text{K}$ at $50\,\text{km}$ (i.e. the stratopause) [24].

Even though TIR radiation from the Earth's surface and atmosphere cover similar wavelengths, the shape of the corresponding radiance spectra is not the same. This is because the spectral emissivity of atmospheric gases differs considerably

[9] The highest concentration of H_2O is at the lower part of the troposphere between $0\,\text{km}$ to $5\,\text{km}$ and of O_3 at the stratosphere between $15\,\text{km}$ to $30\,\text{km}$ [31, 24]. The %-per-volume concentration of CO_2 is virtually constant up to $60\,\text{km}$ [24].

from that of land materials. In particular, for altitudes below $60\,\mathrm{km}$ where *local thermal equilibrium* (LTE) prevails [31], the atmospheric spectral emissivity is linked to the corresponding spectral absorptivity (Figure 1.2) by Kirchhoff's law (Eq. 1.3). This means that the atmosphere will emit radiation only at the same wavelengths that it absorbs [32], as Figure 1.3 clearly presents.

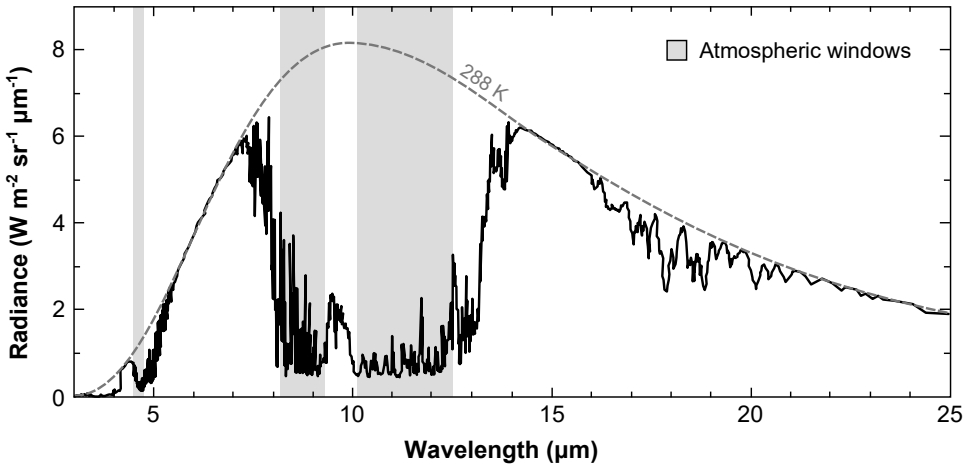

Figure 1.3: Atmospheric emitted radiance spectra (at $288\,\mathrm{K}$) calculated using MODTRAN-5 radiative transfer code for a zenith path from sea level to space through a 1976 US Standard Atmosphere model and a water vapour column with a $1\,\mathrm{cm}$ thickness. The dashed grey line corresponds to the emission spectra of a blackbody at $288\,\mathrm{K}$. Adapted from: [32].

Furthermore, the fact that Earth's atmosphere emits TIR radiation implies that the H_2O, O_3 and CO_2 at the various atmospheric levels will not only absorb TIR radiation emitted by the surface but also TIR radiation emitted by other atmospheric layers that are located at lower or higher altitudes [2]. This process results to a very complex exchange of TIR radiation in Earth's atmosphere, where atmospheric TIR radiation from low altitudes can be absorbed and re-emitted at higher altitudes and vice versa [25]. Moreover, the emission of TIR radiation at all atmospheric levels means that additional power is introduced into the surface-emitted radiation beam as it travels through Earth's atmosphere [33]. In detail, as a radiation beam of radiance L_λ traverses through a non-scattering atmospheric layer of thickness ds that is in LTE and has an absorptivity α_λ, an emissivity ε_λ and a temperature T_p, it changes by the increment dL_λ. This incremental change is due to atmospheric absorption and emission [31] and is equal to:

$$dL_\lambda = dL_\lambda^{\text{absorption}} + dL_\lambda^{\text{emission}} \implies dL_\lambda = -L_\lambda \alpha_\lambda + \varepsilon_\lambda B_\lambda(T_p) \tag{1.6}$$

Because the layer is in LTE, Kirchhoff's law applies. This implies that the medium's spectral emissivity and spectral absorptivity are equal, i.e. $\varepsilon_\lambda = \alpha_\lambda$, and thus Eq. 1.6 becomes:

$$dL_\lambda = [-L_\lambda + B_\lambda(T_p)]\,\alpha_\lambda \tag{1.7}$$

This equation (Eq. 1.7) is known as *Schwarzschild's equation* and shows that, as the radiation beam propagates through the medium, its spectral radiance will increase if $B_\lambda(T_p) > L_\lambda$ or decrease if $B_\lambda(T_p) < L_\lambda$. Nevertheless, the result of both outcomes is the beam's L_λ to approach that of the medium's [31]. However, for wavelengths where α_λ is low, such as the atmospheric window wavelengths (Figure 1.2) under dry weather conditions, the increment dL_λ is so small that its impact on the beam's radiance is minor.

From the above it is clear that the TIR radiation that reaches Earth's TOA (referred to as *outgoing longwave* or *terrestrial* radiation) is a combination of surface-emitted and atmospherically-emitted TIR radiation and thus includes spectral features from both. In addition, because it originates from levels with different temperatures, its spectral distribution will not resemble that of a blackbody at a single temperature, but of a mixture of blackbodies over a range of temperature [25]. An example of an earth-emitted TOA $3\,\mu m$ to $17.5\,\mu m$ radiance spectrum is presented in Figure 1.4a. The data of this figure are from the Nimbus-4 Infrared Interferometer Spectrometer (IRIS) [34] and clearly show the strong absorption of H_2O, O_3 and CO_2 at $6.5\,\mu m$, $9.6\,\mu m$ and $15\,\mu m$, respectively, as well as the high similarity of the earth-emitted spectra with the reference blackbody curves over the $8\,\mu m$ to $9.2\,\mu m$ and $10.2\,\mu m$ to $12.4\,\mu m$ atmospheric windows.

1.2.3 TIR Radiation Measured by Satellites

Satellite sensors measure the TOA TIR radiation along their line of sight in one or more regions of the EM spectrum [1]. According to §1.2.2, for a cloud-free non-scattering atmosphere under LTE, the measured $8\,\mu m$ to $14\,\mu m$ TOA spectral radiance would be a mixture of surface-emitted and atmospherically-emitted TIR radiation. For these wavelengths, this mixed signal can be decomposed into three key components [1], namely the *surface-emitted radiation*, the atmospheric *down-emitted surface-reflected radiation* and the atmospheric *path-emitted radiation*, as presented in Figure 1.5.

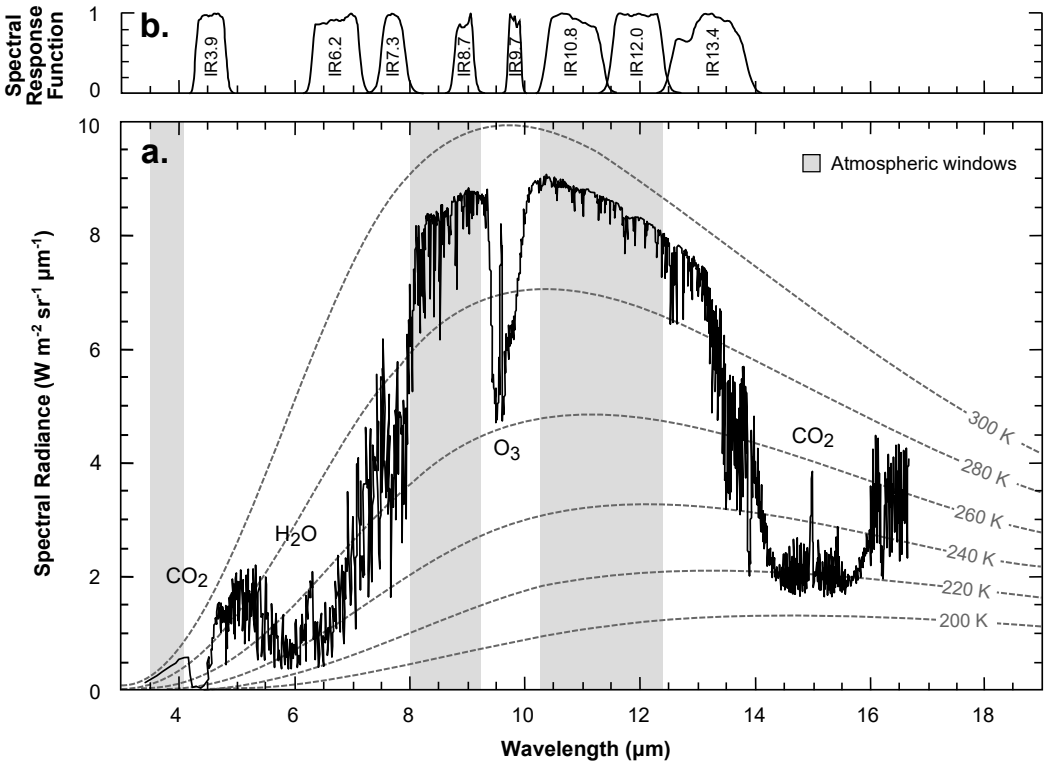

Figure 1.4: **(a)** Example of a $3\,\mu m$ to $17.5\,\mu m$ TOA TIR spectrum measured by the IRIS instrument of Nimbus-4. **(b)** The normalised spectral response functions of the eight MSG-SEVIRI TIR spectral bands.

The surface-emitted radiation (component 1 in Figure 1.5) is the *primary source of information* in thermal remote sensing [25] and is emitted by the upper layer of the Earth's surface. The thickness of this layer varies with wavelength, viewing direction and surface conditions (e.g. wetness, roughness, level of weathering etc.) and for TIR wavelengths it is usually a few millimeters [1]. For a viewing zenith angle (VZA) $\theta \in [0°, 90°]$ and an azimuth angle $\phi \in [0°, 360°]$ (Figure 1.5), the *directional* surface-emitted TIR radiance at TOA ($L_\lambda^{\text{surface}}$) is equal to:

$$L_\lambda^{\text{surf}}(\theta, \phi) = \varepsilon_\lambda(\theta, \phi) B_\lambda(T_s) \tau_\lambda(\theta, \phi, p_s \rightarrow p) \tag{1.8}$$

In Eq. 1.8 $B_\lambda(T_s)$ is the blackbody spectral radiance (Eq. 1.1) of the surface, T_s is the LST, $\varepsilon_\lambda(\theta, \phi)$ is the spectral emissivity (Eq. 1.2) for the viewing direction (θ, ϕ) and $\tau_\lambda(\theta, \phi, p_s \rightarrow p)$ is the spectral transmissivity[10] of the atmospheric layer between the surface of the Earth (at pressure level p_s) and the satellite sensor (at pressure level p)

[10]The spectral transmissivity τ_λ indicates the ability of a medium (in this case the atmosphere) to transmit radiation. It is defined on the basis of *Beer's law*, which states that as radiation passes through a medium, its monochromatic irradiance decreases monotonically with path length [31], and is equal to e^{-u}, where u is the optical depth given by $u = \int_{p_1}^{p_2} \varrho(p) k(p) dp$, ϱ is the density of the absorbing molecules and k_λ the molecules' *mass absorption coefficient* (measured in $\text{m}^2\,\text{kg}^{-1}$).

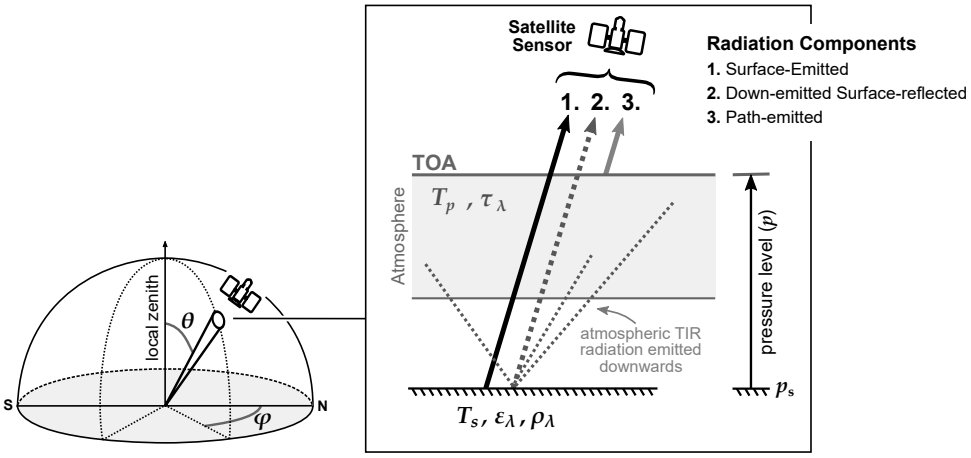

Figure 1.5: The three key radiation components of the earth-emitted $8\,\mu m$ to $14\,\mu m$ TOA TIR radiance. Adapted from: [25].

[27]. The spectral transmissivity adjusts the surface-emitted radiance for *atmospheric attenuation* due to absorption and varies with θ and ϕ [27]. This is because, the path length that the surface-emitted radiation has to travel so as to reach the satellite increases with θ (it is minimum at zenith where $\theta = 0°$), while different azimuth angles might correspond to different profiles of temperature and humidity in the atmosphere.

The down-emitted surface-reflected component (component 2 in Figure 1.5) is the TIR radiation that the atmosphere emits downwards towards the Earth's surface and is then reflected by it and transmitted upwards through the atmosphere to the sensor [25]. The down-emitted radiation arrives to the surface from all the directions (θ', ϕ') of the hemisphere (obstacles can limit the visible sky) and originates from all the levels of the atmosphere. Assuming that there is no azimuthal dependence, the at-surface downwelling spectral radiance ($L_\lambda^{at\downarrow}$) is given by Eq. 1.9 [35].

$$L_\lambda^{at\downarrow} = 2 \int_0^{\frac{\pi}{2}} \int_p^{p_s} B_\lambda(T_p) \frac{\partial \tau_\lambda(\theta', p \to p_s)}{\partial p} \cos\theta' \sin\theta' dp\, d\theta' \tag{1.9}$$

In this equation T_p is the atmospheric temperature at pressure level p and $\tau_\lambda(\theta', p \to p_s)$ the spectral transmissivity of the atmospheric layer between pressure levels p and p_s (the spectral emissivity of the air is not included in Eq. 1.9 because its effect is already contained in τ_λ [36]). Assuming that $\tau_\lambda(\theta', p \to p_s) = \tau_\lambda(\theta, p_s \to p)$ [37], the mean downwelling atmospheric spectral radiance $B_\lambda(T_{at\downarrow})$ for a downward mean atmospheric temperature $T_{at\downarrow}$ can be computed by applying the *mean value theorem*

to $\int_p^{p_s} B_\lambda(T_p)\frac{\partial\tau_\lambda(\theta',p\to p_s)}{\partial p}dp$ [35], which gives:

$$B_\lambda(T_{at\downarrow}) = \frac{1}{1-\tau_\lambda(\theta)}\int_p^{p_s} B_\lambda(T_p)\frac{\partial\tau_\lambda(\theta',p\to p_s)}{\partial p}dp \tag{1.10}$$

Solving Eq. 1.10 for $\int_p^{p_s} B_\lambda(T_p)\frac{\partial\tau_\lambda(\theta',p\to p_s)}{\partial p}dp$ and substituting it in Eq. 1.9, gives the at-surface downwelling spectral radiance expressed[11] as a function of $B_\lambda(T_{at\downarrow})$:

$$L_\lambda^{at\downarrow} = 2\int_0^{\frac{\pi}{2}}[1-\tau_\lambda(\theta)]B_\lambda(T_{at\downarrow})\cos\theta'\sin\theta' d\theta' \implies L_\lambda^{at\downarrow} = [1-\tau_\lambda(\theta)]B_\lambda(T_{at\downarrow}) \tag{1.11}$$

From this radiation only a fraction is reflected by the surface and transmitted through the atmosphere to the sensor. In detail, the reflected fraction is equal to $1-\varepsilon_\lambda$ (as discussed in §1.2.1), while the one that is transmitted through the atmosphere is $\tau_\lambda(\theta,\phi,p_s\to p)$ [27]. Hence, the directional TOA radiance of the down-emitted surface-reflected radiation is equal to:

$$L_\lambda^{\text{refl}}(\theta,\phi) = (1-\varepsilon_\lambda)\tau_\lambda(\theta,\phi,p_s\to p)[1-\tau_\lambda(\theta)]B_\lambda(T_{at\downarrow}) \tag{1.12}$$

This component is generally smaller in magnitude than the surface-emitted component (particularly for wavelengths where ε_λ is close to unity), however on humid days when the total atmospheric water vapour content is high, its contribution to the TOA TIR radiance is considerable [38].

The third and last TOA TIR component is the path-emitted radiation, which corresponds to the TIR radiation emitted by all the level's of the Earth's atmosphere upward to outer space [1]. The TOA spectral radiance of this component can be assumed independent of ϕ [25] and is equal to:

$$L_\lambda^{\text{path}}(\theta) = \int_{p_s}^{p} B_\lambda(T_p)\frac{\partial\tau_\lambda(\theta,p_s\to p)}{\partial p}dp \tag{1.13}$$

Using the mean value theorem with Eq. 1.13, the path-emitted TOA spectral radiance can be expressed as a function of the mean upwelling atmospheric spectral radiance $B_\lambda(T_{at\uparrow})$, where $T_{at\uparrow}$ is the upward mean atmospheric temperature:

$$L_\lambda^{\text{path}}(\theta) = [1-\tau_\lambda(\theta)]B_\lambda(T_{at\uparrow}) \tag{1.14}$$

[11] According to [35], the integration term in the first part of Eq. 1.11 can be solved as: $2\int_0^{\pi/2}\cos\theta'\sin\theta' d\theta' = (\sin\theta')^2|_0^{\pi/2} = 1$.

It is important to note that the magnitude of L_λ^{path} is greater than that of $L_\lambda^{at\downarrow}$ (Eq. 1.11). This is due to the vertical heterogeneity of the atmosphere, which under clear sky conditions, can make the $T_{at\uparrow}$ and $T_{at\downarrow}$ to differ by up to $5\,\text{K}$ [35].

The sum of the surface-emitted, the down-emitted surface-reflected and the path-emitted components makes the directional TOA spectral radiance (L_λ^{TOA}) measured by a satellite sensor from a VZA θ and an azimuth ϕ (for clarity the variables θ, ϕ, p_s and p have been omitted from Eq. 1.15) [1]:

$$L_\lambda^{\text{TOA}} = \underbrace{\varepsilon_\lambda B_\lambda(T_s)\tau_\lambda}_{L_\lambda^{\text{surf}}\text{ (Eq. 1.8)}} + \underbrace{(1-\varepsilon_\lambda)\tau_\lambda(1-\tau_\lambda)B_\lambda(T_{at\downarrow})}_{L_\lambda^{\text{refl}}\text{ (Eq. 1.12)}} + \underbrace{(1-\tau_\lambda)B_\lambda(T_{at\uparrow})}_{L_\lambda^{\text{path}}\text{ (Eq. 1.14)}} \tag{1.15}$$

In Eq. 1.15 and also in Eqs. 1.8 - 1.14, the variables B_λ, ε_λ, τ_λ and L_λ are not monochromatic quantities (i.e. quantities corresponding to a single discrete wavelength) but *band-effective* quantities[12] (i.e. quantities corresponding to a finite spectral bandwidth ranging from λ_1 to λ_2) [1]. This is inevitable because remote sensing instruments cannot sense EM radiation of discrete wavelengths due to technical limitations [25]. Instead they sense EM radiation over a finite spectral range (called *spectral band* or *spectral channel*), with varying sensitivity [1, 25]. For each spectral band i the variation of sensitivity with wavelength is described by the band's *spectral response function* $f_i(\lambda)$ (Figure 1.4b) and each band-effective quantity is calculated as the f_i-weighted average presented in Eq. 1.16 (in this equation X_λ is one of the: B_λ, ε_λ, τ_λ and L_λ) [1].

$$X_i = \frac{\int_{\lambda_1}^{\lambda_2} f_i(\lambda) X_\lambda d\lambda}{\int_{\lambda_1}^{\lambda_2} f_i(\lambda) d\lambda} \tag{1.16}$$

1.2.4 Methods for Retrieving the LST from Satellite Data

The radiative transfer equation given in Eq. 1.15 is fundamental to the remote sensing of LST. This is because, in principle, the LST can be inferred from Eq. 1.15 by solving it for the band-effective Planck function $B_i(T_s)$ and then by inverting this function so as to estimate the LST:

$$T_s = B_i^{-1}\left(\frac{L_i^{\text{surf}}(\theta,\phi) - L_i^{\text{refl}}(\theta,\phi) - L_i^{\text{path}}(\theta)}{\varepsilon_i(\theta,\phi)\tau_i(\theta,\phi,p_s)}\right) \tag{1.17}$$

[12] The use of band-effective values in Eq. 1.15 requires the spectral quantities to be constant within the band's spectral range, which usually holds true since the spectral response functions of most remote sensors are quite narrow [1].

However, Eq. 1.17 is *mathematically underdetermined* and *unsolvable* [1]. This is because if n TOA radiances are measured in n spectral bands the unknowns will always be $n+1$ (i.e. the n spectral emissivities—one for each band—plus the LST) [27]. Hence, to make this problem deterministic one or more of the emissivities must be known or the T_s and ε_i have to be solved simultaneously using various constraints and assumptions [1].

Over the past decades, several methods for retrieving the LST from satellite TIR data have been developed (Table 1.2). These methods can be divided into two broad categories, namely the methods where the spectral emissivities are *known* and the methods where they are *unknown* [1]. The LST retrieval methods of the first category are the single-channel methods, the multi-channel methods and the multi-angle methods; while those of the second category are the stepwise methods, the two-temperature method, the physics-based day/night method, the greybody emissivity method, the temperature emissivity separation (TES) method, the iterative spectrally smooth TES and the linear emissivity constraint TES (the basic concept behind each method is given in Table 1.2) [1]. From these the most widely-used are the *single-channel* methods, the *multi-channel* methods and the *temperature emissivity separation* method.

The single-channel methods estimate the LST by solving Eq. 1.17 using a priori knowledge about the band-effective emissivity and the atmospheric quantities [1]. The emissivity is most usually obtained from the corresponding visible, near-infrared (VNIR) and shortwave infrared (SWIR) spectral bands using semi-empirical methods [27], such as the classification-based method, which assumes a constant emissivity within a particular land cover class (e.g. [39, 40]). The atmospheric information on the other hand is retrieved from concurrent and collocated atmospheric vertical profiles using a radiative transfer model (RTM), such as the MODerate resolution atmospheric TRANsmission (MODTRAN) model. These profiles can be obtained from ground-based atmospheric radiosoundings, satellite vertical sounders or from numerical weather prediction models, which is the most practical option [1]. Because the acquisition of such data is not easy, empirical single-channel methods that do not require atmospheric profiles but more easily obtainable variables such as the near-surface air temperature (T_{air}) and the water vapor content[13] (WVC)

[13]The WVC is used to approximate the band-effective transmittance using an empirical linear function that relates them [1].

Table 1.2: Methods for retrieving the LST from satellite TIR data. Source: [1].

LST Retrieval Method	Basic Concept
with known emissivities:	
Single-channel	Use of Eq. 1.17
Multi-channel or Split-window	LST estimated as a combination of the brightness temperatures of two adjacent TIR bands.
Multi-angle	The LST is assumed independent of VZA and the atmosphere horizontally uniform and stable.
with unknown emissivities:	
Stepwise	Two-step algorithms that first retrieve the emissivities using (semi-) empirical methods and then the LST using a single-channel, multi-channel or multi-angle method.
Two-temperature	By using multiple almost simultaneous acquisitions and assuming the emissivity invariant, the number of unknowns can be reduced and Eq. 1.17 can become solvable.
Physics-based day/night	Using daytime and nighttime TIR data, the number of unknowns is reduced by assuming that the day/night ε_λ is the same.
Greybody emissivity	Assuming that the emissivity is independent of wavelength and using at least two spectral bands the number of unknowns can be reduced. This method is better-suited for hyperspectral data.
TES	This method relies on an empirical relationship between the spectral contrast and the minimum emissivity to increase the number of equations (equivalent to reducing the number of unknowns) so that the undetermined retrieval problem becomes deterministic.
Iterative spectrally smooth TES	The best estimates of the LST and LSE should be obtained when the spectral smoothness of the retrieved LSE is maximized.
Linear emissivity constraint TES	This method assumes that the emissivity spectrum can be divided into M segments and that the emissivity in each segment varies linearly with λ.

have also been developed (e.g. [41]). Overall, single-channel methods offer the great advantage that they can be applied to satellite sensors with only one TIR spectral band [42]. However, their performance can be poor if the employed spectral emissivity and atmospheric data are inaccurate. In particular a 1% uncertainty in ε_i can lead to a $0.4\,\mathrm{K}$ LST error [39], while a 0.5%-2.0% uncertainty in the RTM can lead to a LST error of $0.4\,\mathrm{K}$ to $2.0\,\mathrm{K}$ [1].

The multi-channel methods, also known as *split-window* (SW) methods, require the use of at least two adjacent spectral bands in the $10.2\,\mu\mathrm{m}$ to $12.4\,\mu\mathrm{m}$ atmospheric window (Figure 1.2) and estimate the LST as a combination of the bands' *brightness temperatures*[14] ($T_{b,i}$) [1]. Because the difference between the downward and upward

[14]The brightness temperature $T_{b,i}(\theta, \phi)$ is the directional temperature retrieved by equating the measured spectral TOA radiance with the integral over wavelength of the Planck's Law (Eq. 1.1) times the sensor spectral response f_i for the spectral band i. In essence, it is the temperature of a blackbody that would have the same radiance as the TOA radiance actually measured with the satellite sensor [22].

mean atmospheric temperature in these wavelengths is less than 1 K [24], it can be assumed that $T_{at\downarrow} \approx T_{at\uparrow} = T_{at}$ and thus Eq. 1.15 for spectral band $i = 1$ and $i = 2$ becomes:

$$L_1^{\text{TOA}} = B_1(T_{b,1}) = \varepsilon_1 B_1(T_s)\tau_1 + (1-\tau_1)[(1-\varepsilon_1)\tau_1 + 1]B_1(T_{at}) \tag{1.18a}$$

$$L_2^{\text{TOA}} = B_2(T_{b,2}) = \varepsilon_2 B_2(T_s)\tau_2 + (1-\tau_2)[(1-\varepsilon_2)\tau_2 + 1]B_2(T_{at}) \tag{1.18b}$$

The objective of the SW method is to eliminate the variable T_{at} by combining Eqs. 1.18a and 1.18b [24]. The first step to achieve this is by substituting all the instances of Planck's radiance function in Eqs. 1.18a and 1.18b with the *first order Taylor expansion* of $B_i(T_j)$, which is given in Eq. 1.19 (T_j is one of the $T_{b,1}$, $T_{b,2}$, T_s and T_{at}) [35, 37].

$$B_i(T_j) = B_i(T) + \frac{\partial B_i(T)}{\partial T}(T - T_j) \tag{1.19}$$

This is an appropriate approximation for the $10.2\,\mu\text{m}$ to $12.4\,\mu\text{m}$ spectral region, since the relationship between temperature and blackbody spectral radiance for these wavelengths is almost linear (Figure 1.6) [25]. The application of the Taylor's expansion is critical for deriving the SW algorithm because it expresses the radiances $B_i(T_j)$ in terms of the radiance $B_i(T)$, where T is fixed (this variable is usually set to be the $T_{b,1}$) [35]. After the linearization of the $B_i(T_j)$ the next step is to combine the updated Eqs. 1.18a and 1.18b and eliminate T_{at}. This after some analysis[15] gives:

$$T_s = A_0 + A_1 T_{b1} + A_2 \left(T_{b1} - T_{b1}\right) \tag{1.20}$$

where A_κ ($\kappa = 1, 2, 3$) are the SW coefficients. Eq. 1.20 is a typical formulation of a linear two-band SW algorithm. Nevertheless, over the years, non-linear SW algorithms (e.g. [43]) or algorithms that use three or more spectral bands (e.g. [44, 45]) have also been developed. The SW coefficients of Eq. 1.20 are sensor-specific and pre-determined either by regressing the simulated satellite data with a set of atmospheres and surface parameters or empirically by comparing the satellite data against in-situ LST measurements [1]. Over the years different parameterisations (linear or non-linear) of the A_κ have been proposed that are based on the spectral response functions of the employed spectral bands, the band-effective emissivities,

[15] The interested reader is referred to [35], where the mathematical analysis for deriving Eq. 1.20 from Eqs. 1.18a and 1.18b is presented in detail.

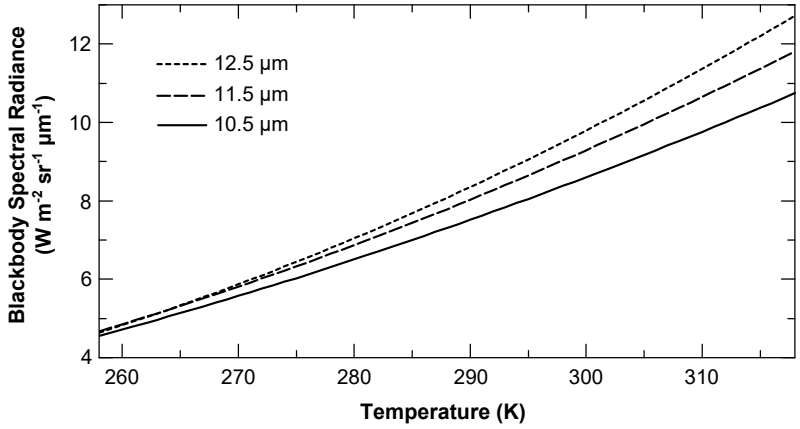

Figure 1.6: The change in blackbody spectral radiance with temperature at $10.5\,\mu\mathrm{m}$, $11.5\,\mu\mathrm{m}$ and $12.5\,\mu\mathrm{m}$.

the WVC (used for empirically determining τ_i) and the VZA [1, 35]. To that end radiative transfer simulations have shown that the dependance of the A_κ on the VZA must not be omitted, especially for satellite sensors with large scan swaths, such as the Moderate Resolution Imaging Spectroradiometer (MODIS) where θ can range between -55° and $+55^\circ$ [30]. For this reason the MODIS operational LST product (i.e. the MOD11 from Terra and the MYD11 from Aqua) uses a *generalised split-window* (GSW) algorithm that employs a set of θ-dependent coefficients. These coefficients have been derived using a regression analysis of RTM simulations for various values of WVC, lower boundary temperature, and surface temperature [30]. The optimisation of the SW coefficients for θ and WVC has increased the accuracy of the LST retrieveal considerably, especially for $\theta > 45^\circ$ and increased WVC values, but its success still depends on how accurately the band-effective emissivities are known (for MOD11 and MYD11 they are retrieved using the classification-based method of [40]).

Finally, the TES algorithm [46], which purpose is to *simultaneously* retrieve the T_s and ε_i from multispectral or hyperspectral thermal data, relies on an empirical relationship between the spectral contrast of emissivity and the minimum emissivity so as to increase the number of equations and make the retrieval problem deterministic [1]. The TES algorithm consists of three modules: the Normalised Emissivity Module (NEM), the Ratio Module, and the Maximum-Minimum Difference (MMD) Module; and takes as input the atmospherically corrected[16] (for τ_λ and L_i^{path}) TIR

[16]The required atmospheric quantities can be retrieved from a collocated and concurrent atmospherical vertical profile and a RTM [47], as done for the single-channel methods.

radiances of $i \geq 3$ spectral bands (L_i^{corr}, Eq. 1.21).

$$L_i^{\text{corr}} = \underbrace{\varepsilon_i B_i(T_s)}_{L_{s,i}} + (1-\varepsilon_i) B_i(T_{at\downarrow}) \tag{1.21}$$

The role of the first module (i.e. the NEM module) is to estimate an initial LST, referred to as NEM temperature (T_{NEM}), and a ε_i spectrum [1]. In particular, T_{NEM} (Eq. 1.22) is the maximum temperature retrieved from each spectral band i by inverting Planck's law (Eq. 1.1) and using as input (i) a reference emissivity (ε_{max}) and (ii) the surface-emitted atmospherically-corrected radiance $L_{s,i}$, derived from Eq. 1.21 as the difference between L_i^{corr} and $(1-\varepsilon_{\text{max}})B_i(T_{at\downarrow})$ [48].

$$T_{\text{NEM}} = \max\left(T_i\right) = \max\left[\frac{c_2}{\lambda_i}\left[\ln\left(\frac{c_1 \varepsilon_{\text{max}}}{\pi L_{s,i} \lambda_i^5} + 1\right)\right]^{-1}\right] \tag{1.22}$$

In Eq. 1.22 ε_{max} is 0.99 for vegetated surfaces, snow and water and 0.96 for rocks and sands [46, 48]; whereas c_1 and c_2 (known as the *first* and *second radiation constants*, respectively) are equal to $c_1 = 2hc^2 = 1.911 \times 10^8\,\text{W}\,\text{m}^{-2}\,\text{sr}^{-1}\,\mu\text{m}^{-4}$ and $c_2 = ch/k = 1.439 \times 10^4\,\mu\text{m}\,\text{K}$, respectively (see §1.2.1 for explanations). After the calculation of T_{NEM}, the next operation is the estimation of the NEM emissivities ($\varepsilon_i^{\text{NEM}}$) using Eq. 1.23.

$$\varepsilon_i^{\text{NEM}} = \frac{L_{s,i}}{B_i(T_{\text{NEM}})} \tag{1.23}$$

The new emissivities are then used to re-estimate $L_{s,i} = L_i^{\text{corr}} - (1-\varepsilon_i^{\text{NEM}})B_i(T_{at\downarrow})$ and then T_{NEM} [48]. This process is repeated until convergence, which is determined if the change in $L_{s,i}$ between two consecutive iterations is less than a predefined threshold or if the number of iterations exceeds a predefined limit [46]. The NEM emissivities of the final iteration are then input to the second module of TES (i.e. the SR module), where they are divided by their average (Eq. 1.24).

$$\beta_i = \frac{\varepsilon_i^{\text{NEM}}}{\frac{1}{n}\sum_i^n \varepsilon_i^{\text{NEM}}} \tag{1.24}$$

The derived ratios β_i (typically ranging from 0.75 to 1.32 [46]) describe well the shape of the emissivity spectrum [1] and are used for estimating the actual ε_i in the third and last module of TES, i.e. the MMD module. The first operation of the MMD

module is to calculate the spectral contrast (i.e. the MMD) of the β_i using Eq. 1.25.

$$\text{MMD} = \max(\beta_i) - \min(\beta_i) \tag{1.25}$$

The derived MMD values are then related to the the minimum emissivity (ε_{min}) of the data using the *empirical* power-law relationship of Eq. 1.26, which is also known as the *TES calibration curve* [47].

$$\varepsilon_{\text{min}} = A_1 - A_2\,\text{MMD}^{A_3} \tag{1.26}$$

The coefficients A_κ ($\kappa = 1, 2, 3$) of this equation (Eq. 1.26) are determined by regression analysis using laboratory and field emissivity spectra from rocks, soils, vegetation, water and snow/ice and are sensor specific (Figure 1.7) [46, 48]. The final

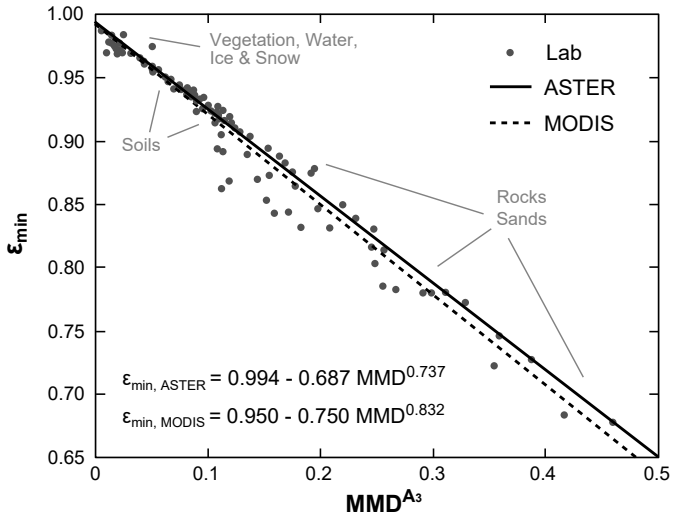

Figure 1.7: The TES empirical power-law relationship between spectral contrast (MMD^{A_3}) and minimum emissivity derived from laboratory measurements. The TES calibration curves for ASTER and MODIS are also included. Adapted from [47].

operation of TES is the calculation of the emissivities ε_i and the retrieval of LST. In detail the emissivities ε_i are calculated from the ε_{min} and the corresponding β_i using Eq. 1.27:

$$\varepsilon_i = \beta_i \left[\frac{\varepsilon_{\text{min}}}{\min(\beta_i)} \right] \tag{1.27}$$

while the LST from the spectral band i^*, for which Eq. 1.27 returned the maximum emissivity. To that end, the estimation of the LST is performed using Eq. 1.28, which is the inverse form of Planck's Law (Eq. 1.1). The input to Eq. 1.28 are the corresponding atmospherically-corrected surface-emitted radiance $L_{\text{s},i^*} =$

$L_{i^*}^{\text{corr}} - (1-\varepsilon_{i^*})B_{i^*}(T_{at\downarrow})$ and the TES-derived emissivity ε_{i^*}.

$$T_s = \frac{c_2}{\lambda_{i^*}} \left[\ln \left(\frac{c_1 \varepsilon_{i^*}}{\pi L_{\text{s},i^*} \lambda_{i^*}^5} + 1 \right) \right]^{-1} \tag{1.28}$$

Numerical simulation and field validations have shown that TES retrieves the LST and the emissivities with an accuracy of about $\pm 1.5\,\text{K}$ and ± 0.015, respectively, when the atmospheric effects are accurately corrected [1, 29]. However, for low spectral contrast surfaces (e.g. graybodies) the performance of TES can be compromised [48].

1.2.5 Physical Interpretation of Satellite Derived LST

The interpretation of satellite derived LST is not straightforward and depends on the application and the method of measurement [18]. To that end the key question that should be considered is: What does the surface-emitted TIR radiance in each picture element (*pixel*) of the acquired image matrix represents?

During the data acquisition process, the satellite sensor senses an area on the ground, which size and shape are determined by the sensor's instantaneous field-of-view (IFOV), the VZA, the satellite's altitude and speed, and the topography of the scene. If the satellite was stationary the shape of the sensed area (i.e. the projection of the IFOV on the ground) would be a circle for $\theta = 0^\circ$ and an ellipse for $\theta \neq 0^\circ$ (its size would increase with $|\theta|$). In reality, however, the satellite is never still but moves forward as it scans the surface of the Earth. This fact makes the area that is actually sensed to be slightly elongated in the along-track direction and also consecutively sensed areas to overlap (due to sensor array design there is also an overlap in the along-scan direction) [49]. The latter is particularly important because it implies that adjoined pixels are positively *spatially autocorrelated* and also that the surface variation of the scene, as represented by the satellite data, is less pronounced than it is in reality [6, 49].

For each sensed area the satellite sensor gives a single response that is allocated to the corresponding pixel. This response corresponds to the spectrally (Eq. 1.16), temporally and spatially weighted average [50] of the upwelling radiation emitted by the skin surface of all the objects within the sensed area and is influenced by (i) the location, temperature, shape, size and orientation of each object (in general objects near the center of the sensed area contribute more than those near the edges [49]); (ii) their arrangement and heterogeneity; and also (iii) by variations in the topography,

and the atmosphere [6]. If all the objects within the sensed area are of the same material and have the same temperature, then the corresponding pixel is characterised as *homogeneous* and *isothermal* and the sensor response can be related to a blackbody distribution (Figure 1.1) at the same temperature. On the other hand, if the objects on the sensed area are of different material and at different temperatures—which is the most common case—then the corresponding pixel is characterised as *heterogeneous* or *mixed* and the sensor response *cannot* be related to a unique blackbody distribution [22]. This is because the radiance of an ensemble of objects at different temperatures depends on its temperature distribution and cannot be represented by a single blackbody at a single temperature that would yield the same radiance at all wavelengths. Hence, the LST[17] of homogeneous and isothermal pixels is *equivalent* to the thermodynamic temperature of the sensed surface, while for mixed pixels it is only an approximation specific to the sensing conditions (i.e. the spectral band, the VZA, the IFOV etc.) [1, 27].

1.3 Motivation and Problem Statement

The distance between two consecutive pixel centers on the ground is called Ground Sampling Distance (GSD) and is directly related to the *spatial resolution* of the image data, i.e. the size of the smallest object that can be reliably detected[18] against a spectrally contrasting background [6]. Based on the spatial resolution, satellite instruments are classified into four groups: the low or coarse resolution systems (GSD $> 1\,\mathrm{km}$), the moderate resolution systems ($0.1\,\mathrm{km} <$ GSD $< 1\,\mathrm{km}$), and the high ($10\,\mathrm{m} <$ GSD $< 100\,\mathrm{m}$) and very high (GSD $< 5\,\mathrm{m}$) resolution systems. In addition, satellite instruments are also classified into groups according to the temporal frequency with which they sense the same location on the surface of the Earth. This frequency is referred to as *satellite revisit time* and is controlled by the orbital characteristics of the satellite platform and the engineering of the satellite instrument (e.g. the swath width). The satellite revisit time can range from several days, to several hours, to a couple of minutes and determines the *temporal resolution* of the data.

The spatial and temporal resolution (referred to as *observational scale* [51]) governs the information content of the data and determines their usage. This is because,

[17] In layman's terms, the LST can be considered as a measure of how hot or cold the surface feels to the touch.

[18] For a homogeneous feature to be detected, its size generally has to be equal to or larger than the resolution cell.

depending on the observation scale, the surface heterogeneity is manifested differently in the image data. This implies that a physical process may appear homogeneous at one observational scale but heterogeneous at another [6]. Hence, to detect and monitor a terrestrial biophysical process using remote sensing, the spatial and temporal resolution of the data has to match—or be finer than—the space and time intervals over which the dominant spatiotemporal patterns of the process emerge [51]. These space and time intervals are referred to as the *characteristic scale* of the process and for LST they are in the order of meters and minutes, respectively [39, 52]. This is because the LST can vary by as much as $10\,\mathrm{K}$ over a few meters due to shadowing and topographic effects; or by several kelvins over a couple of hours due to the *diurnal cycle* of energy and water [2]. Hence, to adequately capture the spatial distribution and temporal evolution of the LST, remote sensing data should have a high spatial and a high temporal resolution [53]. However, due to technical constraints, satellite instruments are unable to provide such data [54]. This is because the spatial and temporal resolutions are *anticorrelated* (Figure 1.8 and Table 1.3) and thus satellite instruments can only provide LST data with either high spatial but low temporal resolution (e.g. semimonthly acquisitions with a GSD $\leq 120\,\mathrm{m}$); or LST data with moderate spatial and temporal resolution (e.g. two images per day with a GSD $\approx 1\,\mathrm{km}$); or LST data with low spatial but high temporal resolution (e.g. half-hourly acquisitions with a GSD $\geq 3\,\mathrm{km}$). The first two groups (group 1 and 2 in Figure 1.8) correspond to instruments onboard *polar-orbiting sun-synchronous* satellites, while the third to *geostationary* satellites. The former are satellites that orbit the Earth at altitudes that range from $300\,\mathrm{km}$ to $1400\,\mathrm{km}$ and pass over a certain area at the same solar time each time, while the latter are satellites that orbit the Earth above the equator (at $36\,000\,\mathrm{km}$) with an orbital period and direction equal to the Earth's rotational period and direction [23]. From these three groups only instruments onboard geostationary satellites can monitor the diurnal cycle of LST [55]. Hence, it is highly desirable to explore effective ways for increasing the spatial resolution of such data. One way to achieve this is by statistically disaggregating the LST to finer GSD, using information from auxiliary datasets that are available at the desired fine spatial resolution. This statistical approach is known as *LST downscaling* (also referred to as *thermal sharpening*) and is well-suited for use with LST from geostationary satellite instruments [55, 56]. Since the mid to late 2000s, LST downscaling has seen significant growth mainly due to the mounting requirements for monitoring

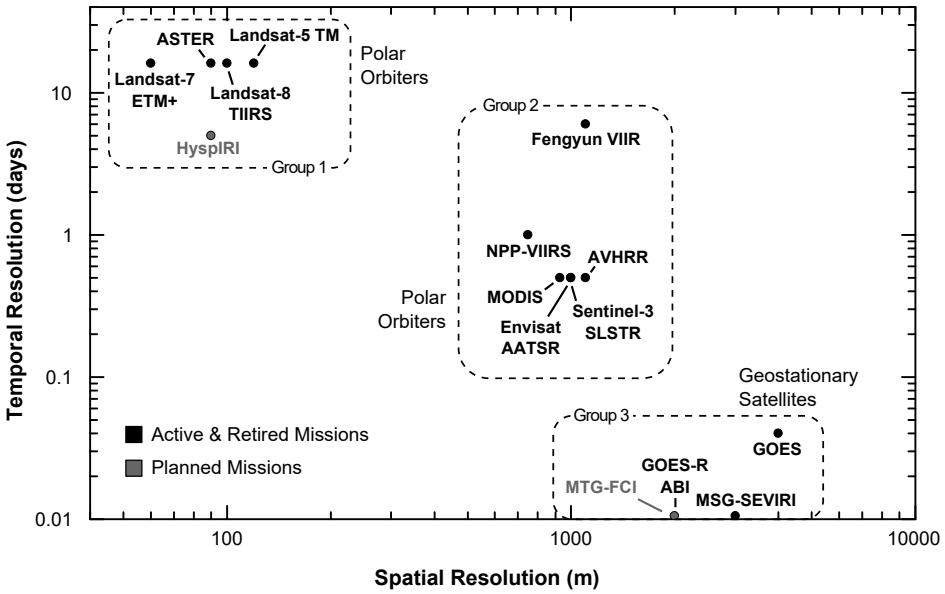

Figure 1.8: The anticorrelation between the spatial and temporal resolution of various satellite instruments. Source: the data are from the database of satellites and sensors of the Faculty of Geo-Information Science and Earth Observation (ITC) of the University of Twente.

surface evapotranspiration and the urban thermal environment [52]. However, as the review of Zhan et al. [53] highlights, the development of this research field was disordered and several issues are still unresolved or poorly understood. The most important of which is: what auxiliary data should be used as disaggregation kernels and how they should be configured into sets, considering that their performance varies with land cover, topography, biome, latitude, season, GSD and time of day [53]. Besides the identification of more robust disaggregation kernels, another issue that also requires attention is how downscaling, when applied to continuous temporally dense LST datasets, affects the spatiotemporal interrelationships of the data. Ideally downscaling schemes should be able to produce downscaled LST (DLST) accurately and consistently and DLST time series where the diurnal evolution of the data is artefact-free and synoptic weather effects and seasonal features are reproduced in greater spatial detail. However, this issue has been so far overlooked primarily due to the lack of appropriate validation data and evaluation methods. Nonetheless better understanding is required if LST downscaling methods are to be used operationally.

Last but not least, research should also focus on the development of methods for analysing and summarising such voluminous datasets. This is because, due to the high spatial and temporal resolution, the analysis and use of long DLST time

Table 1.3: The spatial and temporal resolution of various satellite instruments that acquire TIR data. Source: the data are from the database of satellites and sensors of the Faculty of Geo-Information Science and Earth Observation (ITC) of the University of Twente.

Satellite Sensor	Orbit Type	Spatial Resolution	Temporal Resolution
AATSR*	Sun-synchronous	1 km	4 times per day
ASTER	Sun-synchronous	90 m	irregular
AVHRR	Sun-synchronous	1 km	4 times per day
Fengyun-VIRR	Sun-synchronous	1.1 km	4 days
GOES-R ABI	Geostationary	2 km	15 min
GOES Imager	Geostationary	4 km	30 min
HyspIRI**	Sun-synchronous	60 m	5 days
Landsat-5 TM*	Sun-synchronous	120 m	16 days
Landsat-7 ETM+	Sun-synchronous	60 m	16 days
Landsat-8 TIRS	Sun-synchronous	120 m	16 days
MODIS	Sun-synchronous	1 km	4 times per day
MSG-SEVIRI	Geostationary	3 km	15 min
MTI-FCI**	Geostationary	2 km	15 min
NPP-VIIRS	Sun-synchronous	0.75 km	16 days
Sentinel-3 SLSTR	Sun-synchronous	1 km	4 times per day

* Retired Mission
** Future Mission

series is complex, time-consuming and expensive. To that end methods that are able to summarise the data into a set of spatially distributed parameters that are representative of the surface's thermal dynamics are highly desirable. A way to address this issue is by modelling the diurnal or annual LST cycle and then reducing the model to a set of key cycle parameters as done in [57, 58] and [59], respectively. So far only models for either the diurnal or the annual LST cycle have been proposed. Nevertheless, a method for simultaneously modelling the diurnal and annual cycle would provide a more complete picture of the Earth's surface thermal dynamics.

1.4 Thesis Scope and Research Objectives

The broad aim of this thesis is to improve and assess the downscaling of diurnal LST data from geostationary satellite instruments and also to facilitate the analysis of temporally dense LST or DLST datasets. In particular, given the research needs outlined in the previous section, the objectives of this thesis are:

1. to identify LST disaggregation kernels that perform consistently irrespectively of the time of day and thus are suitable for downscaling diurnal LST acquired by geostationary satellite instruments;

2. to investigate if and how well a DLST time series can reproduce the spatiotemporal features of the original coarse-scale temporally dense LST; and,

3. to develop a method for simultaneously modelling the diurnal and annual cycle of temporally dense LST or DLST and reducing the model to a set of key cycle parameters.

To attain these research objectives, LST data from Meteosat-10 *Spinning Enhanced Visible and Infrared Imager* (SEVIRI) [60, 61] are used. SEVIRI is the main instrument onboard the Meteosat Second Generation (MSG) geostationary satellites operated by the European Organisation for the Exploitation of Meteorological Satellites (EUMETSAT). It acquires image data of Europe, Africa and South America in eight TIR spectral bands (Figure 1.4b) every 15 min (the Earth imaging principle of SEVIRI is presented in Figure 1.9). At the sub-satellite nadir viewpoint (for Meteosat-10 it is located at $0°$E, $0°$N) the GSD is equal to $3\,\mathrm{km}$ and increases with VZA to $4\,\mathrm{km}$ over southern Europe and $6\,\mathrm{km}$ over northern Europe. SEVIRI has been designed to primarily serve the meteorological community, but LST downscaling can make SEVIRI a valuable data source for other disciplines as well.

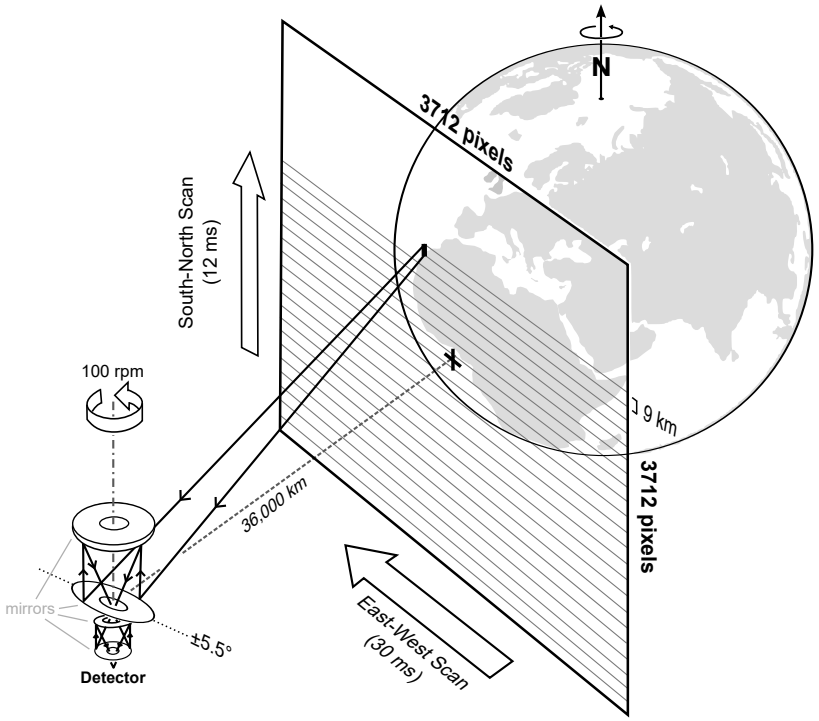

Figure 1.9: The Earth imaging principle of MSG-SEVIRI. Adapted from [61].

1.5 Thesis Outline

This introductory chapter provided the theoretical background for retrieving the LST from space observations and presented the objectives of this work and what research needs they address. The remainder of this thesis is organised into four chapters as follows.

Chapter 2 is concerned with the statistical downscaling of LST. It provides a detailed overview of the state-of-the-art along with a thorough discussion about LST disaggregation kernels and current limitations. Then the use of multi-temporal kernels derived from LST annual climatology data is proposed and tested on diurnal SEVIRI data. The evaluation is accomplished by assessing the DLST spatial patterns (both for daytime and nighttime) and the DLST diurnal temperature range. The work presented in this chapter has been published in the scientific journal *Remote Sensing* as an article titled *"Improving the Downscaling of Diurnal Land Surface Temperatures Using the Annual Cycle Parameters as Disaggregation Kernels"* [62].

Chapter 3 builds upon the findings of Chapter 2 and addresses the second research objective of this thesis. In particular, it describes the downscaling of a SEVIRI three-month long time series of quarter hourly LST from a GSD of $4\,\mathrm{km}$ to $1\,\mathrm{km}$ and assesses the accuracy and consistency of the downscaling method, the formed spatial patterns and the diurnal and seasonal characteristics of the DLST data. This assessment has been also published in *Remote Sensing* as an article under the title *"Assessing the Capability of a Downscaled Urban Land Surface Temperature Time Series to Reproduce the Spatiotemporal Features of the Original Data"* [63].

Chapter 4 addresses the third research objective of this work and proposes an approach for simultaneously modelling the LST diurnal and annual cycle. The proposed approach is based on [59] and is used for summarising Europe's surface thermal dynamics into a set of 48 LST cycle parameters. Part of the results presented in this chapter have been published in the scientific journal *IEEE Geoscience and Remote Sensing Letters* as an article titled *"Mapping the Spatiotemporal Dynamics of Europe's Land Surface Temperatures"* [64].

Finally *Chapter 5* recapitulates and discusses the main findings of this work in relation to the set research objectives and the identified research needs. To that end it also outlines the main contributions and suggests future research directions.

Chapter 2

Statistical Downscaling of Coarse-Resolution Diurnal LST

2.1 State-of-the-Art and Research Hypotheses

LST downscaling is a statistical method for disaggregating coarse-resolution LST[1] to finer GSD, using auxiliary datasets available at the desired fine resolution [53, 65]. These datasets are referred to as *predictors*, *disaggregation kernels*, or *scaling factors* and have to be statistically correlated to the LST in order to be effective. A very promising application field for LST downscaling is the spatial enhancement of geostationary temporally-dense LST images, so as to produce DLST datasets with high spatial and temporal resolution.

Fundamentally the downscaling of LST is related to three principal laws, namely the Bayesian theorem, Tobler's first law[2] of geography, and the surface energy balance (SEB) equation [67]. The Bayesian theorem provides a general framework for assimilating data of multiple sources, while Tobler's first law of geography and the SEB provide the background for understanding the LST spatial dependencies and how LST responds to the surface energy cycle. LST downscaling is also based on four interrelated assumptions. These assumptions are: the assumption of *additivity*, the assumption of *separability*, the assumption of *connectivity* and the assumption of *convertibility* [53, 65]. The first one indicates that the energy flux interactions among pixel components or pixels can be neglected and the second one that the LST component values are statistically separable. The third assumption,

[1] Statistical downscaling algorithms can also be used with TIR digital numbers (DN) and radiances.

[2] Tobler's first law of geography [66] states that *everything is related to everything else, but near things are more related than distant things*. This law provides the foundation for the fundamental concepts of spatial dependence and spatial autocorrelation.

i.e. connectivity, indicates that the LST can be predicted from the employed disaggregation kernels, while the fourth assumption, i.e. convertibility, that the spatial/spectral/temporal/angular information of the employed LST predictors can be combined and used for downscaling LST data.

In general, the workflow of a LST statistical downscaling method consists of three major operations. The first operation is the upscaling and co-registration of the fine resolution LST predictors to the coarse resolution LST data. The second operation is the generation of a *statistical model* on the basis of the coarse resolution LST data and predictors; and finally, the last operation is the application of this model to the fine resolution LST predictors so as to generate the DLST data. The employed empirical model can be linear or nonlinear [65, 67] depending[3] mostly on the type and number of LST predictors used. Zhan et al. [53] discuss that simple regression tools such as linear and quadratic tools are effective when the predictors' number is low, while complex tools such as support vector regression machines (SVM) are better suited when multiple LST predictors are employed. In principle, the LST is driven by numerous factors, including the thermal characteristics of the surface (e.g. heat capacity, thermal inertia), topography, vegetation abundance and vigour, soil moisture, sky-view factor[4], land cover and meteorological conditions [3, 8, 68]; and usually the relationship between the LST data and the LST predictors is *nonlinear* [67]. However, this nonlinearity is so complex [53, 68] that the derivation of explicit global models is not an easy task[5] and hence, even to this date, no strong evidence that support whether the linearity or nonlinearity performs better, exist [65].

Even more than the applied model, the set of LST predictors are the crucial element of every LST downscaling method and the key for meeting the connectivity assumption. This is because the LST predictors indicate the LST distribution in the fine spatial resolution and drive the empirical model [65]. In general the composition and selection of appropriate LST predictors should refer to the understood relations of LST with other biophysical variables and should also consider: the spatial scale; the landscape heterogeneity and morphology; and the temporal cycle (diurnal or

[3]For downscaling DN or TIR radiances the nonlinear factors of the atmospheric and emissivity effects should also be taken into consideration during the selection of a linear or nonlinear statistical model [65].

[4]The sky-view factor is the share of the visible sky above a certain observation point. It ranges from 0 to 1, where 1 means that the sky is completely visible.

[5]Several studies (e.g. [55] and [69]) have used a localisation strategy as a workaround to this issue, where they divided the image data into several groups of adjacent pixels and using a moving window they generated a linear statistical model for each one of them.

annual). The spatial scale is important because the application of a statistical downscaling method presupposes that the relationship between the LST data and the predictors is *scale invariant*, i.e. it is the same in the fine and coarse spatial resolution [70]. The landscape heterogeneity and morphology refer mainly to the particularities of a given geographical location that can distort the relationship between the LST and the biophysical variables used as LST predictors [53], while the temporal cycle is important because it might render some LST predictors less effective or even ineffective. For instance the correlation between LST and the Normalised Difference Vegetation Index (NDVI)—which is a widely-used LST predictor—is stronger during daytime than nighttime and during summertime than wintertime (it also drops as the moisture content of bare soils increases) [71, 72].

In recent literature several LST downscaling methods have been proposed that utilise various LST predictors, either individually or by combining them into large sets. Such LST predictors are: vegetation indices (VIs), topography data, impervious maps and VNIR, SWIR or TIR images. In particular, Kustas et al. [73] utilized the NDVI with a quadratic regression tool (this method is referred in literature as *disTrad*: disaggregation procedure for radiometric surface temperature), whereas Agam et al. [74] used the fractional vegetation cover with a linear tool and also other variants of disTrad. Inamdar et al. [68] employed the emissivity for downscaling LST from the Geostationary Environmental Satellite (GOES), while Essa et al. [75] expanded the disTrad methodology and tested 15 remote sensing based indices (individually) as LST predictors (including soil, vegetation and built-up indices). Stathopoulou and Cartalis [54] enhanced the spatial resolution of Advanced Very High Resolution Radiometer (AVHRR) LST data using as LST predictors the effective emissivity and a LST map retrieved from Landsat 5 data, while Dominguez et al. [76] sharpened simulated ASTER data using the NDVI and the albedo retrieved from airborne high resolution VNIR data.

Downscaling methods that utilize large sets of LST predictors became available after 2009 as the review of Zhan et al. [53] reveals. To that end, Zakšek and Oštir [55] used a LST predictor set comprising VIs, albedo, emissivity, land cover, slope, aspect, and sky-view factor data to downscale LST images retrieved from SEVIRI, while Keramitsoglou et al. [56] employed a set of 17 LST predictors that included topography data, land cover data, VIs and emissivity data in conjunction with a

SVM tool. Merlin et al. [77] used the fractional photosynthetically active and non-photosynthetically active vegetation cover for downscaling MODIS thermal data, while Weng et al. [78] utilised VIs, albedo, emissivity and elevation data to downscale GOES LST data. Lastly, Hutengs and Vohland [79] used as LST predictors VNIR and SWIR surface reflectance data, elevation data and derivatives (i.e. the solar incidence angle and the sky-view factor), and a land cover map with a random forest regression tool. Even though several LST predictors have been proposed and tested, there is still no consensus about which LST predictors perform the best and how they should be configured into sets. This is mainly because none of the above can perform well over various spatial scales, land covers, landscapes, seasons and times-of-day [53]. Hence it is highly desirable to identify LST predictors that perform robustly irrespectively of spatial scale, surface heterogeneity, surface morphology and the temporal cycle. The latter is particularly important when downscaling diurnal LST, where a robust performance is expected irrespectively of time.

To that end, this thesis hypothesises that LST predictors that provide information about the LST spatial distribution at different times-of-day can prove especially useful for downscaling diurnal LST. In addition, it also hypothesises that TIR-based LST predictors can prove quite robust for downscaling LST data. This is because, being derived from satellite thermal data, they incorporate the location-specific seasonal thermal response and thus can perform more consistently over various land cover types and landscapes. To investigate these hypotheses, multi-temporal TIR-based LST predictors are used in a *controlled experiment* for downscaling diurnal (daytime and nighttime) LST. The employed LST predictors are the MODIS LST *Annual Cycle Parameters* (ACP) [59], which are a globally available dataset that presents a continuous time-dependent description of the thermal surface behaviour and the thermal surface characteristics (i.e. the *thermal landscape*).

2.2 The LST Annual Cycle Parameters

The LST ACP [59, 80] consist of three key parameters that provide a simplified, cloud-free, time-dependent climatology of the Earth's annual LST cycle. These parameters are: the *Mean Annual Surface temperature* (MAST); the *Yearly Amplitude of Surface Temperature* (YAST; set by definition to be ≥ 0 K); and the *phase shift* of the peak LST relative to the spring equinox (Theta; is set by definition to range between

-182.5 and +182.5 days [59]). The physical meaning of MAST, YAST and Theta is shown in Figure 2.1, which also describes how the ACP are derived from *multi-year* LST observations. In particular, the derivation of the ACP is performed on a

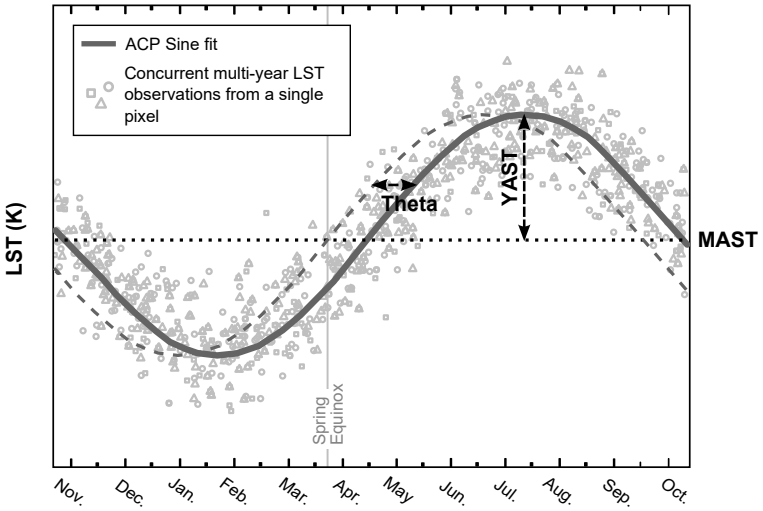

Figure 2.1: The physical meaning of the LST MAST, YAST and Theta Annual Cycle Parameters.

pixel-by-pixel basis by stacking the corresponding multi-year LST observations according to their acquisition day and then fitting[6] a *sine model*. The MAST, YAST and Theta are then derived from the sine model as shown in Figure 2.1. In addition to MAST, YAST and Theta, two more parameters are calculated, namely the root-mean-square-error (RMSE) of the fit and the number of clear-sky observations (NCSA) used for the fit. The former can be seen as an integrated measure of the LST inter-diurnal and inter-annual variability, while the latter as an indicator about the cloud occurrence frequency [80]. As discussed in [81], the sine model performs very well over mid-latitude regions where seasons are pronounced. The derivation of the ACP corresponds to the acquisition time of the satellite data and thus, for multiple acquisitions within a day, multiple sets of ACP can be generated, i.e. ACP that refer to morning, noon, afternoon or night hours. The MODIS ACP dataset employed in this work is available for four times within a day, namely at 01:30, 10:30, 13:30 and 22:30 UTC, which correspond to the overpass times of Terra and Aqua MODIS.

MAST and YAST have already been used as LST predictors in another downscaling study, where it was demonstrated that they can be used to bridge large scale

[6]The interested readers is referred to [59] where more details about the ACP sine fitting process are provided.

differences, i.e. in [82] a LST image from SEVIRI with a GSD of $5\,\mathrm{km}$ was downscaled to $0.1\,\mathrm{km}$. However, the use of the ACP for downscaling diurnal LST data and its ability to provide information about the LST diurnal fluctuations has not been assessed, which is the gap that this work addresses.

2.3 Using the ACP as LST Disaggregation Kernels

2.3.1 Research Objective and Experimental Setup

To answer the research hypotheses put forward in §2.1, this work investigates if the use of multi-temporal MAST, YAST and Theta as LST predictors can increase the performance of downscaling diurnal LST data and in particular if these LST predictors can improve the estimation of the DLST *diurnal range*, which is defined here as the difference between daytime and nighttime DLST data. The study of the DLST diurnal range is a strong indicator of how well the downscaling process can reproduce the diurnal LST cycle and preserve the spatiotemporal interrelationships of temporally dense LST data. This is a critical issue in the downscaling of geostationary LST data because it determines the exploitability of the generated DLST data (this issue is further discussed in Chapter 3). Hence to investigate this issue the controlled experiment of Figure 2.2 is used.

The basic concept of this experiment is to estimate two $1\,\mathrm{km}$ DLST diurnal range maps using two different sets of LST predictors, the first comprising only static LST predictors (scheme 1; *control*) and the second static and multi-temporal (scheme 2), and then to compare them with a reference $1\,\mathrm{km}$ LST diurnal range map retrieved from independent satellite data (the static predictors are kept the same in both schemes). The overall goal is to assess the changes induced by the TIR multi-temporal LST predictors (i.e. the MAST, YAST and Theta) on the DLST data.

The experimental setup presented in Figure 2.2 consists of four major stages. The first stage is the selection of the cloud-free scenes that will be used for the estimation of the diurnal range maps. The second stage is the downscaling of the previously selected coarse-resolution LST images. The third stage is the estimation of the $1\,\mathrm{km}$ daily DLST and reference LST diurnal range maps (daytime minus nighttime), while the last stage is the comparison and evaluation of the results obtained. Specifically, the DLST diurnal range maps employed in the evaluation are estimated using Eq. 2.1 and are the average of the daily DLST diurnal range maps estimated in stage

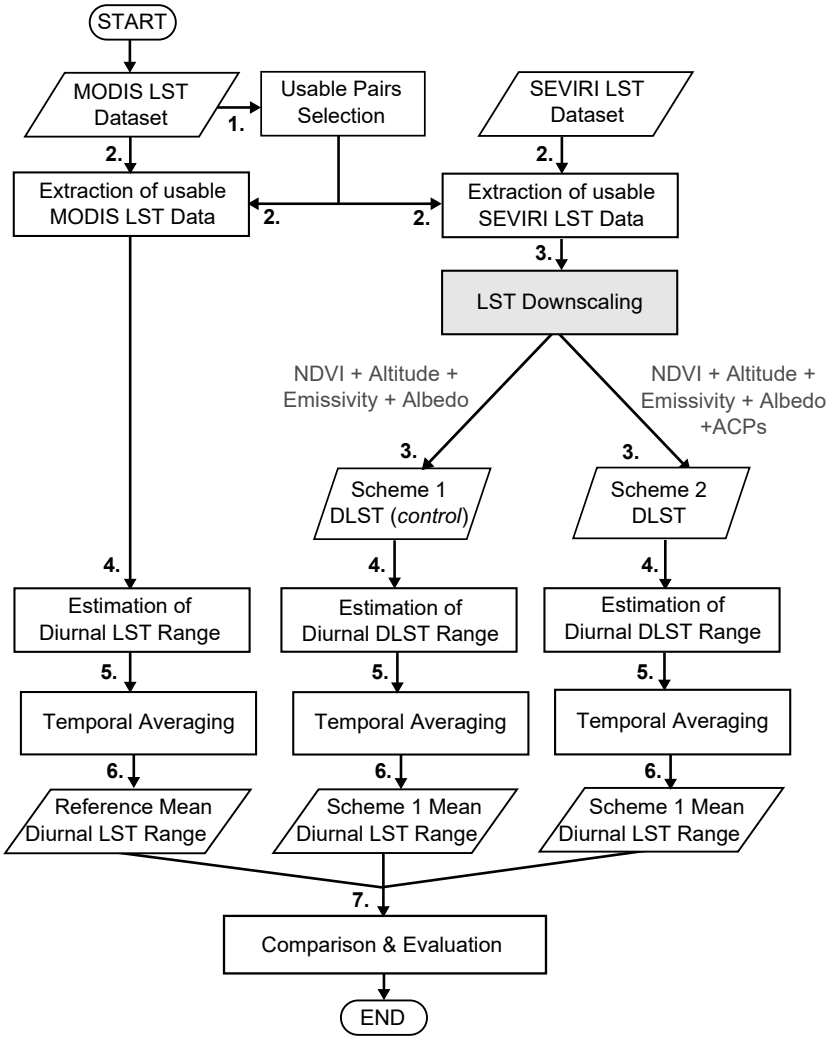

Figure 2.2: The controlled experiment performed so as to assess the use of MAST, YAST and Theta for downscaling diurnal LST data.

three. In this equation, n is the number of days used and d the day-of-year (DOY).

$$\text{mean diurnal DLST range} = \frac{1}{n}\sum_{d=1}^{n}(\text{DLST}_d^{\text{daytime}} - \text{DLST}_d^{\text{nighttime}}) \tag{2.1}$$

Eq. 2.1 is also used for the estimation of the reference LST diurnal range maps using as input the corresponding daytime and nighttime reference data.

2.3.2 Study area

The study area for this experiment is presented in Figure 2.3. It extends $60\,\text{km}$ around the city of Rome in Italy and covers an area of $10\,350\,\text{km}^2$. This region is deemed suitable for assessing the performance of the ACP as LST predictors because: it includes both flat and rugged areas; it has a simple coastline; and it includes rural, urban and

vegetated areas that are relatively homogeneous and confined to certain locations with easily-identifiable boundaries (approx. land cover percentages: 50%, 40% and 10%, respectively). The elevation of the study area varies from $0\,\mathrm{km}$ at the coast to $1.5\,\mathrm{km}$ over the Apennine Mountains (over Rome is about $30\,\mathrm{m}$ to $120\,\mathrm{m}$).

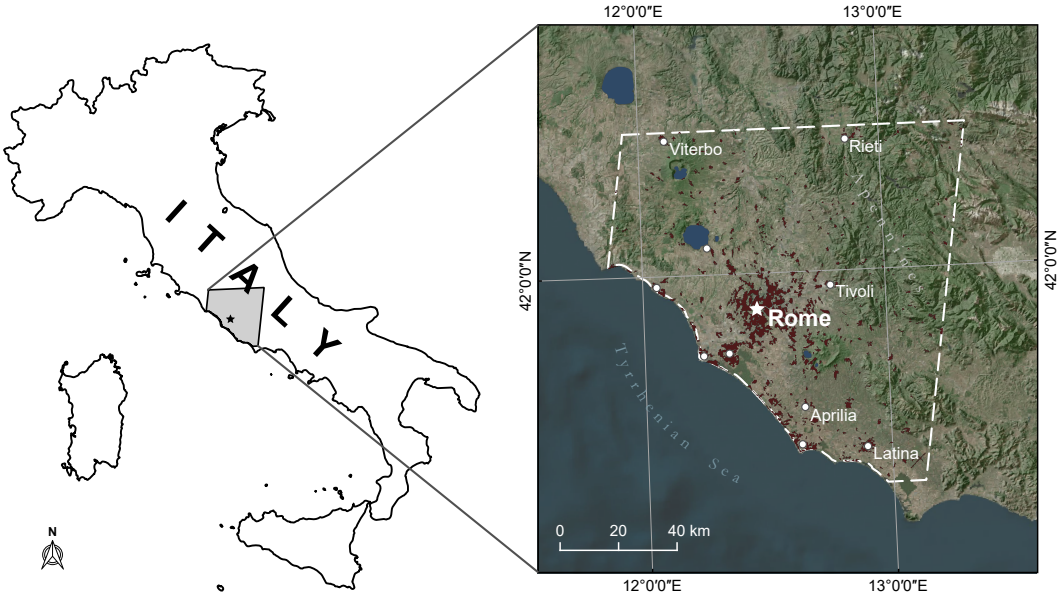

Figure 2.3: Rome greater region (Italy) is the study area for downscaling coarse-resolution SEVIRI LST using the ACP.

2.3.3 LST Data

The primary data (Table 2.1) employed in this study are LST images of Rome Greater Region acquired during summer 2014 (DOYs: 152 - 243) by Terra and Aqua MODIS and Meteosat-10 SEVIRI instruments. In particular, the employed MODIS LST data are the daily $1\,\mathrm{km}$ version 5 MOD11A1 and MYD11A1 data products [83], which are derived from the TIR radiances of MODIS band 31 ($10.78\,\mu\mathrm{m}$ to $11.28\,\mu\mathrm{m}$) and 32 ($11.77\,\mu\mathrm{m}$ to $12.27\,\mu\mathrm{m}$) using a generalized SW algorithm (see §1.2.4 for more details) [84]. The nominal accuracy of the MODIS LST is $1\,\mathrm{K}$ to $2\,\mathrm{K}$ and each MOD11A1 / MYD11A1 data file includes[7] two LST images, one corresponding to the daytime acquisition (for Terra at 10:30 UTC and for Aqua at 13:30 UTC) and one to the night-time (for Terra at 22:30 UTC and for Aqua at 01:30 UTC).

[7]Further, information about the viewing time, the VZA and the band-effective emissivity are also delivered.

Table 2.1: The employed LST data and LST predictors.

Data	Accuracy	GSD	Map Projection	Source
MOD/MYD11A1 v.5 LST	1 K to 2 K	1 km × 1 km	Sphere Sinusoidal	NASA EOSDIS[a]
SEVIRI LST	1 K to 2 K	4 km × 5 km	GEO	IAASARS/NOA
SRTM DEM	±6.2 m	1 km × 1 km	Sphere Sinusoidal	USGS[b]
MOD13A2 v.5 (NDVI)	±0.025	1 km × 1 km	Sphere Sinusoidal	NASA EOSDIS[a]
MOD11A2 v.5 (ε_{32})	1.9% [88]	1 km × 1 km	Sphere Sinusoidal	NASA EOSDIS[a]
MCD43B3 v.5 (WSA)	<5%	1 km × 1 km	Sphere Sinusoidal	NASA EOSDIS[a]
ACP	-	1 km × 1 km	Sphere Sinusoidal	UHH CliSAP[c]

[a] NASA's Earth Observing System Data and Information System (EOSDIS).
[b] United States Geological Survey (USGS).
[c] University of Hamburg Integrated Climate Data Center.

In addition to the above, SEVIRI LST data concurrent to the acquisition times of the MOD11A1 and MYD11A1 data products, are also employed (the time deviation between the corresponding MODIS and SEVIRI data is less than 7.5 min which is not considered a problem). These data have a coarser spatial resolution of approximately $4\,\mathrm{km}$ and were retrieved from the EUMETcast data acquisition station that the *Institute for Astronomy, Astrophysics, Space Applications and Remote Sensing* of the *National Observatory of Athens* (IAASARS/NOA) operates. The IAASARS/NOA system uses an in-house SVM-based LST retrieval algorithm [85, 86] that utilises as input the cloud-free TIR radiances from the $10.8\,\mu\mathrm{m}$ and $12\,\mu\mathrm{m}$ SEVIRI spectral bands and emissivity information from the MOD11A2 data product [83]. The evaluation of the employed SEVIRI LST data is discussed in [85] and has been performed using concurrent and collocated, high quality (accuracy of $1\,\mathrm{K}$ to $2\,\mathrm{K}$) independent Meteosat-10 SEVIRI data from LSA-SAF (Land Surface Analysis Satellite Application Facility [87]). The comparison with the LSA-SAF data revealed a mean difference of $-0.19\,\mathrm{K}$, a RMSE of $0.5\,\mathrm{K}$ and a Pearson's correlation coefficient of 99.8%.

2.3.4 LST Predictors

The LST predictors (Table 2.1) used for downscaling the SEVIRI image data are: altitude data from the Shuttle Radar Topography Mission digital elevation model (SRTM DEM) [89]; NDVI data from the MOD13A2 data product [90]; emissivity data from the MOD11A2 data product [83]; $0.3\,\mu\mathrm{m}$ to $0.7\,\mu\mathrm{m}$ white-sky albedo (WSA) data from the MCD43B3 data product [91]; and the ACP MAST, YAST and Theta discussed in §2.2 [59]. The SRTM DEM is a near-global, high quality DEM available free-of-charge at a spatial resolution of $30\,\mathrm{m}$ and $90\,\mathrm{m}$ (for this work it was upscaled

to $1\,\mathrm{km}$ using a bilinear convolution and then reprojected to the MODIS sinusoidal map projection). The MOD13A2 is a global $1\,\mathrm{km}$ vegetation index product that is generated every 16 days from MODIS VNIR data. The MOD11A2 and MCD43B3 are also $1\,\mathrm{km}$ globally available 16-day data products from MODIS. In particular the $11.77\,\mu\mathrm{m}$ to $12.27\,\mu\mathrm{m}$ band-effective emissivity data (ε_{32}) of the MOD11A2 are estimated using the land cover-based classification method of [40], while the WSA data of the MCD43B3, by integrating each pixel's BRDF (Bidirectional Reflection Distribution Function) over all viewing and irradiance directions. Lastly, the LST annual climatology data employed in this work are the 01:30, 10:30, 13:30 and 22:30 UTC $1\,\mathrm{km}$ MAST, YAST and Theta ACP (Figure 2.4) retrieved from a five-year (2009-2013) time series of MODIS LST data. The selection of the aforementioned LST predictors is based on the findings of [55], [56], [79], [82], [92] and [93].

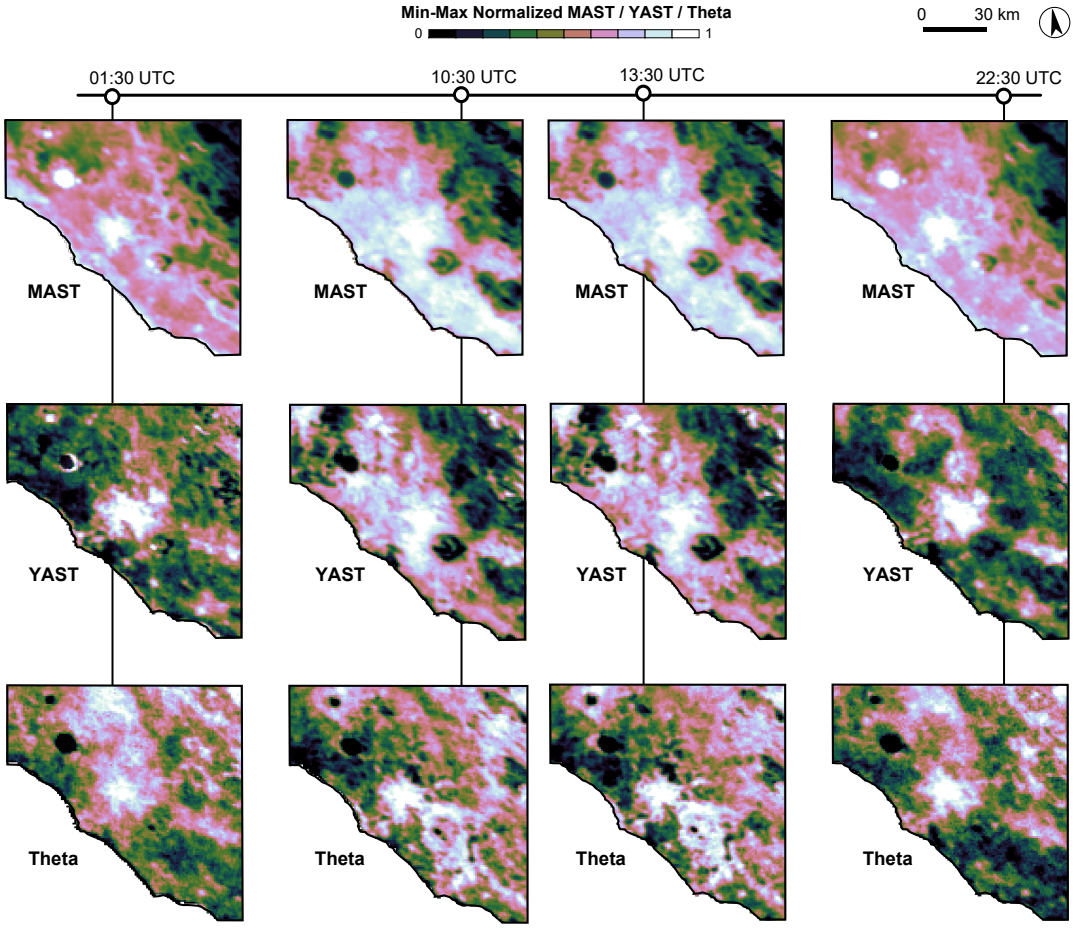

Figure 2.4: The 01:30, 10:30, 13:30 and 22:30 UTC MAST (first row), YAST (second row) and Theta (third row) ACP for Rome greater region in Italy.

2.3.5 Implementation Details

The experiment discussed in §2.3.1 and presented in Figure 2.2 is performed twice. The first time studying the mean diurnal range maps between 10:30 and 22:30 UTC (i.e. the Terra MODIS daytime and nighttime acquisition times) and the second time between 13:30 and 01:30 UTC (i.e. the Aqua MODIS daytime and nighttime acquisition times). For the first experiment, which is referred in the text as *10:30 vs. 22:30 UTC analysis*, the reference data are retrieved from the employed MOD11A1 data and for the second (referred in the text as *13:30 vs. 01:30 UTC analysis*) from the MYD11A1 data. The LST predictors of scheme 1 are the NDVI, the SRTM altitude (H), the ε_{32}, and the WSA, while the TIR multi-temporal of scheme 2 are the MAST, YAST and Theta.

As with most TIR remote sensing studies an important issue that can influence the analysis of the LST data is the impact of short-term weather effect [94]. Short-term weather effects influence the LST and especially the LST spatial patterns, e.g. a rainfall event can significantly change the emissivity of a region. For this reason it is advisable to use time series of LST data instead of individual scenes [94]. This way the results will be more representative for the study area. Hence, to make this study insusceptible to short-term weather effects, summer 2014 (DOYs: 152-243) was selected as the study period. The selection of this study period is based on the following four reasons: (i) it can provide a representative dataset for the purpose of this study; (ii) using LST data from the same year will ensure that the impact of phenological changes on the LST patterns will be reduced; (iii) the negative correlation of LST and NDVI, which is vital for the successful downscaling of LST data, is stronger during summer months [71]; and (iv) using summer data will ensure the availability of the most cloud-free daytime and nighttime LST data. This is especially important since for the estimation of the diurnal range maps cloud-free conditions during daytime and nighttime are required. In this work only LST and DLST diurnal range maps with low cloud cover (CC) are employed. In particular 33 scenes are employed for the 10:30 vs. 22:30 UTC analysis (median CC $= 12\%$) and 28 for the 13:30 vs. 01:30 UTC analysis (median CC $= 19\%$). The DOYs of the selected scenes are presented in Table 2.2. For consistency reasons the same DOYs are used for the calculation of the SEVIRI DLST and MODIS LST (i.e. the reference data) diurnal range maps. The temporal averaging of the DLST diurnal range data using Eq. 2.1 is justified on the basis that the MODIS data acquisition time is not exactly the same for each satellite

Table 2.2: The selected DOYs.

Analysis	DOY (Year: 2014)
10:30 vs. 22:30 UTC	153, 159, 160, 161, 162, 173, 175, 182, 184, 185, 187, 189, 192, 196, 198, 199, 208, 212, 216, 217, 219, 221, 223, 225, 226, 230, 232, 233, 235, 237, 240, 241, 242
13:30 vs. 01:30 UTC	155, 160, 171, 180, 181, 183, 185, 186, 188, 192, 196, 197, 199, 201, 206, 208, 212, 213, 217, 218, 219, 220, 222, 226, 229, 231, 234, 242

overpass and that would complicate the explanation and the discussion of the results. Hence, following this approach—even though it adds an additional source of statistical noise—it makes the performed analysis more straightforward.

Another important issue that can influence the analysis of LST data is thermal anisotropy [95, 96]. Thermal anisotropy refers to the angular variation of TIR radiation. This effect is stronger during daytime, when shadows are pronounced, and can make the LST of the same target to vary more than $2\,\mathrm{K}$ to $4\,\mathrm{K}$ when viewed by different directions (for more details see §1.2.5) [95, 96]. Thermal anisotropy is known to influence the comparison of LST data [1, 95, 96] and for this reason it is important to adopt compensation strategies when comparing LST data from different sources, as is this case. To that end, thermal anisotropy effects are more difficult to handle for MODIS than SEVIRI. This is because the MODIS VZA can range from -55° to $+55^\circ$ (the plus sign means the sensor views the area from west, while the minus sign from the east [97]), while SEVIRI, being onboard a geostationary satellite, acquires data with a constant VZA and azimuth angle (equal to $+50^\circ$ and 18.4°, respectively, for Rome greater region). Even though, this issue has attracted considerable attention in recent years no mature compensation methods are available yet. Nevertheless, a good practice for controlling this problem is to utilize LST data acquired with a similar viewing geometry (ideally it should be the same) [1]. This study follows this approach. In particular the performed analysis is based on the assumption that it is possible to compare and average LST diurnal range maps from different dates, provided that they are estimated from daytime and nighttime LST data (of the same DOY) with highly similar VZAs. In particular, it is assumed that by subtracting the two LST images (i.e. the daytime minus nighttime) the primary signal remaining is of the actual LST diurnal change. Following this approach it is possible to exploit the fact that the VZAs of daytime and nighttime MODIS data from the same DOY are very similar, as presented in Figure 2.5. In this figure the VZAs of the MODIS

LST data employed in this work (Table 2.2) are presented. In particular, the daytime-nighttime MODIS VZA differences for the selected scenes range between $6.5°$ to $10°$ with a median of $8°$.

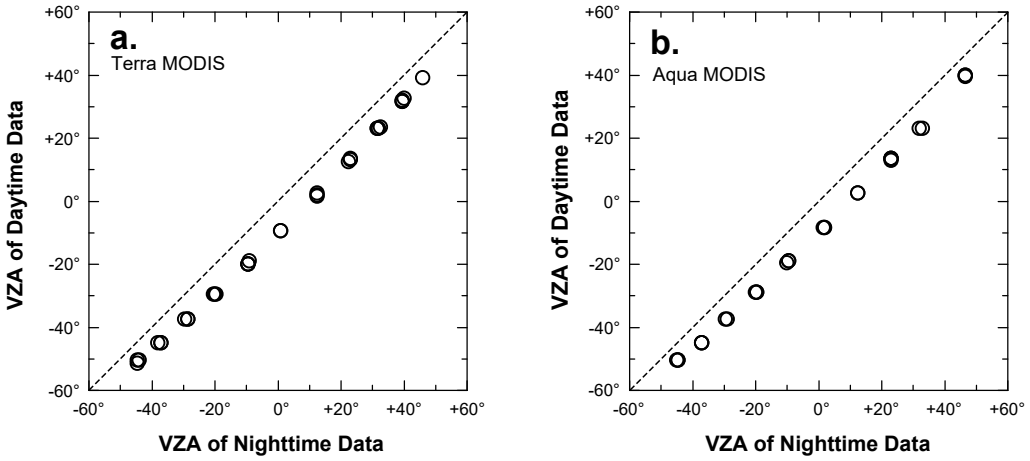

Figure 2.5: The VZA of the employed daytime and nighttime LST data retrieved from **(a)** Terra MODIS and **(b)** Aqua MODIS.

2.3.6 LST Downscaling Methodology

The downscaling of the SEVIRI data is based on a *multiple linear regression* due to its simplicity and efficiency [53] This type of regression attempts to model the relationship between the LST predictors (i.e. the explanatory variables) and the LST data (i.e. the response variable) by fitting a linear equation to the observations. The general form of a multiple linear regression is presented in Eq. 2.2. In this equation y is the response variable; k is the number of explanatory variables used; $A_0, \ldots, A_k$ are the regression coefficients; and $x_0, \ldots, x_k$ are the explanatory variables.

$$y = A_0 + A_1 x_1 + A_2 x_2 + \cdots + A_k x_k \tag{2.2}$$

The workflow of the LST downscaling method employed in this work is presented in Figure 2.6 and consists of three major operations. The first operation is the upscaling and co-registration of the fine-resolution LST predictors to the coarse-resolution LST data and the min-max normalization of the LST predictors between 0 and 1 so as to have comparable values (the normalization boundaries used are common between the $1\,\mathrm{km}$ and $4\,\mathrm{km}$ version of each LST predictor). The upscaling and co-registration process is performed using an intermediate $1\,\mathrm{km} \times 1\,\mathrm{km}$ grid that assigns which $1\,\mathrm{km}$ pixels belong to each coarse scale $4\,\mathrm{km} \times 5\,\mathrm{km}$ pixel on the basis

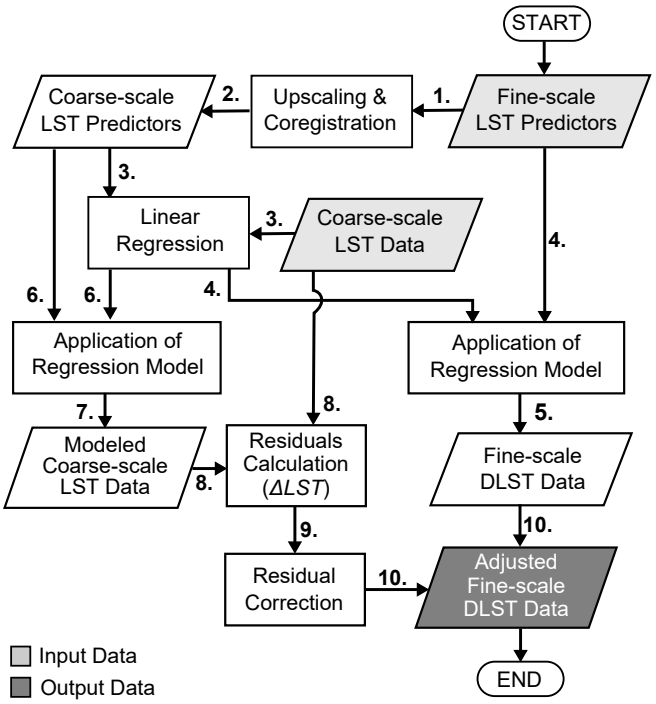

Figure 2.6: The workflow of the employed LST downscaling algorithm.

of their geographical coordinates similar to [55] and [56]. The coarse-resolution LST predictors are estimated eventually as the mean of all the fine-resolution pixels that belong to each coarse-resolution cell. The second operation is the development of the regression model (Eq. 2.2) that describes the relationship between the coarse-resolution LST data and LST predictors. The derived linear regression model is global and unique for each image employed. This selection is justified on the fact that the study area is of limited extent. The third operation of the employed method is the application of the retrieved regression model to the fine spatial resolution LST predictors so as to generate the DLST image data. The third operation is coupled with a DLST adjustment process (i.e. a residual correction) as done in [73, 74, 79, 93]. This process aims to compensate the loss of variability due to the inflexibility of the linear regression tool and it is based on the difference of the observed and modelled coarse-resolution LST data. In particular, the residuals (ΔT_s) between the modelled and the observed coarse-resolution LST are calculated using Eq. 2.3 and then incorporated to the spatially enhanced LST data using Eq. 2.4. Prior to the application of Eq. 2.4, the residuals ΔT_s are resampled to the $1\,\mathrm{km} \times 1\,\mathrm{km}$ DLST grid. A *smoothing filter* is also applied to the resampled $\Delta T_{\mathrm{s}}^{\mathrm{resampled}}$ so as to prevent the occurrence of boxy effects on the DLST data, as suggested in [93]. The $\mathrm{DLST}_{\mathrm{adj}}$ are the primary

output of the employed downscaling method and the main input to Eq. 2.1.

$$\Delta T_{\mathrm{s}} = T_{\mathrm{s}}^{\text{observed}} - T_{\mathrm{s}}^{\text{modelled}} \tag{2.3}$$

$$\mathrm{DLST}_{\mathrm{adj}} = \mathrm{DLST} + \Delta T_{\mathrm{s}}^{\text{resampled}} \tag{2.4}$$

As discussed in the begining of this section, the downscaling method presented above is employed twice. The first time utilizing as LST predictors the NDVI, the H, the ε_{32}, and the WSA (Scheme 1; Eq. 2.5a), and the second time all of the above, plus MAST, YAST and Theta (Scheme 2; Eq. 2.5b).

$$\mathrm{DLST}_{\mathrm{adj}} = f\left(H, \mathrm{NDVI}, \varepsilon_{32}, \mathrm{WSA}\right) \tag{2.5a}$$

$$\mathrm{DLST}_{\mathrm{adj}} = f\left(H, \mathrm{NDVI}, \varepsilon_{32}, \mathrm{WSA}, \mathrm{YAST}, \mathrm{MAST}, \mathrm{Theta}\right) \tag{2.5b}$$

The overall goal is to use the DLST diurnal range map of scheme 1 as control so as to assess the performance of MAST, YAST and Theta as LST predictors. The evaluation of the derived data is based on the RMSE (Eq. 2.6), the Mean-Absolute-Error (MAE, Eq. 2.7) and Pearson's Correlation Coefficient (Rho, Eq. 2.8). In these equations X corresponds to the SEVIRI DLST data and Y to the reference MODIS LST.

$$\mathrm{RMSE} = \sqrt{\frac{\sum_{\mathrm{pxl}=1}^{n}\left(X_{\mathrm{pxl}} - Y_{\mathrm{pxl}}\right)^2}{n}} \tag{2.6}$$

$$\mathrm{MAE} = \frac{\sum_{\mathrm{pxl}=1}^{n}\left|X_{\mathrm{pxl}} - Y_{\mathrm{pxl}}\right|}{n} \tag{2.7}$$

$$\mathrm{Rho} = \frac{n\sum_{\mathrm{pxl}=1}^{n}\left(X_{\mathrm{pxl}} - \overline{X}\right)\left(Y_{\mathrm{pxl}} - \overline{Y}\right)}{\sqrt{\sum_{\mathrm{pxl}=1}^{n}\left(X_{\mathrm{pxl}} - \overline{X}\right)^2}\sqrt{\sum_{\mathrm{pxl}=1}^{n}\left(Y_{\mathrm{pxl}} - \overline{Y}\right)^2}} \tag{2.8}$$

The validity of the scale invariance assumption for the employed LST predictors is evidenced in Figure 2.7 where the relationship between the employed $1\,\mathrm{km}$ MODIS and $4\,\mathrm{km}$ SEVIRI mean LST data and LST predictors is presented both for daytime (10:30 UTC) and nighttime (22:30 UTC). In detail, the corresponding $1\,\mathrm{km}$ and $4\,\mathrm{km}$ point clouds of Figure 2.7 coincide and have similar shapes and comparable Rho values. Hence, it is assumed that the LST data-predictor relation is consistent for the $1\,\mathrm{km}$ and $4\,\mathrm{km}$ spatial scales and thus the use of Eq. 2.5a and Eq. 2.5b for downscaling the SEVIRI data is possible. The moderate-to-high Rho values of Figure 2.7 (with the exception of Theta, the ε_{32}, and nighttime YAST) also suggest

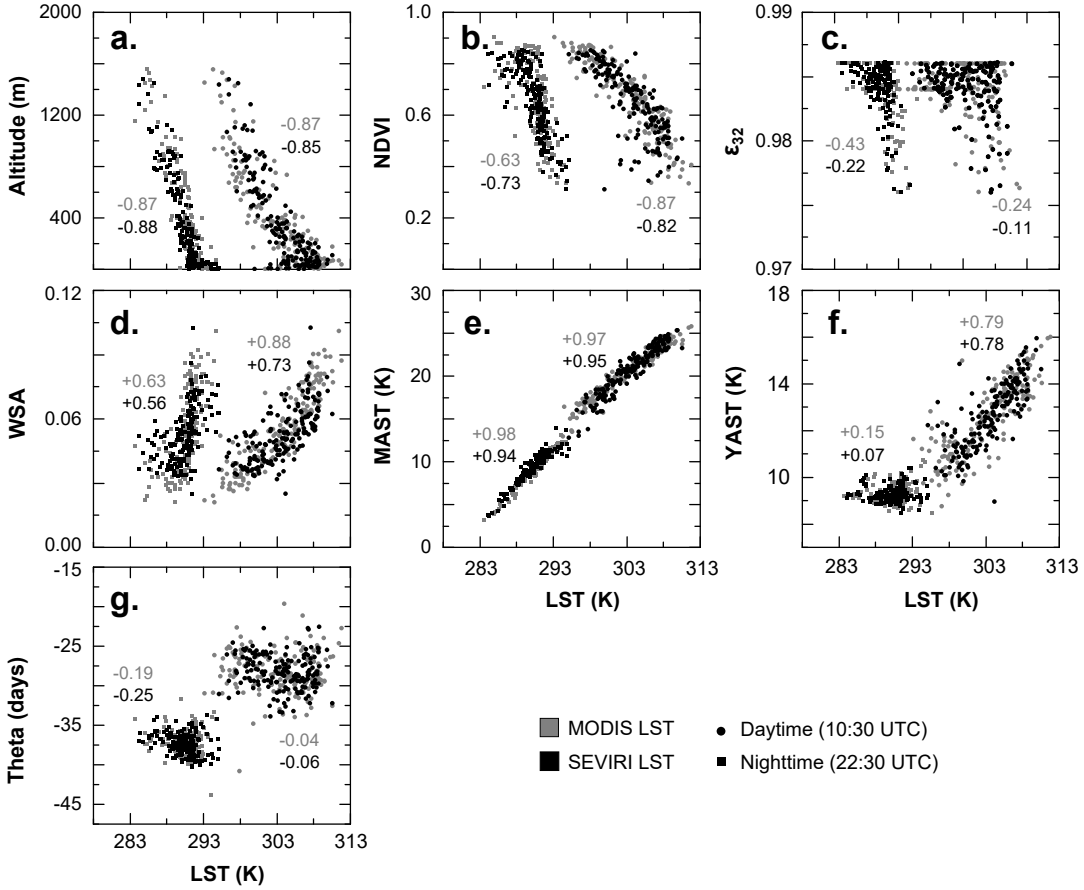

Figure 2.7: The relationship between the **(a)** Altitude; **(b)** NDVI; **(c)** ε_{32}; **(d)** WSA; **(e)** MAST; **(f)** YAST; and **(g)** Theta and the employed mean $1\,\mathrm{km}$ MODIS and $4\,\mathrm{km}$ SEVIRI daytime (10:30 UTC) and nighttime (22:30 UTC) LST data. For each point cloud the corresponding Pearson's correlation coefficient is also presented.

that the employed LST predictors provide relevant information to the downscaling process and thus meet the connectivity assumption [53]. Specifically, the highest Rho values correspond to MAST, altitude, WSA and NDVI LST predictors and the lowest to Theta. A change in Rho between daytime and nighttime is also observable, especially for YAST, WSA and NDVI. Finally, the dependency of the employed LST predictors is presented in the correlation matrix of Table 2.3. From this table it is evident that the dependency between the utilized LST predictors is in most cases low. Nonetheless, a moderate dependency between altitude and NDVI, and YAST (10:30 UTC) and NDVI and WSA is evident; as well as a high association between MAST (10:30 UTC and 22:30 UTC) and Altitude.

Table 2.3: The Rho^2 matrix of the employed fine-resolution LST predictors. The subscripts D and N correspond to 10:30 UTC and 22:30 UTC, respectively

	H	NDVI	ε_{32}	WSA	$YAST_D$	$MAST_D$	$Theta_D$	$YAST_N$	$MAST_N$	$Theta_N$
H	1.00	0.46	0.01	0.50	0.27	0.83	0.01	0.04	0.73	0.01
NDVI		1.00	0.01	0.78	0.57	0.65	0.01	0.18	0.33	0.00
ε_{32}			1.00	0.00	0.02	0.08	0.12	0.03	0.20	0.00
WSA				1.00	0.57	0.70	0.01	0.14	0.34	0.00
$YAST_D$					1.00	0.49	0.00	0.30	0.10	0.06
$MAST_D$						1.00	0.00	0.10	0.61	0.01
$Theta_D$							1.00	0.16	0.00	0.18
$YAST_N$								1.00	0.00	0.46
$MAST_N$									1.00	0.05
$Theta_N$										1.00

2.4 Results

2.4.1 Statistical Comparison with Reference Data

Overall the inclusion of MAST, YAST and Theta as LST predictors improved considerably the estimation of the diurnal range from the DLST data (Figure 2.8). In particular, for the 10:30 vs. 22:30 UTC analysis the RMSE is reduced from $1.4\,K$ for scheme 1 to $1.0\,K$ for scheme 2, while the MAE from $1.1\,K$ to $0.8\,K$ (Table 3.2). The corresponding values for the 13:30 vs. 01:30 UTC analysis are for RMSE $2.0\,K$ and $1.6\,K$, respectively, and for MAE $1.6\,K$ and $1.2\,K$. The mean difference (bias) with the reference MODIS data is close to $0\,K$ for all cases.

Table 2.4: Various statistical measures quantifying the difference of the DLST diurnal range data with the reference MODIS data.

Measures	10:30 vs. 22:30 UTC		13:30 vs. 01:30 UTC	
	Scheme 1	Scheme 2	Scheme 1	Scheme 2
Mean Difference (K)	-0.1	-0.1	0.2	0.1
MAE (K)	1.1	0.8	1.6	1.2
RMSE (K)	1.4	1.0	2.0	1.6
Rho	0.90	0.95	0.89	0.94
R^2	0.81	0.90	0.80	0.88

The similarity of the DLST diurnal range data with the reference data is also increased with the use of the ACP as LST predictors. Specifically, Rho increased from 0.90 to 0.95 for the 10:30 vs. 22:30 UTC analysis and from 0.89 to 0.94 for the 13:30 vs. 01:30 UTC analysis (Table 3.2). This is also evident in the scatterplots

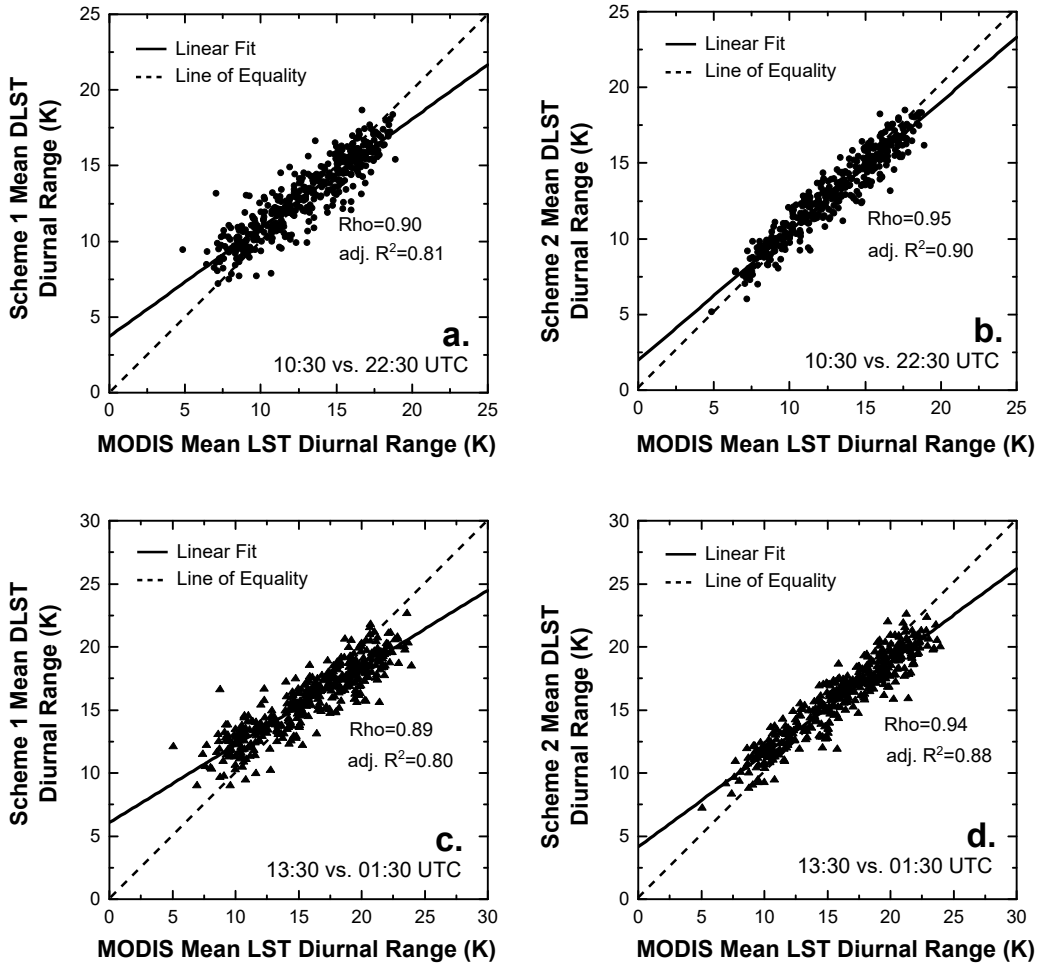

Figure 2.8: Scatterplots of the mean diurnal DLST range (daytime minus nighttime) versus the reference data for the 10:30 vs. 22:30 UTC analysis (**(a)** scheme 1 and **(b)** scheme 2 data) and the 13:30 vs. 01:30 UTC analysis (**(c)** scheme 1 and **(d)** scheme 2 data).

of Figure 2.8, where the point clouds of scheme 2 match better the line of equality ($y = x$) than those of scheme 1. Specifically for the 10:30 vs. 22:30 UTC analysis, the intercept of scheme 1's linear fit is 3.72 and the slope 0.72, while for scheme 2 the corresponding values are 1.97 and 0.85, respectively. For the 13:30 vs. 01:30 UTC analysis the intercept and slope are 6.07 and 0.61 for scheme 1, and 4.15 and 0.73 for scheme 2, respectively.

The use of MAST, YAST and Theta also improved the distribution of the DLST diurnal range values as Figure 2.9 and Table 2.5 reveal. In detail the distributions of scheme 2 data are more widespread and match better the reference data in contrast to scheme 1, which are more condensed over the middle-range values (i.e. the 25th-75th percentiles). Nevertheless the mean and median values of both scheme 1 and scheme 2 are almost the same and equal to the reference MODIS data (13 K for the

10:30 vs. 22:30 UTC analysis and 16 K for the 13:30 vs. 01:30 UTC analysis; Table 2.5).

Table 2.5: The mean, minimum, maximum and 1%, 5%, 25%, 50% (median), 75%, 95% and 99% values of the reference LST and scheme 1 and scheme 2 DLST diurnal range data. The term Terra refers to the 10:30 vs. 22:30 UTC analysis and the term Aqua to the 13:30 vs. 01:30 UTC analysis.

Analysis	Data	Mean (K)	Min (K)	Max (K)	Percentiles (K)						
					1%	5%	25%	50%	75%	95%	99%
Terra	Ref.	12.9	1.1	20.1	6.3	7.7	10.3	13.1	15.6	17.4	18.3
	Sch. 1	13.0	5.7	21.3	7.9	9.1	11.0	13.1	15.1	16.8	17.9
	Sch. 2	13.0	3.3	19.3	7.1	8.5	10.9	13.1	15.4	17.1	18.0
Aqua	Ref.	16.0	1.8	25.7	7.4	9.2	12.7	16.6	19.5	21.8	23.1
	Sch. 1	15.9	7.2	25.2	9.6	11.3	13.8	16.3	18.1	20.2	21.2
	Sch. 2	16.0	6.6	22.9	9.1	10.7	13.4	16.5	18.6	20.6	21.5

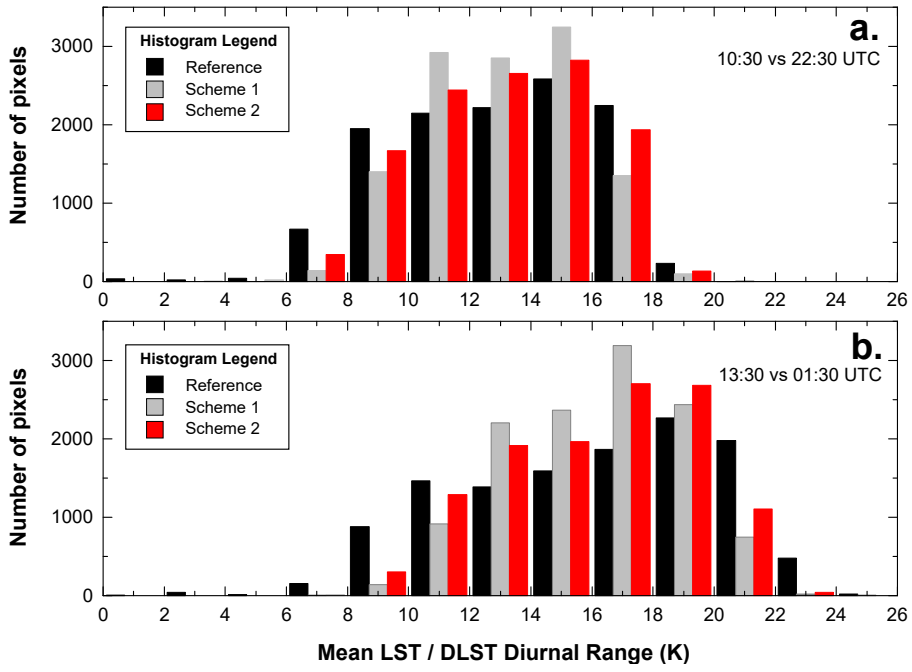

Figure 2.9: Histograms presenting the distribution of **(a)** the 10:30 vs. 22:30 UTC and **(b)** the 13:30 vs. 01:30 UTC diurnal DLST range in respect to the reference MODIS data.

The inclusion of the ACP also improved the estimation of the minimum DLST diurnal range and the 1% and 5% percentiles (Table 2.5). In particular, for the 10:30 vs. 22:30 UTC analysis the minimum dropped from 5.7 K for scheme 1 to 3.3 K for scheme 2 (the reference is 1.1 K). A similar but not so pronounced improvement is also observable for the 13:30 vs. 01:30 UTC analysis (from 7.2 K to 6.6 K; Ref.=1.8 K). However, the inclusion of the ACP as LST predictors did not improve the estimation

of the 95%, 99% and maximum DLST diurnal range, which deviates for about 1 K to 2 K from the reference data for both schemes.

2.4.2 Analysis of the Spatial Patterns and the Impact of Land Cover and Altitude

For Rome greater region the most pronounced diurnal DLST range corresponds to the rural area surrounding the city of Rome (Figures 2.10 and 2.11). Specifically, the mean rural 10:30 vs. 22:30 UTC DLST diurnal range is 15.9 K for scheme 1 and 16.3 K for scheme 2 (Ref.= 16.6 K); while the corresponding 13:00 vs. 01:30 UTC values are 18.6 K and 19.1 K, respectively (Ref.=20.5 K). In both cases scheme 2 is closer to the reference data than scheme 1 (Figure 2.10). The weakest DLST diurnal range corresponds to the Apennine Mountains. In particular, the reference mean diurnal range for the Apennines is 10.4 K for the 10:30 vs. 22:30 UTC analysis and 12.4 K for the 13:00 vs. 01:30 UTC analysis. Both scheme 1 and scheme 2 overestimate these values by approximately 1.0 K (Figure 2.10).

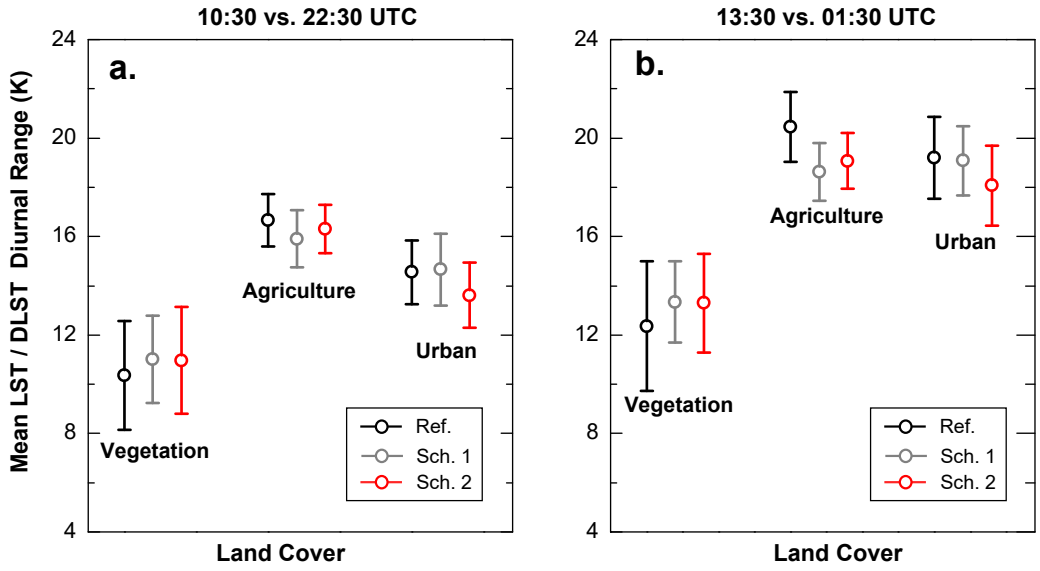

Figure 2.10: The mean DLST diurnal range (and standard deviation) for areas covered by vegetation (over the Apennines), agriculture and urban land cover classes.

For the city of Rome the 10:30 vs. 22:30 UTC DLST diurnal range is 14.7 K for scheme 1 and 13.6 K for scheme 2 (Ref.= 14.5 K). The corresponding values for the 13:30 vs. 01:30 UTC analysis are 19.1 K and 18.1 K, respectively (Ref.=19.2 K). In both cases scheme 1 performed slightly better than scheme 2, which underestimated the reference mean by 1.0 K. Nevertheless the shape of the spatial pattern of Rome's built-up is more similar to the reference data in scheme 2 than of scheme 1 (Figure

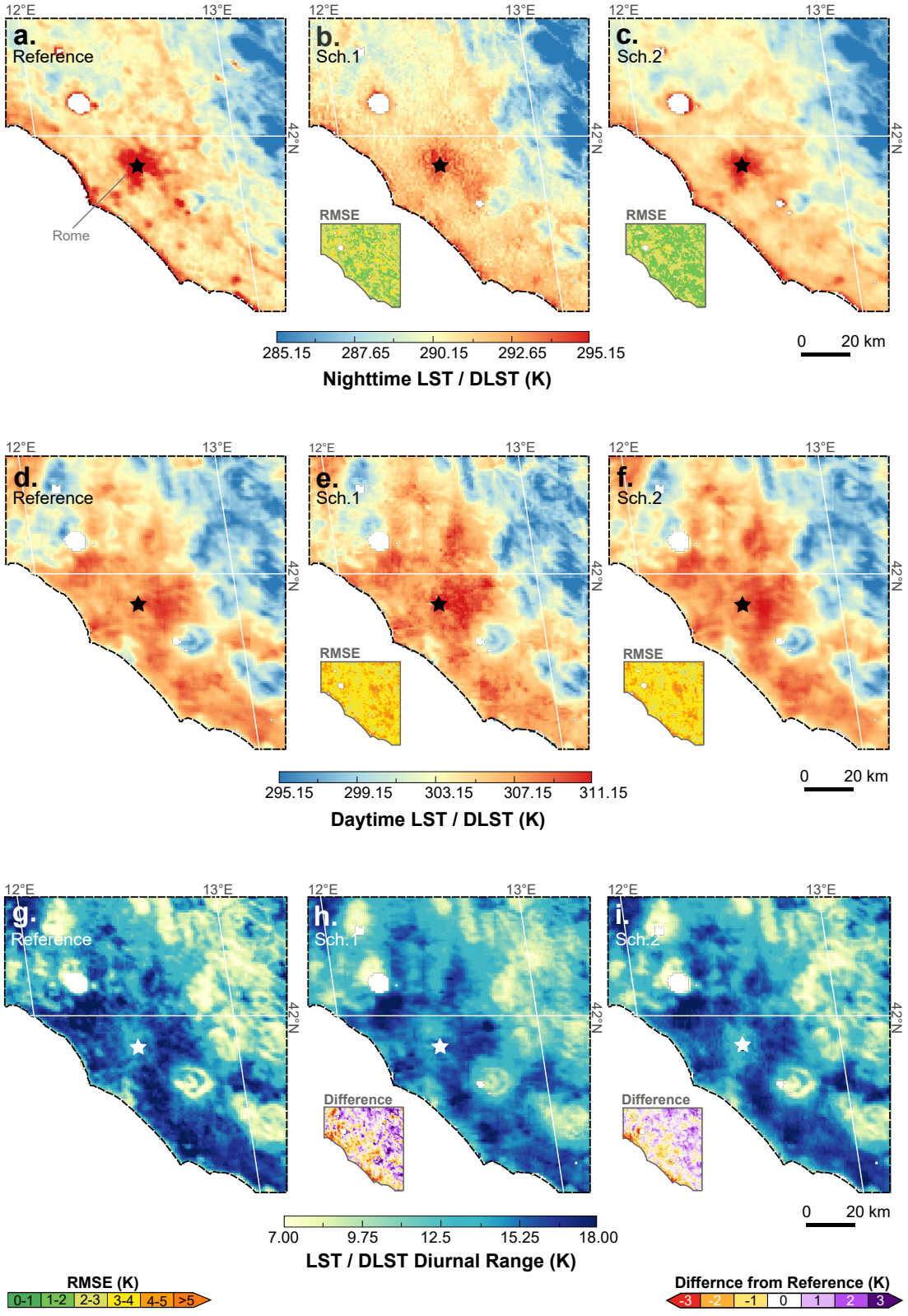

Figure 2.11: (a-c) The 22:30 UTC and **d-f)** 10:30 UTC mean LST and DLST maps and **(g-i)** the corresponding diurnal range maps for MODIS LST, SEVIRI DLST Scheme 1 and SEVIRI DLST Scheme 2.

2.11). In detail, the thermal spatial pattern of Rome's urban agglomeration exhibits a very distinct thermal behaviour due to the Surface Urban Heat Island (SUHI) effect. This effect is primarily caused by the higher thermal conductivity and heat storage capacity of impervious surfaces (e.g. concrete and asphalt) [13, 12] and results to increased urban nighttime temperatures. In this study this effect is evidenced as a weakening of the DLST diurnal range of Rome and the formation of a very distinct spatial feature that looks like a hole (Figure 2.11). In particular, Rome's 10:30 vs. 22:30 UTC diurnal range pattern is presented for schemes 1 and 2 in Figures 2.11h and 2.11i, respectively. The comparison with the reference data (Figure 2.11g) reveals that scheme 2 outperformed scheme 1, which underestimated the 10:30 vs. 22:30 UTC DLST change of the city's eastern part.

The better performance of scheme 2 in respect to scheme 1 in reproducing the reference LST diurnal range spatial patterns is also observable in the Difference-from-Reference maps of Figure 2.11. Overall, both scheme 1 and scheme 2 show the same spatial features: an overestimation (purple colours) over the Apennines and an underestimation (orange colours) over the rural area surrounding the city of Rome. However, the magnitude of the differences from the reference data is considerably greater for scheme 1 than for scheme 2 (the above also applies for the 13:30 vs. 01:30 UTC analysis). The exception is the coastline where both scheme 1 and scheme 2 underestimated its diurnal DLST range. This problem is mainly due to two reasons: (i) the LST retrieval of coastline pixels which is known to be more error prone due to emissivity uncertainties [1]; and (ii) the difference in pixel size between SEVIRI and MODIS, which can result to considerably different samplings over highly heterogeneous regions (e.g. coastlines) [39].

The assessment of the obtained DLST diurnal range data concludes with an analysis of how they change with altitude. In Figure 2.12, the relationship between the mean DLST diurnal range and altitude is presented. Overall, the curves of scheme 1 and scheme 2 match well with the curve of the reference MODIS data. As expected, a slight overestimation of the DLST diurnal range for the areas with an altitude greater than $500\,\mathrm{m}$ is evident for both schemes. For the $50\,\mathrm{m}$ to $500\,\mathrm{m}$ range the results are substantially better and the DLST data almost match the reference data.

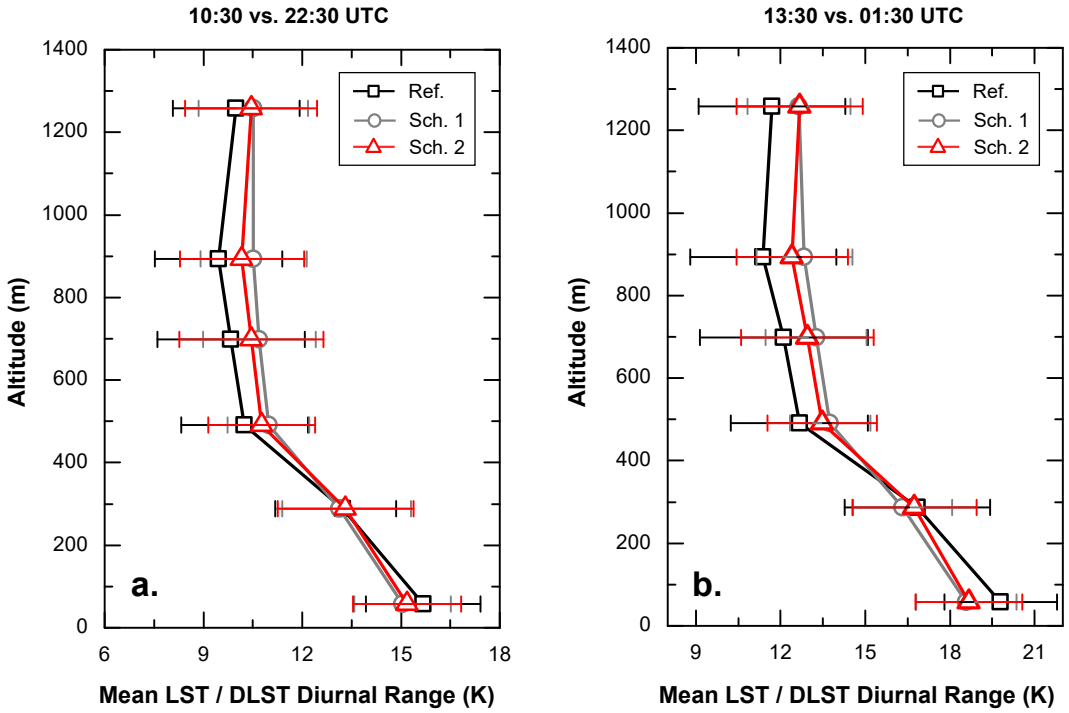

Figure 2.12: The mean DLST diurnal range in respect to altitude: **(a)** for the 10:30 vs. 22:30 UTC analysis and **(b)** for the 13:30 vs. 01:30 UTC analysis.

2.4.3 Similarity of the MODIS LST and SEVIRI DLST time series

Finally, a comparison between the daytime and nighttime MODIS LST (Table 2.2) and the corresponding SEVIRI DLST datasets is given. Overall the employed data exhibit a high degree of similarity, with scheme 2 data to perform slightly better than scheme 1 (Table 3.2). The mean difference (bias) between the $1\,\mathrm{km}$ SEVIRI DLST and MODIS LST data ranges from $0\,\mathrm{K}$ to $-0.5\,\mathrm{K}$ while the RMSE is close to $1.3\,\mathrm{K}$ for the nighttime data and $2.5\,\mathrm{K}$ for the daytime data. The standard deviation (σ) of the MODIS LST and SEVIRI DLST differences is $2.5\,\mathrm{K}$ for the 10:30 UTC and 13:30 UTC data and $1.2\,\mathrm{K}$ for the 01:30 UTC and 22:30 UTC data. Rho is equal to approximately 0.9 for all cases. Scheme 2 outperforms scheme 1 at all acquisitions times but the added value is highest at 01:30 and 10:30 UTC while it is rather little at 13:30 UTC.

Table 2.6: Various statistical measures quantifying the difference of the DLST diurnal range data with the reference MODIS data.

Measures	01:30 UTC		10:30 UTC		13:30 UTC		22:30 UTC	
	Sch. 1	Sch. 2	Sch. 1	Sch. 2	Sch. 1	Sch. 2	Sch. 1	Sch. 2
Bias (K)	−0.41	−0.41	−0.46	−0.46	−0.19	−0.16	−0.48	−0.50
σ (K)	1.37	1.00	2.44	2.29	2.70	2.64	1.31	1.14
RMSE (K)	1.43	1.08	2.48	2.33	2.70	2.65	1.40	1.23
Rho	0.87	0.93	0.87	0.89	0.87	0.88	0.89	0.91

The high similarity of the mean SEVIRI DLST with the MODIS LST data is also evident in Figure 2.11a-f. Overall the same spatial features are presented in the corresponding maps. The most pronounced spatial pattern difference is the nighttime DLST pattern of Rome of scheme 1, which is due to the weakening of the relationship between the LST predictors and the nighttime LST data.

2.5 Discussion

The results of this study suggest that the use of MAST, YAST and Theta as LST predictors improve the downscaling of coarse-scale LST data and also the estimation of the diurnal range from the DLST data. MAST, YAST and Theta represent the thermal landscape of a region [59, 80] and can be estimated for various times within a day (e.g. morning, noon, afternoon and night) depending on the availability of satellite data. Hence, these LST predictors can be very useful for the downscaling of geostationary diurnal LST data, which is a more demanding process than the downscaling of single scenes. This is because the spatiotemporal interrelationships of the LST data, which are driven by the thermodynamic characteristics of the surface materials; the short-term meteorological conditions; and the diurnal and annual cycle of heating and cooling, have to be preserved.

In this work MAST, YAST and Theta improved the downscaling of both daytime and nighttime LST data and also their interrelationship. The former is evident through the comparison with the corresponding MODIS data and the latter with the estimation of the DLST diurnal range, which is the main focus of this paper. The estimation of diurnal thermal differences, (e.g. daytime minus nighttime), is particularly useful for numerous studies such as: the assessment of regional and global climate change [98, 99]; the estimation of evapotranspiration [100, 101]; the assessment and monitoring of the SUHI effect [55, 56, 102]; the estimation of crop yield [103]; and the assessment of excess heat effects to human health [104] (for most of these studies a LST accuracy of 1 K or better is required [1]). The use of the three ACP components as LST predictors improved considerably the thermal spatial patterns of the nighttime data, which were influenced by the weakening of the LST predictor's relationship with LST [71]. In addition, MAST, YAST and Theta improved the estimation of the very low DLST values and the overall distribution of the DLST diurnal range. Usually downscaling schemes tend to be biased in the extreme LST

ranges [79], due to the small number of extreme LST pixels and also the presence of outliers [74].

The inconsistency in the performance of LST predictors, both in respect to time and location, is another important issue in the downscaling literature [93, 105]. This is because it complicates or even prohibits the transfer of a downscaling scheme designed for a specific area to another area with different landscape and climatic characteristics [105]. For instance NDVI-based downscaling schemes do not perform well over complex heterogeneous regions [105] and for this reason alternative approaches have been proposed, e.g. [79]. Such inconsistencies are also evident when working with different land cover types. This is because the explanatory power of a LST predictor varies in respect to land cover. For instance, the impervious surface cover is more appropriate for downscaling urban LST than NDVI [75] and vice versa. To that end, MAST, YAST and Theta offer the advantage of a stable performance over various land cover types, landscapes and climatic conditions. This is because, being derived from LST data, they incorporate the location-specific variability, e.g. the effects of topographic shading [59], and also how this variability changes with time (when multi-temporal MAST, YAST and Theta data are being used). This fact makes them especially useful for downscaling geostationary diurnal LST data. In addition, it also implies that the inclusion of YAST, MAST and Theta can help limit the size of the LST predictor set, which is more practical and performs better as some studies [82, 93] suggest. However, the good performance of the ACP depends on the multi-year time series of satellite LST data used for their estimation. Specifically the employed time series should deliver a sufficient sample size that is not affected by short weather effects and does not cover substantial changes in the climatic or surface conditions (e.g. a burnt scar) in order to be accurate [59, 80]. Otherwise artefacts may occur [59].

Another important issue that may prohibit the use of a dataset as LST predictors is the scale invariance assumption, i.e. the relationship between the LST data and LST predictors to be the same between the coarse and fine spatial scale [82, 70]. For NDVI it is known that as the spatial scale becomes finer the near-linear relationship with coarse-scale LST transforms to a trapezoid and weakens [70]. In this work, the scale invariance assumption for MAST, YAST and Theta was validated for the $4\,\mathrm{km}$ and $1\,\mathrm{km}$ spatial scales. Strong evidence that support the validity of the scale invariance assumption for MAST, YAST and Theta for finer scale resolutions are available

in [82], where the ACP were used in conjunction with other LST predictors to downscale a SEVIRI scene down to $100\,\mathrm{m}$ (RMSE $= 2.2\,\mathrm{K}$). However, more detailed tests are still required.

2.6 Concluding Remarks

This chapter discusses the downscaling of geostationary diurnal LST data with the use of multi-temporal LST predictors and assesses if MAST, YAST and Theta can improve the downscaling performance. The rationale behind this work is that multi-temporal MAST, YAST and Theta are able to provide information about the spatial distribution of the LST for different times-of-day and thus improve the estimation of DLST and DLST diurnal changes, both in terms of magnitude and pattern shape. The results of this research support the aforementioned hypothesis. The SEVIRI ACP-based DLST data showed a better similarity and lower RMSE and MAE values with the reference MODIS data in comparison to DLST data estimated using a set of only static LST predictors. In addition, the findings of this work suggest that the ACP improved the DLST spatial patterns—especially for the nighttime data—and also the distribution of the DLST diurnal range values. Overall, the use of MAST, YAST and Theta as LST predictors offers many advantages to the downscaling process and can prove an important step towards the maturing of this technology. This is important because at the moment LST downscaling is the main way to obtain LST data that match the characteristic scale of the LST diurnal cycle.

Chapter 3

Assessing the DLST Spatiotemporal Inter-relationships

3.1 Introduction

The downscaling of frequently acquired geostationary LST data has the potential to compensate the lack of high spatiotemporal LST datasets [55, 56]. To achieve this goal, the key idea is to retrieve a time series of temporally dense geostationary LST data (e.g. quarter-hourly SEVIRI data) and then to *individually* downscale each LST image to the desired GSD. However, because LST downscaling algorithms by design do not consider any information from the other LST images, they can potentially distort the spatiotemporal interrelationships of the time series.

For LST data these interrelationships are especially pronounced and also highly dependent on the geographic location, the time-of-day and the season [2]. In particular, under clear-sky and fair-weather conditions the diurnal evolution of the LST follows a periodic temporal pattern where the LST smoothly increases during daytime and smoothly decreases during nighttime. Short-term weather effects (e.g. heatwaves) and seasonal effects (e.g. changes in vegetation phenology) affect this temporal pattern [106]. In detail the spatiotemporal features caused by short-term weather effects are evident in the LST time series as brief but pronounced changes in LST, e.g. a heatwave is recorded as an extreme increase of the LST for a small number of consecutive days [107, 108]. On the other hand, seasonal effects are more subtle and only observable when examining long time series, e.g. the gradual cooling from summer to winter. Short-term and seasonal effects also affect the spatial distribution of LST. For instance a heatwave can intensify SUHI hotspots [109], while the phenological cycle of croplands or deciduous forests can affect the shape of the LST spatial

patterns.

Today there is very little understanding about the impact of LST downscaling on the spatiotemporal interrelationships of the generated DLST time series. This is because current research focuses mostly on testing new combinations of regression tools and LST predictors. In addition, because LST downscaling is rather recent, there are only very few studies that use DLST datasets so as to monitor an environmental variable (e.g. [110]) and thus several limitations may still be unnoticed. Hence further research is required so as to better understand the impact of this image processing operation on LST time series. This is important if LST downscaling algorithms are to be used operationally and by non-experts.

3.2 Experimental Setup

3.2.1 Research Objective and Assessments Tests

This chapter is concerned with the impact of LST downscaling on the spatiotemporal interrelationships of long DLST time series. Ideally, LST downscaling algorithms should produce DLST data accurately and consistently and DLST time series where the diurnal evolution of the data is artefact-free and synoptic weather effects and seasonal features are reproduced in greater spatial detail. To investigate this research question, a three-month long time series of quarter-hourly LST is downscaled to a GSD of $1\,\mathrm{km}$ (from a GSD of $4\,\mathrm{km} \times 5\,\mathrm{km}$) and the following three issues are examined:

1. the accuracy, reliability, and consistency of the downscaling method;
2. the formed DLST spatial patterns, and;
3. the capability of the generated DLST time series to emulate the diurnal and seasonal characteristics of the original LST time series.

To address each issue a set of relevant key-aims was identified and targeted tests were devised as discussed below and presented in Table 3.1. These tests are based either on the LST *cross-validation* method [1] or the exploitation of the high temporal resolution of the employed quarter-hourly LST data. The LST cross-validation method is a widely-used LST evaluation method that can be applied anywhere in

Table 3.1: The identified key aims for addressing the raised DLST assessment issues and the proposed evaluation tests.

Issue	ID	Aim	Test
1	a	Quantification of the difference between the DLST and the reference LST time series.	Statistical measures at the fine resolution (1 km).
1	b	Downscaling performance with respect to land cover type.	RMSE spatial distribution.
1	c	Downscaling method's consistency assessment.	Image-to-image analysis between DLST and reference LST.
1	d	Assessment of DLST when no coincident reference LST are available.	Statistical measures at original resolution (4 km).
2	e	Assessment of formed pattern's shape, size, and location.	DLST and reference LST Local Moran Indices (LMI) comparison.
2/3	f	Compliance of DLST and original LST pattern diurnal evolution.	LMI juxtaposition and visual inspection.
2/3	g	Magnitude of diurnal spatial change.	Similarity between the first image of the day and the rest.
2/3	h	Smoothness of DLST diurnal spatial change / Artefact formation due to ACP's sudden change.	Similarity between sequential quarter-hourly images.
3	i	Preservation of original radiometry.	Min./Mean/Max. LST-DLST value comparison.
2/3	j	DLST potential to emulate the spatial changes due to seasonal effects.	Similarity between sequential images.

the world on the condition that independent high-quality LST image data are available [1]. This method is especially advantageous to alternatives, such as the ground-based temperature-based method, since the availability of ground truth LST data around the globe is extremely limited [1]. In this assessment study the LST data used for downscaling are from SEVIRI (see §1.4), while those used for evaluation are from Terra and Aqua MODIS. Both datasets cover the same time period, i.e. DOYs 152 to 243 (corresponding to June, July and August of 2014; the rationale for selecting these DOYs is explained in Chapter 2 in §2.3.5) and depict the same study area, i.e. Rome greater region (Figure 2.3). The SEVIRI data are from the IAASARS/NOA system[1] [86] (see §2.3.3 for more details regarding data accuracy), while the MODIS LST are

[1]The in-house LST retrieval algorithm used by IAASARS/NOA takes as input the cloud-free radiances of the 10.8 µm and 12.0 µm SEVIRI TIR bands [85, 86]. This algorithm is based on the Automatized Atmospheric Absorption Atlas (4A/OP) radiative transfer model in conjunction with a SVM, and information from the Thermodynamic Initial Guess Retrieval (TIGR) dataset. In particular at the start of operation of the IAASARS/NOA system the 4A/OP radiative transfer model and the TIGR dataset have been synergistically employed so as to generate a dataset of simulated 10.8 µm and 12.0 µm at-sensor radiances associated with various LSTs, emissivities and atmospheric conditions. This simulated dataset is employed as training set for the SVM and is essentially the core of IAASARS/NOA LST retrieval algorithm. In addition to the SEVIRI at-sensor TIR radiances, IAASARS/NOA also requires as input the corresponding emissivity values retrieved from MOD11A2 data product [83].

the version 5 MOD11A1 and MYD11A1 data products. As discussed in Chapter 2 the two time series have different spatiotemporal characteristic: SEVIRI offers LST data of Rome greater region with a GSD of $4\,\mathrm{km} \times 5\,\mathrm{km}$ 96 times every day (one image every 15 min), whereas MODIS provides $1\,\mathrm{km}$ LST data 4 times every day (two at noon: 10:30 and 13:30 UTC, and two at night: 01:30 and 22:30 UTC; morning and afternoon data are not available). Moreover, the two satellite instruments view the study area with different VZA (θ) and azimuth (ϕ) angles. For SEVIRI θ is constant and equal to $+50°$, while for MODIS it ranges from $-55°$ to $+55°$ (the plus sign means the sensor view the area from west, while the minus sign from the east). In this work only MODIS data acquired with a positive VZA are considered. This is so as to avoid any comparisons between LST data sampled by opposite directions and to retain a large enough evaluation dataset. Overall for this work 6470 SEVIRI images (on average 71 images per day; only images with a $< 30\%$ cloud cover are used) and 92 Terra and Aqua MODIS (47 daytime and 45 nighttime) LST images are used. The time distribution of the utilised data is presented in Figure 3.1. From this figure it is clear that the used data are well distributed throughout summer 2014 and also throughout each day, with some exceptions due to high cloudiness. In most cases two MODIS images are available for each day, covering sufficiently the time span of interest (MODIS data are available for 50 of the 90 days covered by this study).

For addressing the downscaling method's accuracy, reliability and consistency (*issue 1*), four major tests (Table 3.1, tests a to d) are used, namely (i) the quantification of the SEVIRI DLST and MODIS LST time series differences; (ii) the assessment of the RMSE spatial distribution; (iii) the estimation of the downscaling method's performance on an image-to-image basis; and (iv) the comparison of the generated DLST data (upscaled to the original coarse resolution) with the corresponding original SEVIRI LST data. For quantifying the differences between the $1\,\mathrm{km}$ DLST and reference MODIS LST time series several descriptive statistical measures, namely the mean difference, the standard deviation, the RMSE (Eq. 2.6), and the Rho (Eq. 2.8) are calculated. This analysis is performed separately for each one of the four MODIS overpass times and uses only the MODIS pixels where the LST retrieval accuracy is equal or better than $1.0\,\mathrm{K}$ (the accuracy information is derived from the MODIS quality assurance layer supplied with each MOD11A1 and MYD11A1 LST product as discussed in [85]).

In addition to the above, the RMSE spatial distribution is also estimated for each

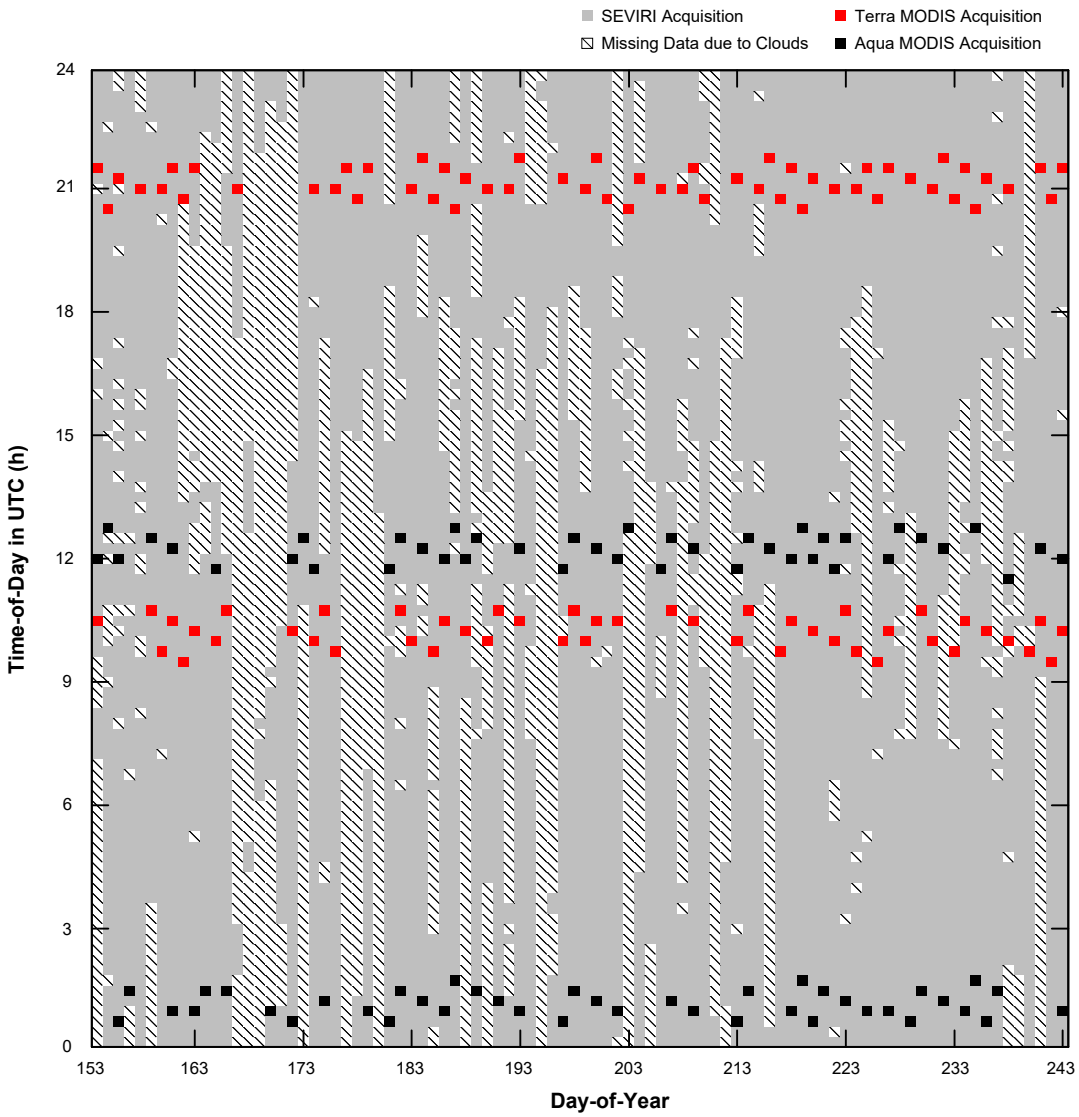

Figure 3.1: The time distribution of the employed Summer 2014 SEVIRI and MODIS LST data.

MODIS overpass time (Table 3.1 test b). This test aims to assess the downscaling performance in respect to land cover type; to highlight the differences between the daytime and nighttime data; and to identify any regions with persistently high RMSE. The third test (Table 3.1 test c) concerns the assessment of the methods reliability and consistency. For this purpose the RMSE and Rho values are estimated separately for the 47 daytime and 45 nighttime MODIS-coincident DLST data and the consistency with time is examined. The last test for addressing issue 1 is the comparison of the generated DLST data with the original coarse resolution SEVIRI LST data (Table 3.1 test d). For this purpose all 6470 SEVIRI images are employed and several statistical measures are calculated. In particular, the DLST data are upscaled to $4\,\mathrm{km}$ using the pixel-assignment method discussed in §2.3.6 and then divided into 96 groups

(corresponding to each SEVIRI quarter-hourly acquisition time). For each group the analysis of the data is based on the distribution of LST differences, the mean difference, the RMSE, and the Rho statistical measures.

The assessment of the formed DLST spatial patterns (*issue 2*), is required since the downscaling method can form unwanted artefacts. To facilitate the assessment of the spatial thermal patterns the Local Moran Index (LMI) is employed, which is an established spatial analysis tool for the detection of spatial clusters [111]). The LMI identifies the prevalent hotspots by comparing individual locations with their neighbourhood using Eq. 3.1. In Eq. 3.1 z_i is the pixel value at location i, n is the sample number, m_2 is an estimate of variance (calculated as $\sum_i \left(z_i^2/n\right)$), and w_{ij} is a distance-based weight for the pixel j included in the neighbourhood of pixel i. The application of the LMI leads to the generation of a new image depicting the prevalent thermal patterns.

$$\mathrm{LMI}_i = \frac{z_i}{m_2} \sum_j \left(w_{i,j} z_j\right) \tag{3.1}$$

To assess the formed spatial patterns (Table 3.1 test e), the SEVIRI DLST-derived LMI images are compared with the corresponding daytime and nighttime MODIS LMI. Specifically, the three month-mean, MODIS-coincident DLST images are estimated and then employed for calculating the LMI. This is done so as to minimize the influence of local short-term weather effects. The evaluation of the retrieved LMI is performed by comparing the location, the shape and the size of the prevalent thermal clusters with the ones derived from the MODIS data.

Lastly, for addressing the capability of the generated DLST time series to emulate the diurnal and seasonal characteristics of the original LST time series (*issue 3*), three tests are used. The first test concerns the assessment of the spatial pattern diurnal evolution (Table 3.1 test f). For this test the 6470 SEVIRI images included in each dataset (i.e. the $4\,\mathrm{km}$ LST, and the $1\,\mathrm{km}$ and $4\,\mathrm{km}$ DLST time series) are divided into 96 groups (according to their acquisition time) and averaged. Then the LMI is calculated separately for each three-month mean image to minimize the weather effects. The analysis of the retrieved LMI data is performed in three stages. Firstly, the $1\,\mathrm{km}$ DLST-derived LMI data are juxtaposed with the corresponding $4\,\mathrm{km}$ LST-derived LMI data for assessing the agreement of the corresponding spatial patterns. Then, the magnitude of the spatial pattern diurnal change (Table 3.1 test g) is examined

by calculating the Rho between the 00:00 UTC image with each one of the following 95 as shown in Figure 3.2a (the $4\,\mathrm{km}$ LST data are used as reference). Finally, the smoothness of the diurnal DLST pattern evolution is assessed by estimating the Rho between sequential quarter-hourly images as shown in Figure 3.2b (test h in Table 3.1). In particular, it is assumed that the 15 min SEVIRI data acquisition frequency is too short for any major spatial pattern change to take place. Hence, the Rho between sequential quarter-hourly mean LST/LMI data should be close to 1. The impact of the sudden change of the ACP LST predictors is also assessed using the aforementioned *autocorrelation* tests.

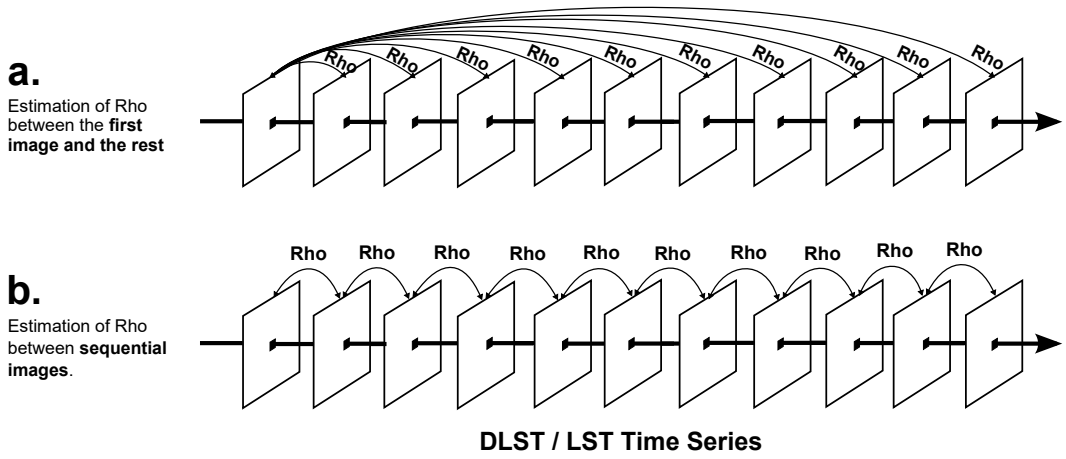

Figure 3.2: A graphical representation of the autocorrelation tests performed for assessing the spatiotemporal features of the DLST time series.

For the second test of issue 3, the $1\,\mathrm{km}$ mean, minimum, and maximum DLST values of each generated image are compared with the corresponding $4\,\mathrm{km}$ LST values so as to assess if the original radiometry is preserved (Table 3.1 test i). The third test focuses on the spatial changes due to seasonal effects (Table 3.1 test j) . In detail, it is assumed that for a long but finite time period, as the period under study, the Rho between the first MODIS image (i.e. the one acquired first) and each one of the rest (in a sequential manner similar to Figure 3.2a) should exhibit a smooth declining trend. This trend would be due to seasonal effects and the DLST data should replicate it.

3.2.2 LST Downscaling Methodology

The downscaling of the SEVIRI LST time series used in the above experiments is performed using the method proposed in [56] and evaluated in [85]. This method utilises as a regression tool a SVM that is coupled with *gradient boosting* [112] and is

selected because it has been designed for use with geostationary diurnal LST data. The employed SVM is the B-SVR Light SVM [113, 114], which is an implementation of Vapnik's SVM [115] for solving the problems of pattern recognition, regression and learning a ranking function. The SVM is preferred over other regression tools because it has limited requirements on training dataset size and quality; it is effective in terms of noise reduction and computation efficiency; and its self-adaptability makes it better suited to describe the complex relationship that connects the diurnal LST data with the LST predictors [78, 116]. Gradient boosting is a *machine-learning* concept for forming model ensembles by sequentially combining several weak models into a much stronger one. To achieve this the key idea is, at each iteration, to train a new model that is maximally correlated with the negative gradient of the loss function[2], associated with the error of the whole ensemble [117]. Here, the employed form of gradient boosting is an additive formula that minimises the loss function of the observed coarse resolution LST residuals by appropriately weighting and combining several model runs. In detail, additive gradient boosting fits simultaneously several base-learner candidates atop some randomly chosen variables, and then selects the best of these models based on the residual sum of squares criterion [117]. In this work the gradient boosting method is used instead of the DLST residual correction method (Eqs. 2.3 and 2.4 in §2.3.6) utilised in the downscaling method of Chapter 2.

The workflow of the employed SVM-based downscaling method follows the standard three-stage procedure discussed in Chapter 2 (i.e. upscaling and coregistration; generation of a regression model; application of this model to the fine resolution LST predictors) and is individually applied to each coarse resolution SEVIRI image. The LST predictors employed in this study are the 14 predictors (Figure 3.3) used originally in [56] and the 12 MODIS ACP LST predictors used in Chapter 2 (Figure 2.4). The original 14 LST predictor are: topography data, land cover data, emissivity data and VIs. In particular the topography data are from the SRTM DEM [89] and consist of the altitude, the slope and four aspect maps (one for each of the four main directions: North, South, West, and East). The land cover data are from the GlobCover dataset [118] (aggregated to four major classes, namely: water bodies, urban areas, agricultural areas, and vegetated regions, and then decomposed to

[2] According to the task at hand, the employed gradient boosting loss function can take many forms, such as Gaussian, Laplace, Binomial etc. [117].

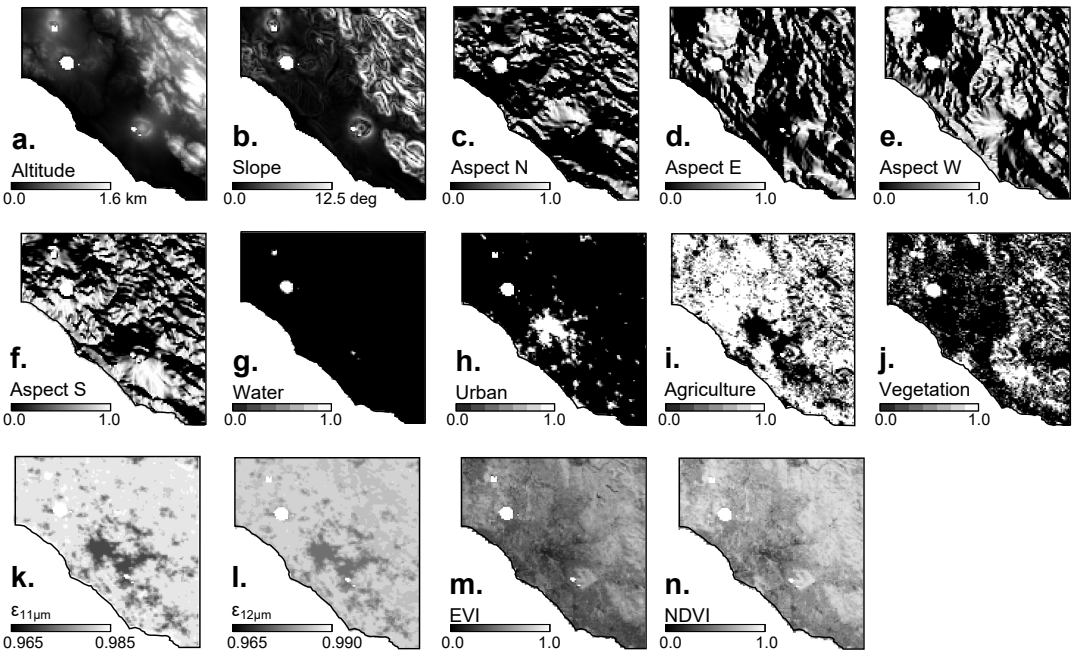

Figure 3.3: The employed topography, land cover, emissivity and VIs LST predictors used for downscaling SEVIRI LST data of Rome greater region.

provide percentages of specific land cover for each pixel). The emissivity data are the 8-day MOD11A2 band 31 (11 μm) and band 32 (12 μm) [83], while the VIs are the 16-day MOD13A2 NDVI and Enhanced Vegetation Index (EVI) VIs [90].

The aforementioned LST predictors correspond to two major categories: the time-independent (static) predictors and the time-dependent (dynamic) predictors. The topography data, as well as the land cover maps fall in the first category, while the rest of the predictors fall in the second category. The time-dependent predictors are further divided into those that change on a weekly or biweekly basis (i.e. the emissivity and the VIs) and those that change within a day (i.e. the MAST, YAST and Theta ACP). Hence, for downscaling the three-month long SEVIRI time series, the emissivity and the VI LST predictors are updated every 8 and 16 days, respectively; while the ACP are successively changed on a daily basis. In particular, the Aqua nighttime MAST, YAST and Theta are set in use at 23:30 UTC, the Terra daytime at 06:00 UTC, the Aqua daytime at 11:30 UTC, and lastly the Terra nighttime at 17:30 UTC. To that end, the estimation of intermediate ACP from other satellite data was not possible at this stage, while the option to estimate intermediate MAST, YAST or Theta as the average of consecutive ACP was not considered as an option because this would not be valid. The sequential change of the ACP data is expected

to raise two problems: first the sudden change of the ACP will affect the smooth evolution of the DLST spatial patterns and secondly the use of the night and noon ACP during morning and afternoon hours will impact the formed DLST spatial patterns for these time periods. Nevertheless, the inclusion of the ACP is considered significant because, being derived from fine-resolution thermal data, they can explain a lot of the LST spatial variation and facilitate the formation of correct DLST spatial patterns, as shown in Chapter 2. In addition, the use of a large number of diverse predictors in conjunction with the SVM is expected to minimize the aforementioned problems (for assessing this issue targeted tests are performed).

For the upscaling and co-registration of the fine-resolution LST predictors to the coarse-resolution LST data, the pixel assignment method discussed in §2.3.6 is used. The coarse-resolution LST predictors are then estimated as the mean of the selected fine resolution pixels that fall inside each coarse-resolution pixel, with the exception of the slope and aspect data that are re-calculated from the coarse resolution mean altitude data. Prior to upscaling, all LST predictors are min-max normalized between -1 and 1 so as to have comparable values and reprojected to a common $1\,\mathrm{km} \times 1\,\mathrm{km}$ grid. After the development and application of the regression model a spatial 3×3 averaging filter is also applied to each DLST image so as to make the generated DLST more physically realistic and also to remove any artefacts.

3.3 Results

3.3.1 Accuracy and Consistency Assessment

The first aim of the evaluation process is to provide an accuracy estimation of the retrieved SEVIRI DLST data through comparisons with the corresponding MODIS LST data. The results (Table 3.2 and Figure 3.4) are consistent between day- and nighttime. The mean difference (bias) is close to $0\,\mathrm{K}$ in almost every case, with the exception of the 10:30 UTC data where the SEVIRI DLST time series is warmer by $1\,\mathrm{K}$. Furthermore, the calculated LST differences are more disperse for daytime (σ of $3\,\mathrm{K}$) than for nighttime (σ of $1\,\mathrm{K}$) data. The superiority of nighttime results, which is a trend reported in most downscaling works (e.g. [55]), is also evident for RMSE ($3\,\mathrm{K}$ for daytime and $1\,\mathrm{K}$ for nighttime). Rho is equal to 0.86 for daytime and 0.9 for nighttime comparisons.

Table 3.2: Various statistical measures quantifying the difference of the DLST diurnal range data with the reference LST data.

Statistical Measures	01:30 UTC	10:30 UTC	13:30 UTC	22:30 UTC
Bias (K)	-0.5	1.0	0.0	0.0
σ (K)	1.0	3.0	3.0	1.0
RMSE (K)	1.0	3.0	3.0	1.0
Rho	0.88	0.85	0.86	0.91

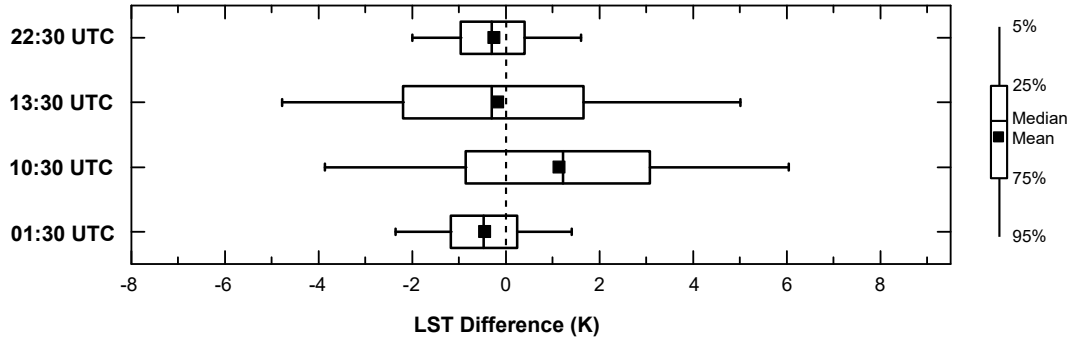

Figure 3.4: The distribution of the LST differences between the generated $1\,\mathrm{km}$ DLST and reference LST datasets.

3.3.2 Analysis of the RMSE spatial distribution

The performance of the downscaling process is not the same for every pixel but depends on land cover type and topography [97]. To assess this issue the spatial distribution of the RMSE for each MODIS overpass time is presented in Figure 3.5. From Figure 3.5 it is evident, that every pixel—regardless of land cover type—has a higher RMSE in daytime than in nighttime, and that the daytime RMSE spatial patterns are considerably more complex than the nighttime (in accordance with [97]). In particular, the Apennine Mountains daytime and nighttime RMSE values are approximately $6.0\,\mathrm{K}$ and $1.0\,\mathrm{K}$, respectively, making it the most pronounced daytime spatial feature. For the city of Rome the corresponding RMSE values are $3.5\,\mathrm{K}$ and $2.5\,\mathrm{K}$, respectively and it is the most prominent nighttime feature. The rural area pixels exhibit the lowest RMSE values ($2.0\,\mathrm{K}$ for daytime and $1.0\,\mathrm{K}$ for nighttime).

The particularly high daytime RMSE values over the Apennines (Figure 3.5) are mostly due to colocation uncertainties [97] and the enhanced effective anisotropy of rugged terrain [119]. Specifically, the terrain-induced shadows cause differential heating patterns that increase the spatial heterogeneity of the LST. The enhanced LST spatial heterogeneity makes the emitting surfaces to differ even more when viewed

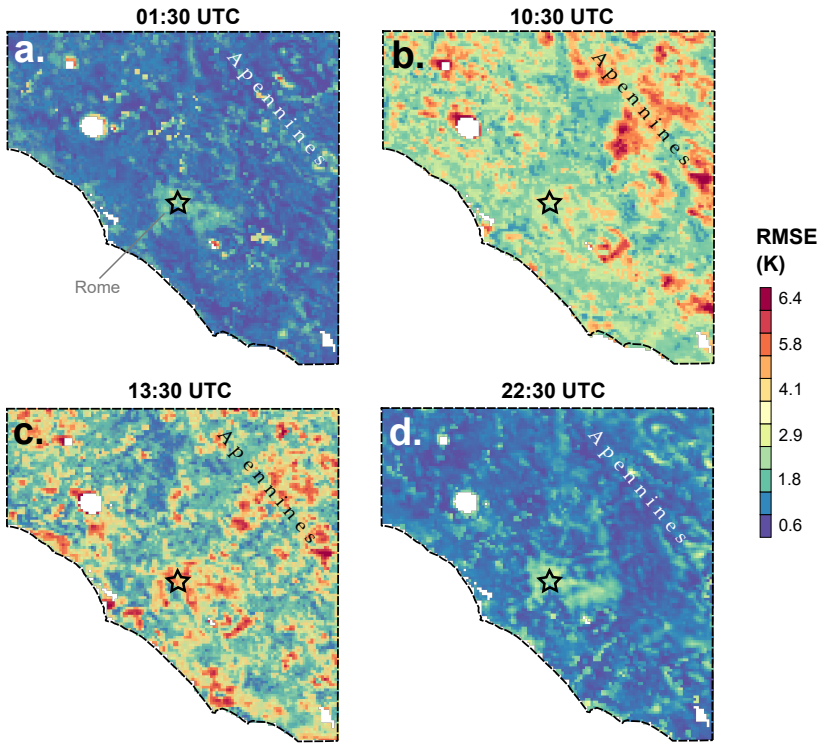

Figure 3.5: The **(a)** 01:30 UTC; **(b)** 10:30 UTC; **(c)** 13:30 UTC; and **(d)** 22:30 UTC RMSE spatial distribution.

by different angles, as is the case between SEVIRI and MODIS. Hence, the radiometric incompatibilities between the same rugged-terrain pixels are more pronounced and lead to the calculation of higher RMSE values in respect to flat regions. The influence of shadows on effective anisotropy can also explain why the daytime Apennines RMSE patterns are more pronounced for the 10:30 UTC data than the 13:30 UTC data. In particular, the increase of sun elevation from $50°$ to $70°$ during the 10:30 - 13:30 UTC period implies that the differential heating patterns caused by the sun-terrain geometric configuration become weaker with time. Hence, their influence decreases during the 10:30 - 13:30 UTC time period and so do the radiometric incompatibles between SEVIRI and MODIS for this region.

3.3.3 Assessment of the downscaling method's stability and consistency

The image-to-image RMSE and Rho values for assessing the downscaling method's stability and consistency are presented in the scatterplots and frequency histograms of Figure 3.6. Specifically, the calculated Rho values are greater than 0.7 for 86 of the available 92 MODIS-SEVIRI pairs (only for 3 daytime and 3 nighttime images the Rho was lower than 0.7); and the RMSE is consistently close to $3\,\mathrm{K}$ for daytime and

1 K for nighttime comparisons. Hence, the performance of the downscaling method is considered *consistent*.

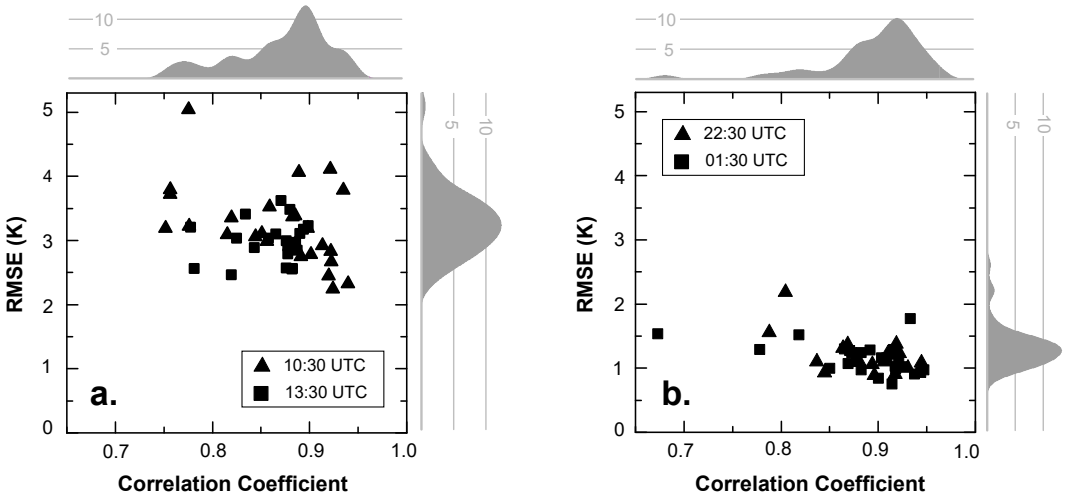

Figure 3.6: The RMSE and Rho of the SEVIRI DLST that were compared with the MODIS **(a)** daytime and **(b)** nighttime data. The corresponding RMSE (vertical) and correlation coefficient (horizontal) frequency histograms are included for each plot.

3.3.4 Comparison of SEVIRI 4 km LST and 1 km DLST time series

The hourly distribution of the LST differences between the original 4 km SEVIRI LST and the upscaled DLST time series is presented in Figure 3.7a, while the corresponding Rho and RMSE values are presented in Figures 3.7b and 3.7c, respectively. The mean LST difference is close to 0 K for all time spots under study, while the standard deviation of the LST differences is greatest for the 10:00 - 14:00 UTC time period and minimum for the 00:00 - 09:00 UTC and the 17:00 - 24:00 UTC time periods. The RMSE shows a similar pattern: the RMSE is equal to 1 K in the morning hours until 09:00 UTC and then it starts increasing. At 14:00 UTC it reaches its maximum value (approximately 2 K) and then starts to fall back to 1 K. Rho is close to 0.9-0.95 almost throughout the day, with the exception of noon when it falls to 0.85. Consequently, it can be assumed that the performance of the downscaling process during morning and afternoon hours would not be as good as for night hours but better than noon.

3.3.5 Assessment of Formed DLST Spatial Patterns

In Figure 3.8 the predominant spatial thermal clusters as derived by the 10:30 UTC and 22:30 UTC MODIS and the corresponding DLST data are presented, respectively

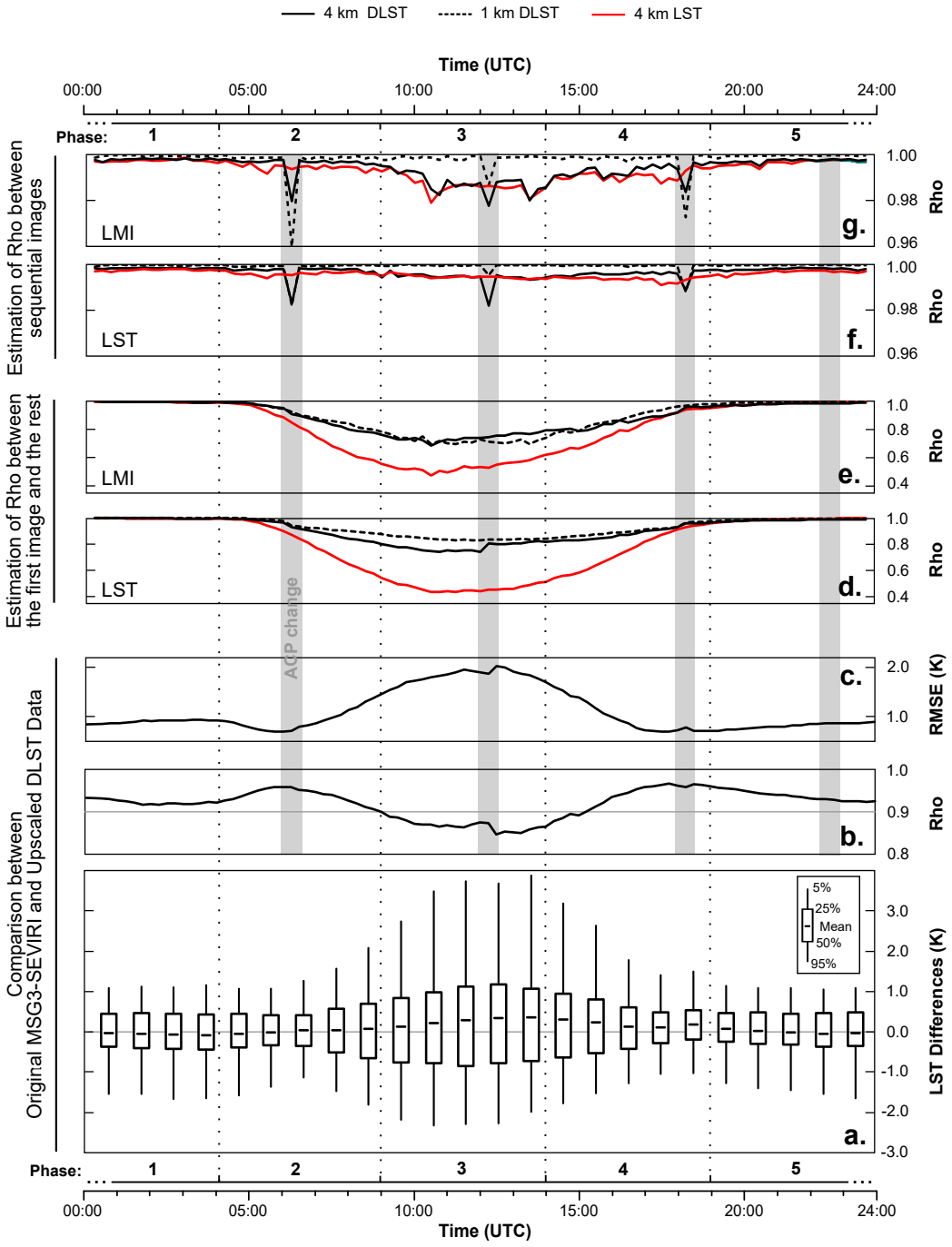

Figure 3.7: The **(a)** mean difference and the distribution of LST differences, **(b)** Rho, and **(c)** RMSE between the DLST (upscaled to 4 km) and original coarse scale SEVIRI LST data. The Rho between the first mean **(d)** LST and **(e)** LMI image and the rest (both for 4 km and 1 km). The Rho between sequential mean **(f)** LST and **(g)** LMI images (both for $4\,\mathrm{km}$ and $1\,\mathrm{km}$).

(the 13:30 and 01:30 UTC data are similar with the aforementioned). In general, the same major clusters are present between the MODIS LST and SEVIRI DLST data. However, none of the DLST images emulate the spatial features visible in the MODIS LST data with the same sharpness and contrast (they appear somewhat blurry).

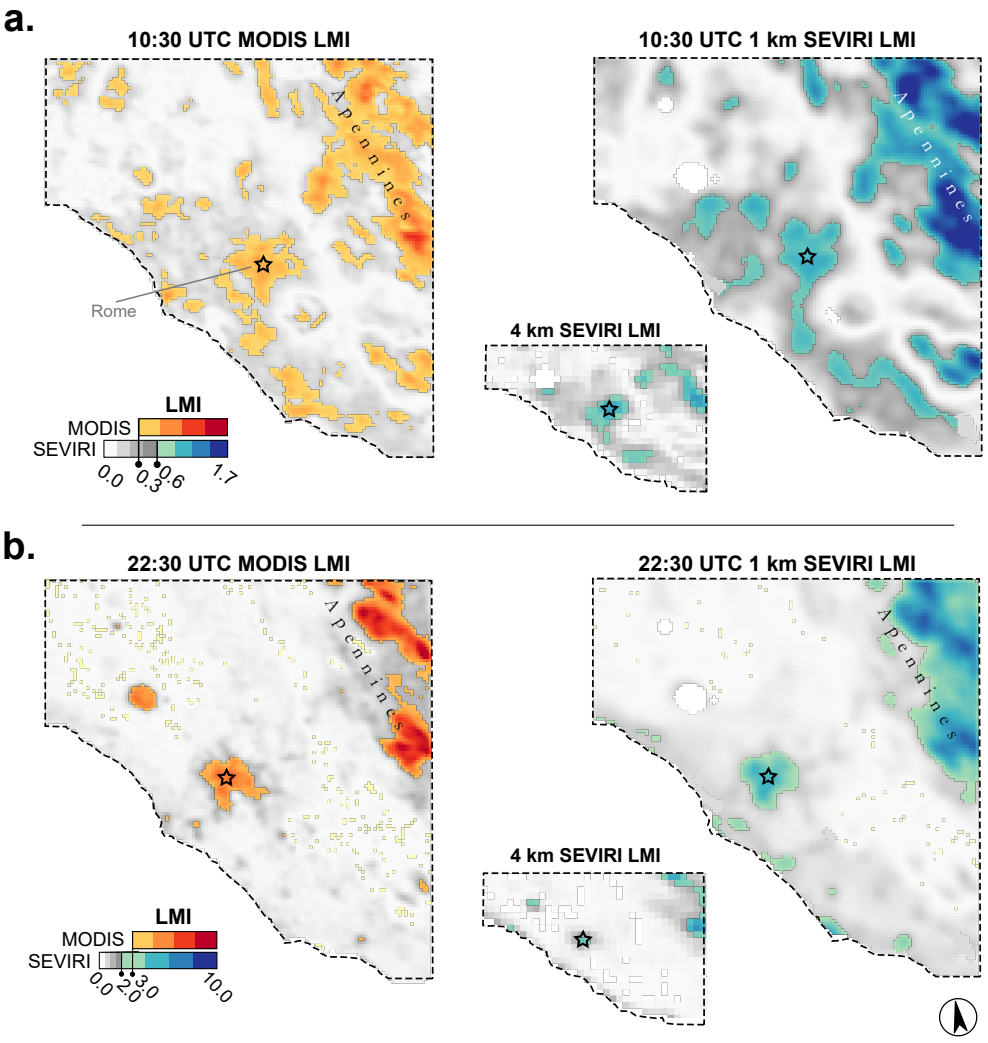

Figure 3.8: The 3-month mean MODIS LMI and SEVIRI 1 km and 4 km LMI images for **(a)** 10:30 UTC and **(b)** 22:30 UTC. The prevalent thermal clusters are highlighted (tones of blue for SEVIRI and tones of red for MODIS).

The high homogeneity of the DLST data affects the extraction of spatial information from the generated data. In this work, the high similarity of adjacent DLST pixels led to the estimation of larger LMI clusters and higher LMI values, and thus to the extraction of larger hotspots. This is evident especially for the daytime data (Figure 3.8a), where the dominant MODIS LMI (orange shapes) and SEVIRI DLST LMI (blue shapes) hotspots differ in size (Figure 3.8a). For the 22:30 UTC data (Figure 3.8b) the blurriness impact is minor since the nighttime LST values are intrinsically homogeneous. In general, the nighttime LMI-derived MODIS and SEVIRI hotspots are similar (Figure 3.8b).

3.3.6 Assessment of the DLST spatial pattern diurnal evolution

In Figure 3.9 the diurnal evolution of the $4\,\mathrm{km}$ LST-derived LMI and the corresponding $1\,\mathrm{km}$ DLST-derived LMI is presented. According to the $4\,\mathrm{km}$ LMI data the study area's diurnal cycle can be perceived as a five-phase cycle. During the first phase the Apennine Mountains and Rome's SUHI effect are the prevalent LST spatial features (the former remains strong throughout phase 1 and also the entire day, while the latter weakens with the passage of time). In phase 2 the rural region becomes a prevalent thermal cluster that is warmer than the city of Rome, and thus an urban sink phenomenon occurs [120]. In phase 3 the most complex LST patterns occur: at 10:30 UTC the eastern part of Rome forms a well-defined cluster that is warmer than the western part and stands out from the surrounding rural area, while at 13:30 UTC the east and west parts of Rome have similar LST values and form a unified cluster centred over Rome. During phase 4 the LST values start to drop and the rural thermal pattern weakens until it disappears. The cluster corresponding to Rome shrinks but remains prevalent. In the last phase the predominant spatial patterns are those induced by the mountainous region and Rome's SUHI, similar to phase 1 (Figure 3.9, 19:30 and 22:30 UTC). The success of the downscaling process depends on how well the DLST time series can emulate the characteristics of the aforementioned diurnal cycle.

In general, the diurnal evolution of the DLST spatial patterns follows the five-phase cycle discussed above. However, the DLST scheme did not reproduce the urban sink phenomenon observed at the 4 km 07:30 UTC LMI image (Figure 3.9c). This is an important issue because it can adversely impact the analysis of the SUHI diurnal evolution. Another issue observed is that the strength of the diurnal spatial changes is weaker in the generated DLST data than in the original SEVIRI LST data as Figures 3.7d and 3.7e reveal. Specifically, the phase 2, 3 and 4 Rho values corresponding to the DLST data are considerably higher than the reference data (red curves, Figure 3.7). This finding suggests that the increased similarity of the DLST data made the diurnal cycle changes less pronounced, and thus the generated daytime and nighttime DLST data more similar. Finally, Figures 3.7f and 3.7g show that the diurnal evolution of the DLST data is smooth as Rho is equal to approximately 1 for every case. In these figures, at the time spots where the ACP change takes place, a minor drop of 0.02 (Rho ≈ 0.98) is observable that is considered not important. Hence, it can be suggested that the use of a large number of LST predictors with a

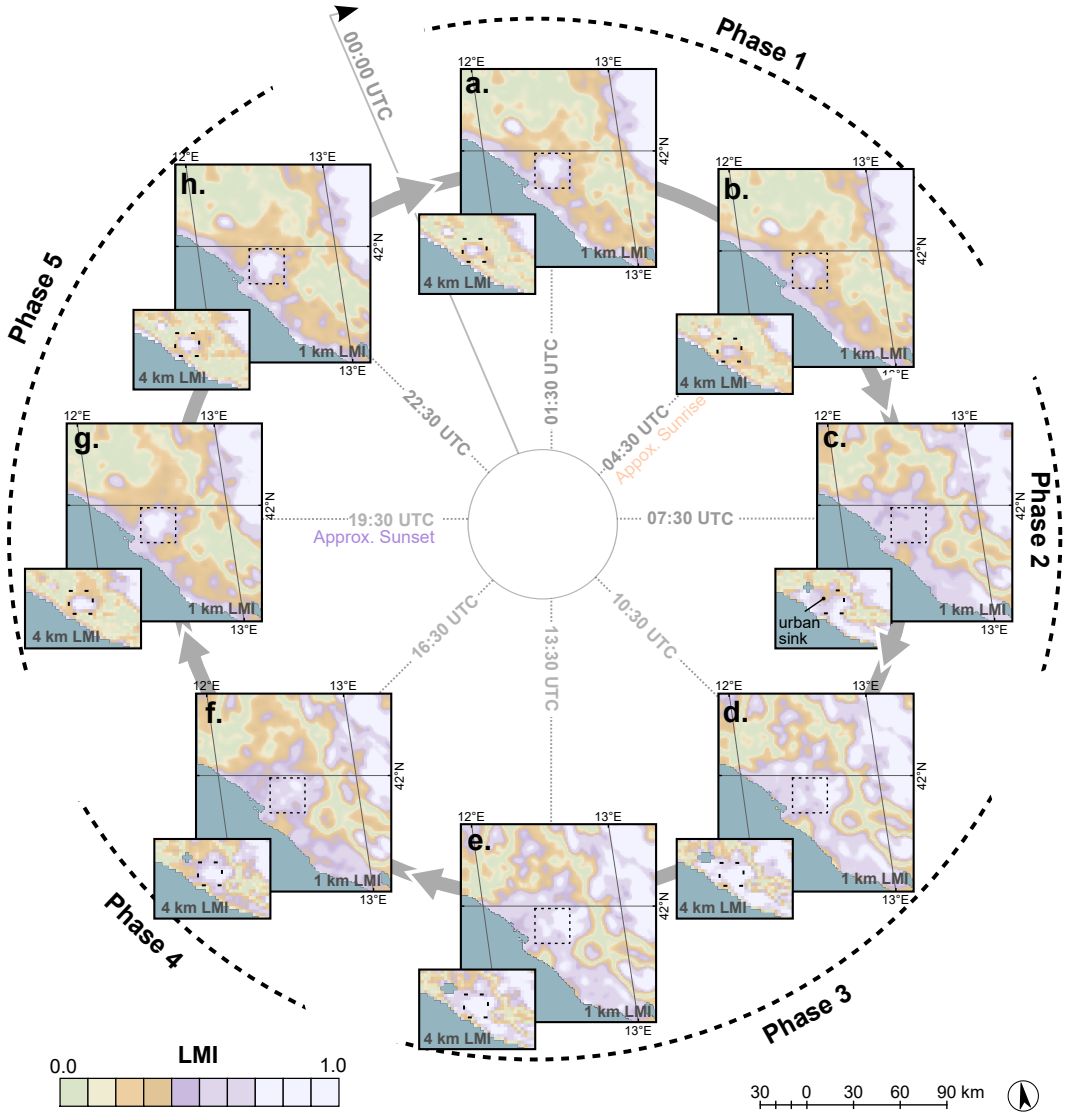

Figure 3.9: The diurnal evolution of the 4 km and 1 km SEVIRI LMI (the LMI were min.-max. normalised separately). The black squares correspond to the city of Rome, Italy.

SVM was able to compensate the sudden change of LST predictors.

3.3.7 Assessment of the DLST Potential to Emulate LST Temporal Features

The last stage of the evaluation process is the assessment of the DLST time series' potential to emulate the temporal features of the original 4 km LST time series. In Figure 3.10 the mean, minimum and maximum LST and DLST values for each image of the original SEVIRI 4 km and the generated 1 km datasets are presented for the period under study (Summer 2014). The retrieved 4 km LST and 1 km DLST values

are very similar and form a sine-wave like pattern. These two characteristics suggest that the DLST data adequately preserved the radiometry of the original data and thus were capable to retain the smooth increases and decreases of the measured 4 km LST values.

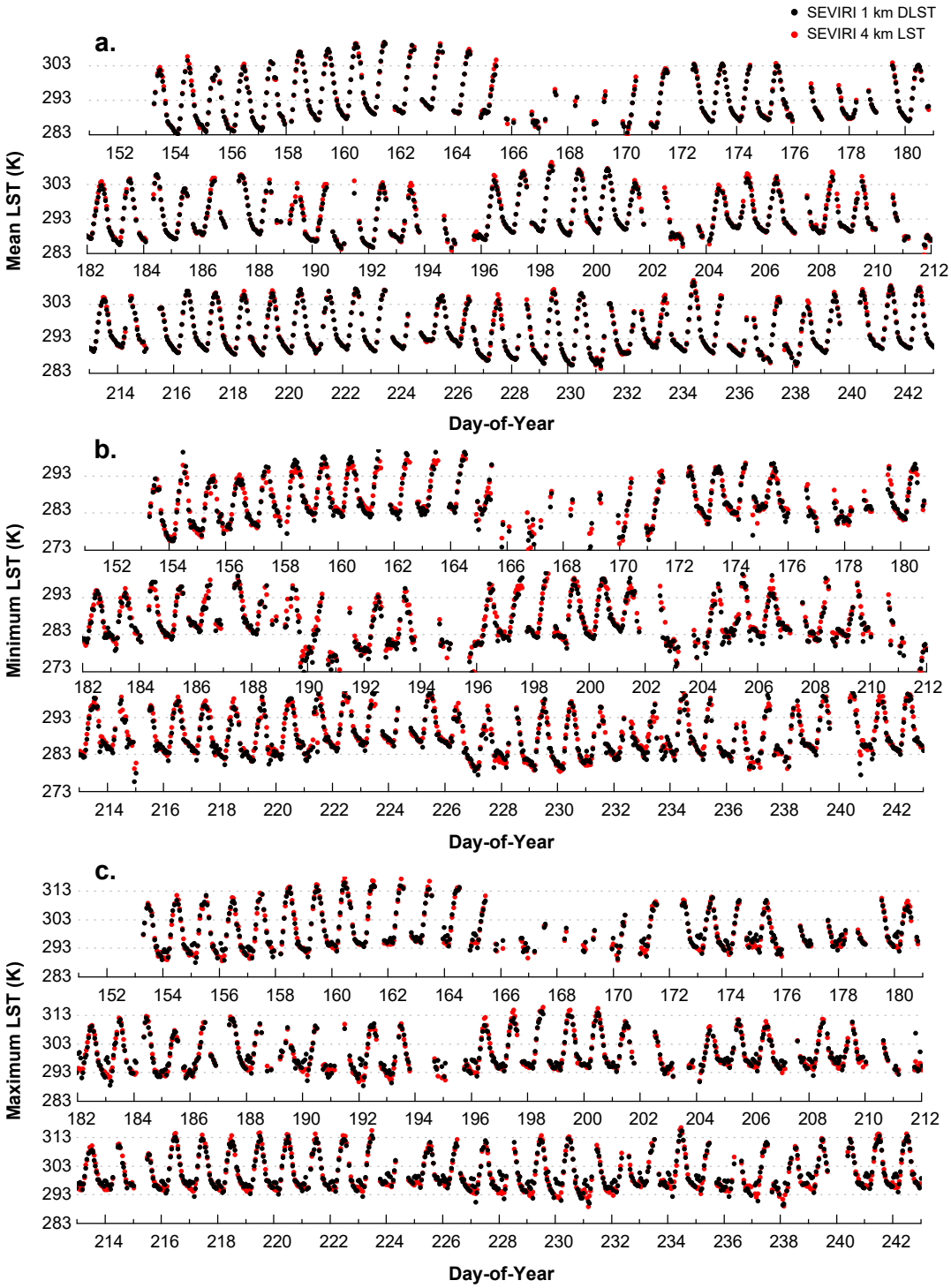

Figure 3.10: The **(a)** mean, **(b)** minimum and **(c)** maximum SEVIRI LST and DLST for summer 2014.

The long-term seasonal effects on the DLST spatial patterns are studied in Figure 3.11 by estimating the Rho between the first image of each employed dataset (i.e. the MODIS LST and SEVIRI DLST time series) and the rest (as discussed in §3.2.1 and presented in Figure 3.2a). Specifically, the expected declining Rho trend due to the seasonal effects is observable only for the daytime data but very weakly (Figures 3.11b-c). For the nighttime data the linear fits (Figures 3.11a-d) are almost horizontal. This is mostly due to the fact that the utilised data correspond to the same season of the year. The most interesting observation though concerns the magnitude of the Rho values obtained. Specifically, the MODIS Rho values are lower (by 0.1 to 0.2) than the ones derived from the SEVIRI DLST dataset. This observation hints that the generated DLST spatial patterns are more similar than the measured LST data (a similar issue was noticed when the daytime and nighttime DLST spatial patterns were compared in §3.3.6) and that the downscaling process could not represent the spatial thermal changes as pronouncedly as the measured data could.

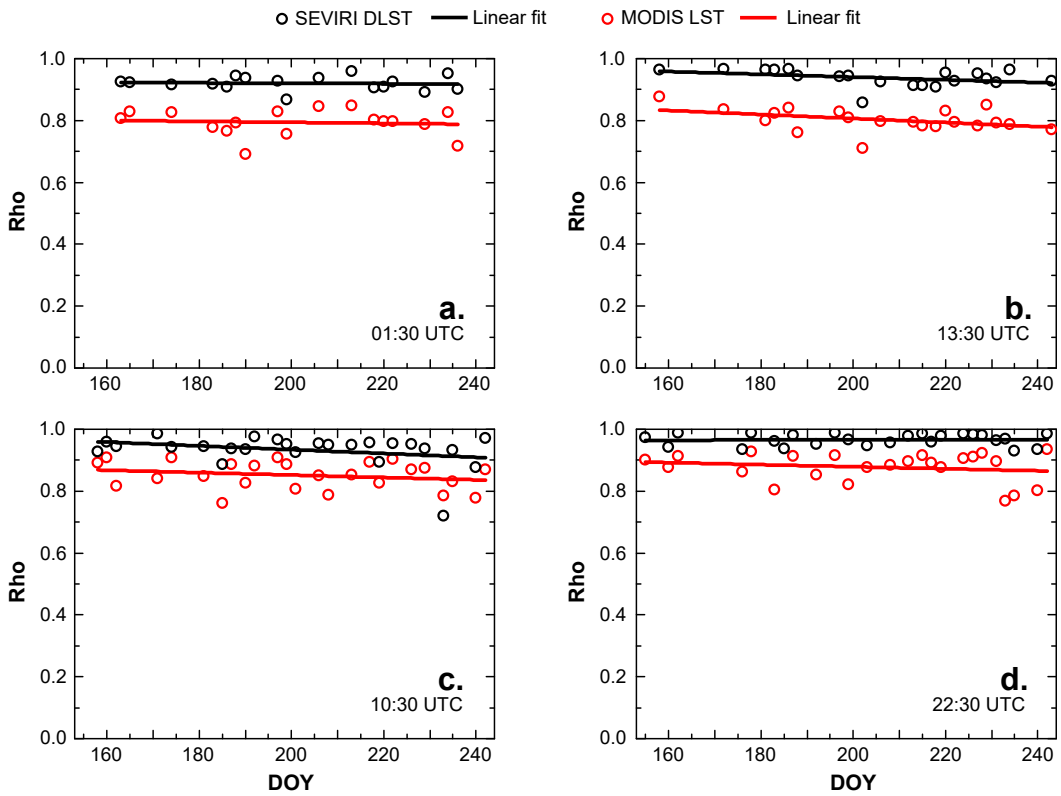

Figure 3.11: The Rho between the first 1 km LST/DLST image of each dataset and the rest.

3.4 Discussion

The downscaling of temporally-dense geostationary LST has the potential to compensate the lack of high spatiotemporal LST time series. To deem the downscaling of geostationary LST time series successful and capable to capture the spatial and temporal variations of the Earth's thermal landscape, the generated high spatiotemporal DLST time series must reproduce the spatiotemporal features of the coarse-scale LST time series with greater spatial detail. To investigate this issue, this work studied the accuracy, the correct pattern formation, and the temporal changes of a downscaled three-month long SEVIRI LST time series depicting the city of Rome in Italy and the surrounding rural area.

The results suggest that the downscaling process operated in a consistent manner, preserved the radiometry of the original SEVIRI data and generated noon, afternoon and nighttime spatial thermal patterns that were similar with those present in the evaluation data. Moreover, the results also suggest that the downscaling of urban pixels is more challenging than for rural pixels, both for daytime and nighttime images. Furthermore, the evaluation process showed that the diurnal evolution of the generated data was smooth but the autocorrelation of the $1\,\mathrm{km}$ DLST data was higher than of the original $4\,\mathrm{km}$ LST data. This suggests that the DLST data could not present subtle spatial thermal changes during the course of a day as pronouncedly as the measured data could. These findings (even though confined to this study) reveal a series of issues, that using only conventional DLST evaluating schemes (i.e. comparisons with independent LST data confined to certain time spots) would remain unnoticed. Generalising the aforementioned observations, the assessment of high spatiotemporal DLST data should consider also the following issues:

- The capability of the DLST data to accurately emulate the diurnal pattern cycle.
- The capability to detect subtle diurnal spatial thermal changes.
- The smoothness of the diurnal evolution of the DLST data.
- The consistent performance of the employed downscaling method.

3.5 Concluding Remarks

The exploitation of the DLST spatiotemporal inter-relationship for evaluation purposes can overcome some of the limitations posed by the lack of ground truth data and facilitate the assessment of the issues listed above. Presently, this matter is overlooked. However, the capability of the downscaling process to accurately emulate the DLST diurnal cycle values and patterns, and the time series' temporal characteristics is crucial. This is because these two features ultimately determine the exploitability of the DLST time series for generating added value products and services for the study of the urban thermal environment such as, the estimation of air temperature, the SUHI analysis, and the heat wave hazard assessment. Besides the difficulties and the limitations currently faced, the generation of geostationary DLST time series is an important advancement of thermal remote sensing that has the potential to compensate the lack of LST data that combine high spatial and temporal resolution.

Chapter 4

High-Resolution Characterisation of the LST Temporal Dynamics

4.1 Introduction

Information about the Earth's LST and its temporal dynamics, including diurnal, seasonal, annual and inter-annual variations, is key for calculating the exchange of energy and water between the land and the atmosphere, for mapping the thermal landscape, and for studying climate change [14, 80, 121]. The LST temporal variations are driven by the Earth's diurnal and annual cycles and are conveyed differently from place to place based on differences in geographic location, topography, meteorology, and the surface's ability to conduct, convect and store heat [1, 2, 122]. Accurate knowledge of the LST *diurnal* and *annual temperature cycles* (DTC and ATC, respectively) can lead to better understanding of the surface's thermal behavior and its physical properties [58, 59]. Additionally it can also facilitate the identification and correction of land surface model deficiencies [123].

In recent years, several studies have proposed models that are directly fitted to satellite-derived LST and approximate either the LST DTC or ATC. The primary driver of the LST DTC is the rotation of the Earth around its axis, which results in the alternation between day and night. For this reason, LST DTC models (e.g. [58, 57, 124, 125, 126]) are usually a combination of two functions, the first for modelling the sun heating effects and the second the LST decay that starts after solar noon. For instance, in Göttsche and Olesen [58] the LST DTC has been approximated by a combination of a cosine and an exponential decay function, while in Inamdar et al. [124] and Duan et al. [125] by a cosine and a hyperbolic decay function. However, when aerosols and dust are present, the use of a cosine function can result in

increased errors as demonstrated and addressed in [57]. In contrast to the LST DTC, the LST ATC is driven by the seasonal variations of the incoming solar radiation (insolation). These variations are caused by the Earth's axial obliquity to the ecliptic, which results in different LST ATCs for tropical, mid-latitude and polar regions. In the tropics the annual LST variation is comparably low and has two annual maxima (at the two equinoxes), whereas in the polar regions the LST ATC has only one maximum (at each hemisphere's summer season [127]). In mid-latitude regions, such as Europe, the ATC exhibits strong seasonality and has been effectively modelled using a sine function plus a constant term (e.g. [80, 59, 78, 128, 129, 130]).

An important advantage of LST DTC and ATC models is that they can be reduced to a set of key cycle parameters (diurnal or annual) like the LST mean, amplitude, peak time and phase shift (such parameters are the ACP introduced in §2.2). These model-derived parameters are gap-free, provide a generalised characterisation of the cloud-free LST dynamics, and are more informative and representative of the surface's thermal characteristics than individual LST measurements [59, 57]. The most accurate DTC models parameterise the LST diurnal cycle using six parameters (e.g. [57]). This implies that they require at least six LST observations per day as input, which only geostationary satellites can offer (Figure 1.8). To use DTC models with LST from polar orbiting satellites (maximum four observations per day), the users should either employ a less accurate [131] four-parameter model or fix some of the six parameters as constants [125]. In contrast to DTC models, ATC models can be fitted to LST data from both geostationary and polar-orbiting platforms without any changes or assumptions. So far ATC models have only been used with LST from polar-orbiting platforms (e.g. [80, 59, 78, 128]). Such data offer a fine GSD but limit the ATC modelling to the satellite overpass times and thus the derived cycle parameters are only snapshots that refer to certain times-of-day.

Both LST DTC and ATC models are extremely useful and for this reason considerable improvements have been achieved over the last decade. Nonetheless, modelling only the DTC or the ATC, provides an incomplete picture of the LST spatiotemporal dynamics, which vary both as a function of time-of-day and DOY. To address this gap, further research is required on the development of methodologies that simultaneously model the DTC and ATC. Such methodologies should result in cycle parameters that represent the complete diurnal and annual LST dynamics with adequate spatial and temporal detail. This chapter presents such a method.

4.2 Materials and Methods

4.2.1 Research Objective and Method Overview

The research objective of this work is to develop a methodology that can be used so as to characterise the diurnal and annual temporal dynamics of LST with increased spatial and temporal detail. To achieve this, the workflow presented in Figure 4.1 is proposed. In particular, the key idea is to iteratively fit an ATC model on diurnal geostationary data and generate several sets of cycle parameters for different times-of-day (at regular and frequent time intervals). Separately, each set of cycle parameters provides only a snapshot of the annual LST dynamics that corresponds to a certain time-of-day. When combined however, these sets can represent the complete diurnal and annual LST climatological cycle. This information is what is required for characterising the LST temporal variation, but because the cycle parameters are derived from geostationary data their GSD is too coarse. Hence, to attain the research objective set above, the spatial resolution of the derived cycle parameters should be increased.

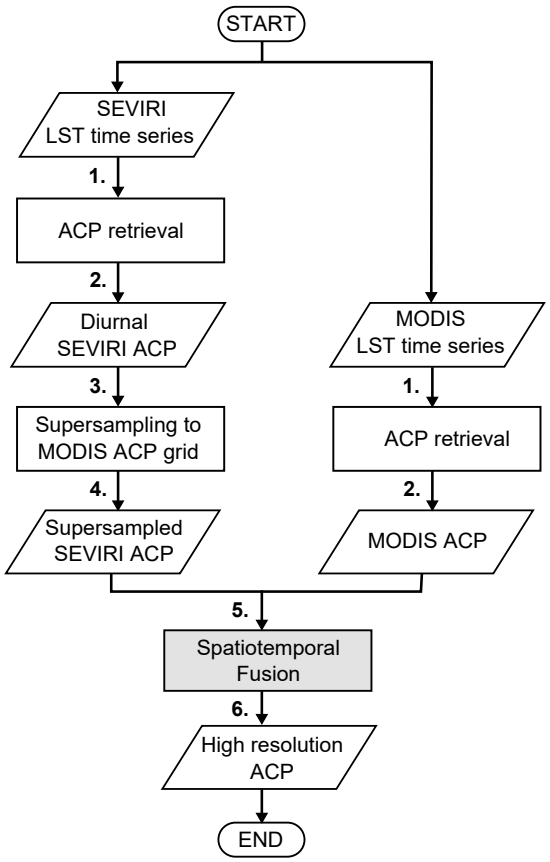

Figure 4.1: Overview of the proposed method for estimating fine-resolution LST cycle parameters.

To achieve this, the proposed method uses a *spatiotemporal fusion* scheme [132]. This image processing operation is used for blending multi-source image data, with either the desired temporal or spatial resolution, into a single dataset that retains the desired fine spatial and temporal resolution. The use of a spatiotemporal fusion algorithm is based on the availability of at least one collocated and concurrent pair of fine- and coarse-resolution image data and its workflow can be briefly described as follows: first, the algorithm establishes a relation between the radiometric and spatial information of the existing fine- and coarse-resolution image pair, and then it applies this relationship to the available coarse-resolution images so as to complete the time series of the fine-resolution data. To relate the concurrent and collocated fine (F) and coarse (C) resolution images, the algorithm assumes that over a homogeneous region a fine and a coarse-resolution pixel acquired at time t_0 ($F(x_i, y_j, t_0)$ and $C(x_i, y_j, t_0)$, respectively) would differ only due to system biases (i.e. sensor calibration, random noise, difference in SZA and scale, processing methods etc.). Thus the relationship between $F(x_i, y_j, t_0)$ and $C(x_i, y_j, t_0)$ is:

$$F(x_i, y_j, t_0) = C(x_i, y_j, t_0) + \gamma_0 \tag{4.1}$$

where, γ_0 is the difference due to system biases. Similarly, for another acquisition time t_κ, Eq. 4.1 can be written as:

$$F(x_i, y_j, t_\kappa) = C(x_i, y_j, t_\kappa) + \gamma_\kappa \tag{4.2}$$

If the land cover of the target and sensor calibrations have not changed between t_0 and t_κ, then it can be reasonably assumed that $\gamma_0 = \gamma_\kappa = \gamma$. Hence, solving Eq. 4.1 for γ and then substituting it in Eq. 4.2 gives:

$$F(x_i, y_j, t_\kappa) = F(x_i, y_j, t_0) + [C(x_i, y_j, t_\kappa) - C(x_i, y_j, t_0)] \tag{4.3}$$

Eq. 4.3 is the core idea of spatiotemporal image fusion and shows that the fine-resolution image at t_κ can be predicted from an already known fine-resolution image plus the temporal differences of the corresponding coarse-resolution image data [132]. It is important to note that Eq. 4.3 holds true only for homogeneous pixels,

which are very rare (especially at coarse resolutions). To be able to use this methodology for heterogeneous pixels, additional information is required [132]. This information is retrieved from neighbouring pixels and is introduced in Eq. 4.3 as a spatiotemporal weighting function W:

$$F(x_i, y_j, t_\kappa) = F(x_i, y_j, t_0) + W_{ijk}\left[C(x_i, y_j, t_\kappa) - C(x_i, y_j, t_0)\right] \tag{4.4}$$

Initially spatiotemporal fusion was proposed for use with reflectance data [132] but it performs well also with TIR remote sensing data, as recently demonstrated in [133, 134, 135]. This work aims to use such a scheme so as to to increase the spatial resolution of the geostationary cycle parameters by blending them with corresponding cycle parameters retrieved from fine-resolution LST data.

To test and assess the performance of the proposed method, the workflow presented in Figure 4.1 is applied on cycle parameters derived from SEVIRI LST and MODIS LST. The study area is Europe and the ATC model used for deriving the cycle parameters is the sine-based ACP model presented in [59, 80] and discussed in §2.2 of this thesis. The cycle parameters derived from this model are the mean annual LST, the yearly amplitude of LST and the phase shift from the spring equinox, which are known as MAST, YAST and Theta, respectively (Figure 2.1). Following this introductory section, the proposed method is thoroughly discussed in §4.2.2 and §4.2.3, where the retrieval of the SEVIRI and MODIS ACP and the devised spatiotemporal fusion scheme are explained, respectively.

4.2.2 ACP Retrieval

Two five-year (2009-2013) time series of LST data are used in this work for retrieving the required ACP. The first is from SEVIRI and the second from MODIS (i.e. the MOD11A1 and MYD11A1 v.6 LST product). The SEVIRI time series has a temporal resolution of 30 min (it comprises 84,386 LST images) and has been obtained from Land-SAF that operationally generates, archives and disseminates diurnal LST of Europe and Africa [87]. Land-SAF's LST are retrieved on a pixel-by-pixel basis from the $10.8\,\mu\mathrm{m}$ and $12.0\,\mu\mathrm{m}$ TIR radiances of Meteosat-10 SEVIRI with a nominal accuracy of 1-2 K [97, 136]. The LST retrieval is performed using a generalised SW algorithm (see §1.2.4) that takes also as input the land surface emissivity, the atmospheric WVC and the SZA [97]. The GSD of the employed SEVIRI data for mainland

Europe ranges from approximately $4\,\mathrm{km}$ at $35°$ to $6\,\mathrm{km}$ at $50°$N. In contrast to the SEVIRI LST, the MOD11A1 and MYD11A1 LST are available only for four time during a day and have a finer GSD of $1\,\mathrm{km}$. These data are disseminated from NASA's EOSDIS and are retrieved from the MODIS band 31 and band 32 TIR radiances using a similar generalised SW algorithm (see §2.3.3 for data accuracy and properties).

To retrieve the ACP from the SEVIRI and MODIS LST, each time series was divided into n groups according to the LST acquisition time, i.e. for SEVIRI: 00:00, 00:30, 01:00, ..., 23:30 UTC ($n = 48$) and for MODIS: 01:30, 10:30, 13:30 and 22:30 equatorial crossing time ($n = 4$). Next the LST data of each group were stacked according to their acquisition day-of-cycle ($d \in [1, 2, ..., 365]$) and each group's stack was fitted with the ATC model of Eq. 4.5. The fitting was performed on a pixel-by-pixel basis as discussed in [59] using a least square optimization.

$$\widehat{T}_{\mathrm{s}}(d) = \mathrm{MAST} + \mathrm{YAST}\sin\left(\frac{2\pi}{365}d + \mathrm{Theta}\right) \tag{4.5}$$

For each LST group, the model fitting was conducted[1] on a server with 4 sockets of AMD Opteron (Abu-Dhabi) 6386 SE (16 cores each, 1.4 to 2.8 GHz) and 256 GB RAM using an unconstrained nonlinear optimization algorithm (see [59] for details). The derived ATC models were then reduced to n sets of MAST, YAST and Theta image data (i.e. 48 for SEVIRI and 4 for MODIS).

For use in the spatiotemporal fusion scheme, the SEVIRI ACP were then reprojected from the geostationary satellite view projection to a regular grid of $0.05° \times 0.05°$ and corrected for time differences. In particular, because the original land-SAF LST data are in UTC time (Coordinated Universal Time; t_{UTC}), so are the derived ACP data. This implies that pixels of the same image correspond to different local solar times (t_{solar}) and hence to different phases of the LST diurnal cycle [137]. These time differences are a function of longitude (Λ) and for mainland Europe they can range between -0.7 h at $10°$W and +2.0 h at $30°$E (they are 0 over the Greenwich meridian, $\Lambda_{\mathrm{Greenwich}} = 0°$). Hence to address this issue Eq. 4.6 was employed for converting the t_{UTC} (where t_{UTC} = 00:00, 00:30, 01:00, ..., 23:30 UTC) of each SEVIRI pixel to the corresponding t_{solar} values.

$$t_{\mathrm{solar}}(\Lambda) = t_{\mathrm{UTC}} + \frac{\Lambda}{15°} \tag{4.6}$$

[1]The model fitting was conducted by Dr. Benjamin Bechtel at the Institute of Geography of the University of Hamburg in Germany.

Then, using the derived t_{solar} values, each pixel's MAST, YAST and Theta were linearly interpolated for every 30 min starting from 00:00 local solar time. The result of this process is a time-consistent set of three SEVIRI data cubes (a MAST, a YAST and a Theta), where each cube comprises 48 images of half-hourly MAST, YAST or Theta data.

Finally, in order to establish a common spatial framework between the MODIS and SEVIRI data, the SEVIRI ACP retrieved at the previous step were re-projected to the MODIS sinusoidal grid and supersampled to a GSD of $1\,\text{km}$.

4.2.3 Spatiotemporal Fusion of MODIS and SEVIRI ACP

To blend the SEVIRI (S) and MODIS (M) ACP (either the MAST, YAST or Theta) into a single high spatiotemporal dataset, the two-pair fusion scheme presented in Figure 4.2 is used. In particular, for a time-of-day t_κ, the proposed scheme utilises two SEVIRI-MODIS pairs—a daytime and a nighttime—and estimates the corresponding fine-resolution ACP as the average (Eq. 4.7) of the fused images derived from each pair ($M_{\text{fus},1}$ and $M_{\text{fus},2}$, respectively).

$$M_{\text{fus}}(x_i, y_j, t_\kappa) = \frac{M_{\text{fus},1}(x_i, y_j, t_\kappa) + M_{\text{fus},2}(x_i, y_j, t_\kappa)}{2} \tag{4.7}$$

The utilised SEVIRI-MODIS pairs—available at t_1 and t_2—are defined in such a way that $t_1 < t_\kappa < t_2$. Hence, the fused image from the first pair is given by Eq. 4.8a (corresponds to Eq. 4.4) and the one from the second pair by Eq. 4.8b. The latter is analogous to Eq. 4.4 and is derived by subtracting the weighted SEVIRI temporal difference from the MODIS ACP instead of adding it (as done for Eq. 4.8a).

$$M_{\text{fus},1}(x_i, y_j, t_\kappa) = M(x_i, y_j, t_1) + W_{ij1}\,[S(x_i, y_j, t_\kappa) - S(x_i, y_j, t_1)] \tag{4.8a}$$

$$M_{\text{fus},2}(x_i, y_j, t_\kappa) = M(x_i, y_j, t_2) - W_{ij2}\,[S(x_i, y_j, t_2) - S(x_i, y_j, t_\kappa)] \tag{4.8b}$$

In this work two daytime and two nighttime SEVIRI-MODIS pairs are available approximately at 10:30 and 13:30 local solar time and 01:30 and 22:30, respectively. To select which ones to use, the Rho^2 between the corresponding SEVIRI and MODIS ACP (upscaled to the SEVIRI grid) is calculated and the pairs that provided the highest values for all three ACP are the ones selected (the same pairs are used for

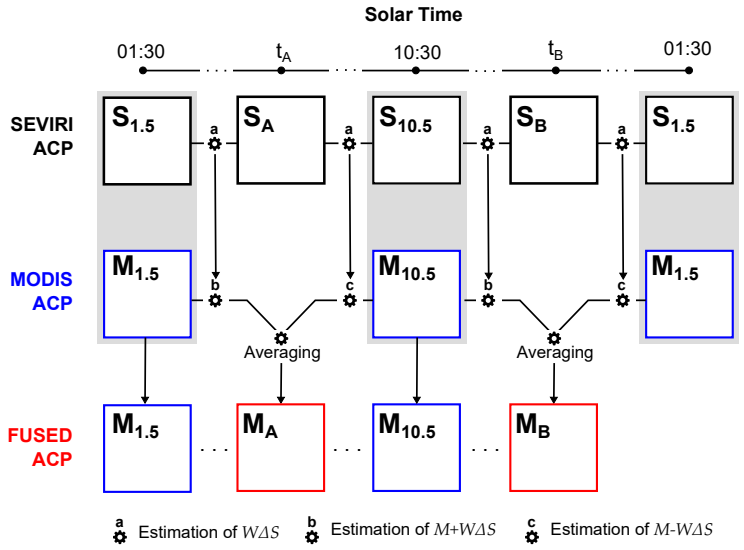

Figure 4.2: A graphical representation of the employed two-pair spatiotemporal fusion scheme. The top line corresponds to the SEVIRI ACP, the mid line to the MODIS ACP and the bottom line to the output high spatiotemporal ACP dataset.

fusing the MAST, YAST and Theta data). For this study the selected daytime pair is the 10:30 and the nighttime is the 01:30. Hence for the cases where t_κ is < 10:30, the 01:30 SEVIRI-MODIS pair is assigned as the t_1-pair and the 10:30 SEVIRI-MODIS pair as the t_2-pair. For the cases where t_κ is > 10:30 the reverse configuration is used. At 01:30 and 10:30 local solar time the MODIS ACP are included "as is" in the final dataset, as shown in Figure 4.2, while the remaining 13:30 and 22:30 MODIS ACP are used for evaluation.

The weights W_{ij1} and W_{ij2} in Eqs. 4.8a and 4.8b, respectively, are estimated separately from each SEVIRI-MODIS pair using a filter operation that is based on a moving window of size w. Within the moving window four metrics are calculated in a pixelwise manner and are then combined into a single weight (i.e. the W_{ij1} for pair 1 and the W_{ij2} for pair 2). These four metrics are the similarity degree, the euclidean distance, the scale difference and the ATC difference.

The similarity degree ($\mathrm{SD}_{ijt_{\mathrm{pair}}}$) is given by Eq. 4.9 and is the absolute difference between each window pixel and the central pixel $(x_{w/2}, y_{w/2})$. It is estimated using information only from the fine-resolution MODIS ACP at t_{pair} (either t_1 or t_2) and a small value of SD implies a high degree of similarity with the central pixel [133]. This in turn means that a large weight should be assigned to this pixel.

$$\mathrm{SD}_{ijt_{\mathrm{pair}}} = \left| M(x_i, y_j, t_{\mathrm{pair}}) - M(x_{w/2}, y_{w/2}, t_{\mathrm{pair}}) \right| \tag{4.9}$$

The euclidean distance metric (ED_{ij}) is given by Eq. 4.10 and is used so as to weight pixels closer to the central pixel more than pixels that are more distant. This is justified on the basis of Tobler's first law of geography [66], which implies that nearby pixels are more similar than distant pixels due to spatial autocorrelation [133].

$$\mathrm{ED}_{ij} = \sqrt{\left(x - x_{w/2}\right)^2 + \left(y - y_{w/2}\right)^2} \tag{4.10}$$

The third metric is the scale difference ($\mathrm{ScD}_{ijt_{\mathrm{pair}}}$) and is equal to the absolute difference of the corresponding MODIS and SEVIRI ACP at t_{pair} (either t_1 or t_2). This metric is also adopted from [133] and is used as an approximate measure of homogeneity between the MODIS and SEVIRI ACP. Like the SD, a small ScD implies a stronger similarity between the MODIS and SEVIRI ACP, which in turn means that a large weight should be assigned to this pixel.

$$\mathrm{ScD}_{ijt_{\mathrm{pair}}} = \left|M(x_i, y_j, t_{\mathrm{pair}}) - S(x_i, y_j, t_{\mathrm{pair}})\right| \tag{4.11}$$

Lastly, the final metric used is the ATC difference (AD_{ij}) between each fine-resolution window pixel and the central pixel. This metric is calculated from the MODIS ACP using Eq. 4.12, where $\widehat{T}_{\mathrm{s}}$ is the modelled LST derived from Eq. 4.5 for a subset of DOYs given by $d = 4 + 15n$, where $n = 0, 1, ..., 24$.

$$\mathrm{AD}_{ij} = \sqrt{\frac{\sum_{n=1}^{24}\left[\widehat{T}_{\mathrm{s}}(x_i, y_j, d) - \widehat{T}_{\mathrm{s}}(x_{w/2}, y_{w/2}, d)\right]^2}{n}} \tag{4.12}$$

Each one of the above metrics is adjusted using an exponential decay function so as to enhance the contribution of the most similar pixels. The retrieved values are then rescaled to range between 0 and 1 and to sum to 1. The rescaling is done in order the four metrics to have comparable values. The aforementioned two processes are performed using Eq. 4.13, where X is one of the SD, ED, ScD and AD and A_κ is a parameter for fine-tuning the exponential decay function (after sensitivity analysis A_κ is set to 6 for SD, 0.3 for ED, 3 for ScD and 3 for AS).

$$W_X(x_i, y_j) = \frac{e^{-A_\kappa X(x_i, y_j)}}{\sum_{i=1}^{w^2} e^{-A_\kappa X(x_i, y_j)}} \tag{4.13}$$

The last step for calculating the fusion weights $W_{ijt_{\mathrm{pair}}}$ is to combine the four weights derived from Eq. 4.13 into a single weight using Eq. 4.14 (one for each pair), as done

in [132] and [133]. This equation also ensures that the sum of the weights is always equal to 1.

$$W_{ijt_{\text{pair}}} = \frac{W_{\text{SD}} W_{\text{ED}} W_{\text{ScD}} W_{\text{AD}}}{\sum_{i=1}^{w^2} W_{\text{SD}} W_{\text{ED}} W_{\text{ScD}} W_{\text{AD}}} \tag{4.14}$$

The fusion weights W_{ij1} and W_{ij2} are calculated only from the moving window pixels that are similar to the central pixel. These pixels are identified using Eqs. 4.15 and 4.16. The first equation is used so as to generate four binary mask for each MODIS ACP (available at 02:00, 11:00, 13:00 and 22:00), while the second so as to calculate their *intersection* (Eq. 4.16). This approach ensures a rigorous selection of similar pixels (the selection of high quality similar pixels is of paramount importance for the success of the fusion algorithm [132]) and also that the corresponding fused MAST, YAST and Theta data are estimated from the same SEVIRI pixels.

$$\text{Mask}_{ijt_{\text{pair}}}^{\text{ACP}} = \begin{cases} 1 & \text{if } \text{SD}_{ijt_{\text{pair}}} \leq m\sigma_{\text{SD}} \\ 0 & \text{if } \text{SD}_{ijt_{\text{pair}}} > m\sigma_{\text{SD}} \end{cases} \tag{4.15}$$

$$\text{Mask}_{ij} = \left(\bigcap_{t_{\text{pair}}=1}^{4} \text{Mask}_{ijt_{\text{pair}}}^{\text{MAST}} \right) \cap \left(\bigcap_{t_{\text{pair}}=1}^{4} \text{Mask}_{ijt_{\text{pair}}}^{\text{YAST}} \right) \cap \left(\bigcap_{t_{\text{pair}}=1}^{4} \text{Mask}_{ijt_{\text{pair}}}^{\text{Theta}} \right) \tag{4.16}$$

In Eq. 4.15 σ_{SD} is the standard deviation of the SD (Eq. 4.9) for all the pixels inside the moving window and $m \in (0, 2]$ is a scale factor for controlling how strict the selection process should be.

The value of m and the size of the moving window w should be jointly determined because they have a major impact on the processing time and the fusion accuracy (e.g. if m and w are too small the algorithm performs faster but it may not be able to find similar pixels; in contrast if they are too large the algorithm performs slower and it can use low-quality pixels). To identify the optimal m and w values, a sample of regularly placed pixels (every $15\,\text{km}$) that cover the study area is extracted from the data and the aforementioned two-pair fusion algorithm is applied to each one of them separately. In detail the fusion algorithm is executed iteratively for various combinations of $w = 2r + 1$ and m, where $r = 2, 4, ..., 28$ and $m = 0.25, 0.5, ..., 2$. The output ACP are then compared with the corresponding MODIS reference MAST, YAST, Theta and for each one the Rho^2 is calculated. The r and m values that are finally selected are the ones that are closer to the origin and give a Rho^2 (rounded to the second decimal) that it does not increase by more than

1% in the next iterations (the same r and m values are used for all three ACP, as shown in Figure 4.3 for MODIS tile h18v04).

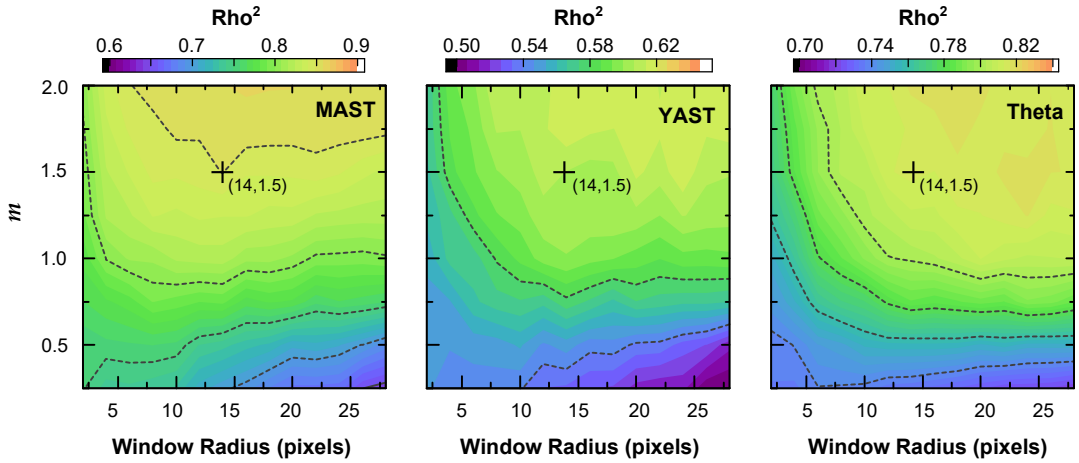

Figure 4.3: The results of the sensitivity analysis regarding the selection of parameter m and the window radius r for MAST, YAST and Theta for MODIS tile h18v04.

4.2.4 Biogeographic Analysis of the SEVIRI ACP

To further analyse the SEVIRI ACP it is hypothesised that they form a three dimensional (3D) MAST-YAST-Theta *feature space* where pixels with similar characteristics in terms of climate, geography, and land cover populate distinct subspaces. To investigate this hypothesis the following experiment is performed. Using a systematic random sampling so as to reduce the impact of spatial autocorrelation, a sample of MAST, YAST and Theta triads corresponding to various times-of-day is extracted. To obtain this sample, a regular point grid is used that extends over mainland Europe and has a cell size of $0.5^\circ \times 0.5^\circ$ (Figure 4.4). Then using the European Environmental Agency's Biogeographic Regions of Europe dataset (version 2016.1), each grid point is assigned to a biogeographic region. Europe is divided in eleven biogeographic regions, namely: alpine, anatolian, arctic, atlantic, black sea, boreal, continental, macaronesian, mediterranean, pannonian and stepic that exhibit distinct characteristics in respect to climate, physical geography, geology, vegetation and land cover. This analysis focuses only on the atlantic, continental, mediterranean and pannonian regions (Figure 4.4), which together cover more than 85% of the study area (10°W, 32°N to 30°E, 50°N). For each biogeographic region a sample of 1500 MAST, YAST and Theta triads corresponding to various times-of-day, is randomly extracted and mapped in a 3D MAST-YAST-Theta feature space. To assess if the four samples are

from the same population (and thus the aforementioned hypothesis should be rejected) or from different populations, a Kruskal-Wallis non-parametric test with a 1% significance level is used. The normality of each MAST, YAST, and Theta sample is also tested using a one-sample Kolmogorov-Smirnov test and an Anderson-Darling test with a 5% significance level.

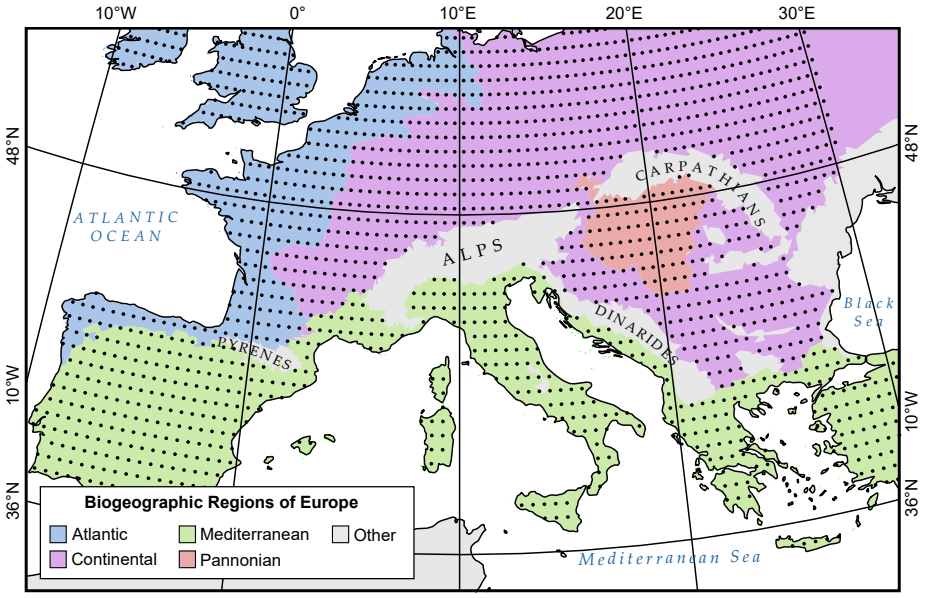

Figure 4.4: The atlantic, continental, mediterranean and pannonian biogeographic regions of Europe and the corresponding sampling positions.

4.3 Results

4.3.1 The SEVIRI ACP

The derived SEVIRI MAST, YAST and Theta ACP are presented in Figures 4.5, 4.6 and 4.7, respectively. Daytime and nighttime MAST exhibit a clear latitudinal gradient from South to North with a strong impact of topography, as it can be seen over the Alps and the Carpathian Mountains. At solar noon ($t_{\text{solar}} = 12{:}00$) Europe's MAST ranges from 270 K to 315 K (mean $\pm\,\sigma$ is 293 ± 6 K), with the highest values to correspond to the Iberian Peninsula and the lowest to the Alps. At 05:00 local solar time, which is close to the LST diurnal low, MAST ranges from 258 K to 295 K (mean $\pm\,\sigma$ is 277 ± 4 K) and follows a similar spatial distribution, where the southern areas are hotter than the northern. The difference between the MAST image for $t_{\text{solar}} = 12{:}00$ and the one for $t_{\text{solar}} = 05{:}00$ reveals that the diurnal amplitude of MAST decreases as we move north but it is also strongly affected by elevation and land

cover. For instance, Paris (France) and London (United Kingdom) have a considerably higher MAST diurnal amplitude compared to their surrounding less urbanized areas. Overall, the MAST spatial patterns are more complex during daytime than in nighttime and also in southern Europe than in northern. This is because southern Europe is more arid than the northern and the higher proportion of bare soil and sparse vegetation areas result to a more heterogeneous LST spatial distribution.

In contrast to MAST, YAST exhibits a longitudinal gradient with enhanced differences between the Atlantic coast and inland Europe. Figure 4.6 clearly shows that the YAST gradient is strongest at the northeastern part of the study area and that during the day it expands to the west until it reaches its highest peak at approximately 16:00 local solar time. It then retracts again to the northeast as it can be seen in Figure 4.6. Even though the Iberian Peninsula is at the westernmost part of Europe it is also a strong YAST hotspot, much stronger than its neighbouring France. This is most probably due to its land cover and climate. The highest YAST values are observed between 08:00 and 17:00 local solar time. For inland Europe, YAST exhibits a local maximum at approximately 09:00 (mean $\pm$ σ is 14 ± 3 K) and a global maximum at approximately 16:00 (16 ± 3 K). In coastal areas the YAST diurnal curve exhibits a different shape than inland areas and has only one maximum close to solar noon ($t_{\text{solar}} = 12{:}00$). During nighttime YAST is considerably lower than during daytime. In particular the mean $\pm$ σ difference between the 16:00 and 03:30 YAST is 11 ± 2 K. Furthermore, the YAST spatial patterns are much smoother in nighttime than in daytime as it can be clearly seen over Greece, Spain and at the northeastern part of the study area. Similar to MAST, topography also affects YAST but the corresponding spatial patterns are not as pronounced as they are for MAST.

Theta, which is the third ACP and a measure of the surface's heat uptake latency, is presented in Figure 4.7. One of the most interesting findings of this work is that Theta varies over the day and that it is greatest (in absolute values) during nighttime. In particular, the mean $\pm$ σ Theta for the entire study area is -35 ± 5 days at 02:30 local solar time, -24 ± 4 days at 07:30, -25 ± 8 days at 12:30, -22 ± 5 days at 17:30, and -32 ± 5 days at 22:30. To that end, Figure 4.7 clearly shows that the diurnal variation of Theta is not the same over Europe but it exhibits pronounced spatial patterns (both in daytime and nighttime) that are related to land cover, distance from water bodies, and topography. Overall, the magnitude of Theta (both in daytime and nighttime) is higher in the Mediterranean Europe than in the Central

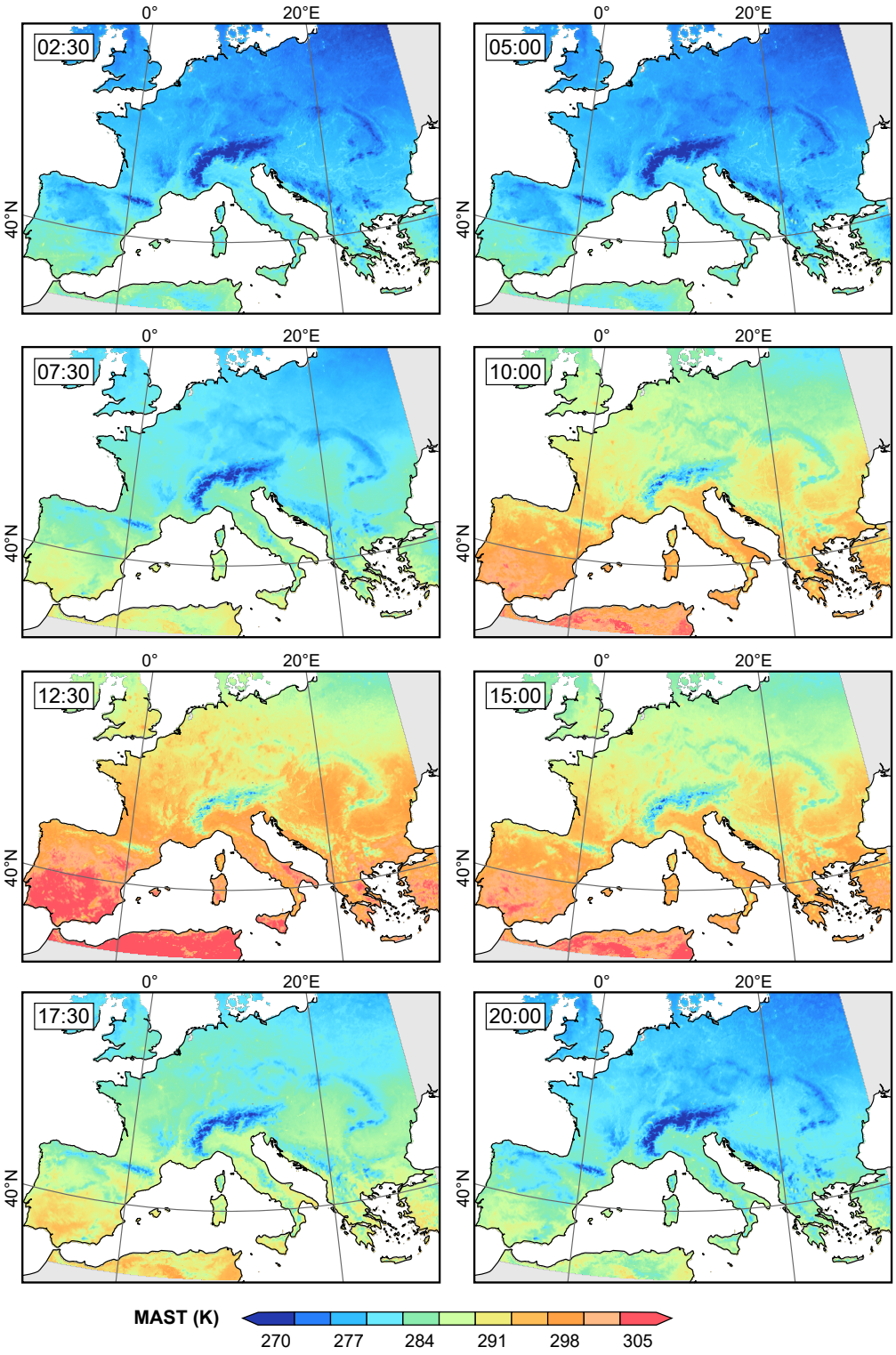

Figure 4.5: The 2009-2013 SEVIRI MAST parameter for mainland Europe for 02:30, 05:00, 07:30, 10:00, 12:30, 15:00, 17:30 and 20:00 local solar time.

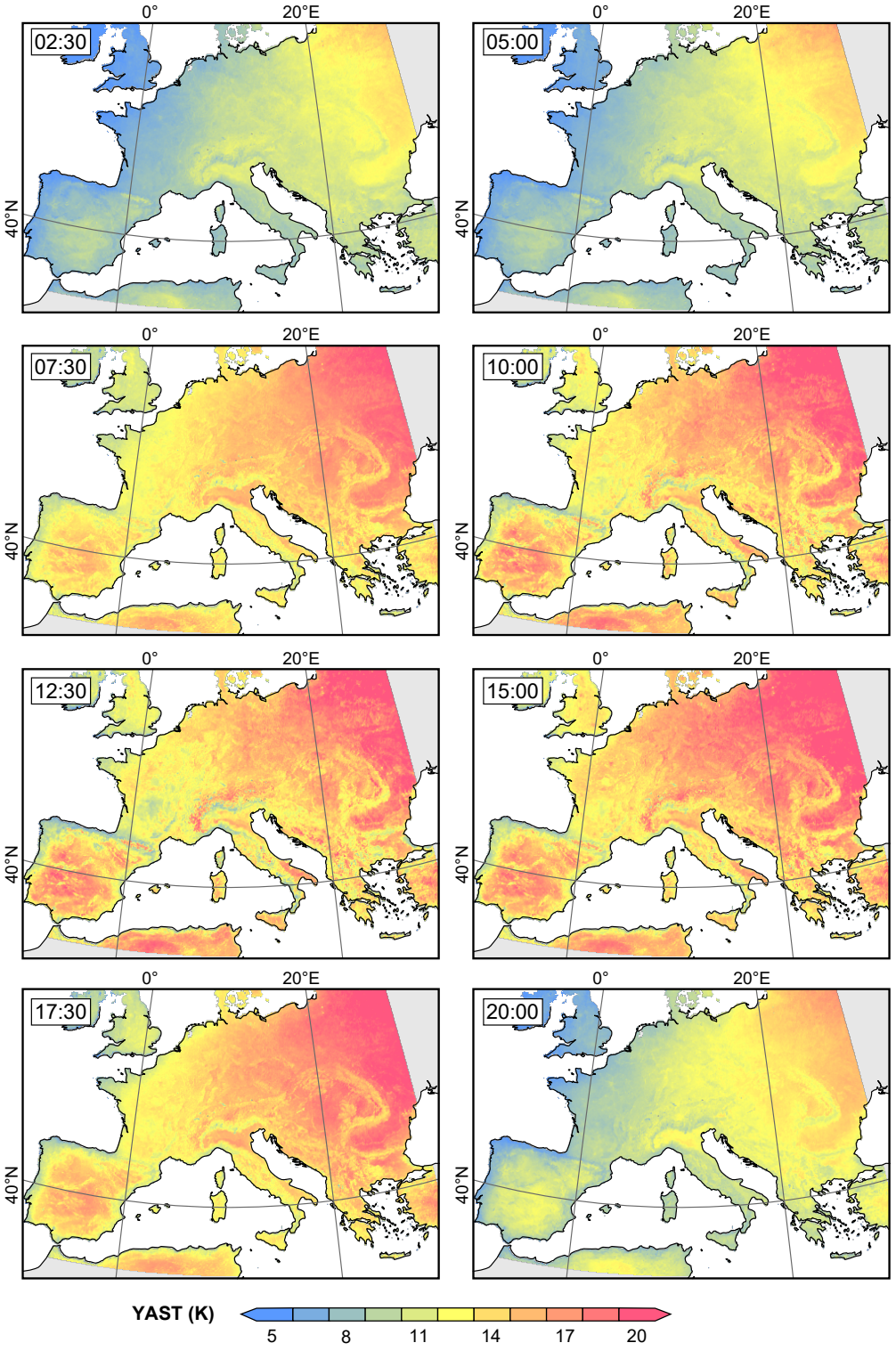

Figure 4.6: The 2009-2013 SEVIRI YAST parameter for mainland Europe for 02:30, 05:00, 07:30, 10:00, 12:30, 15:00, 17:30 and 20:00 local solar time.

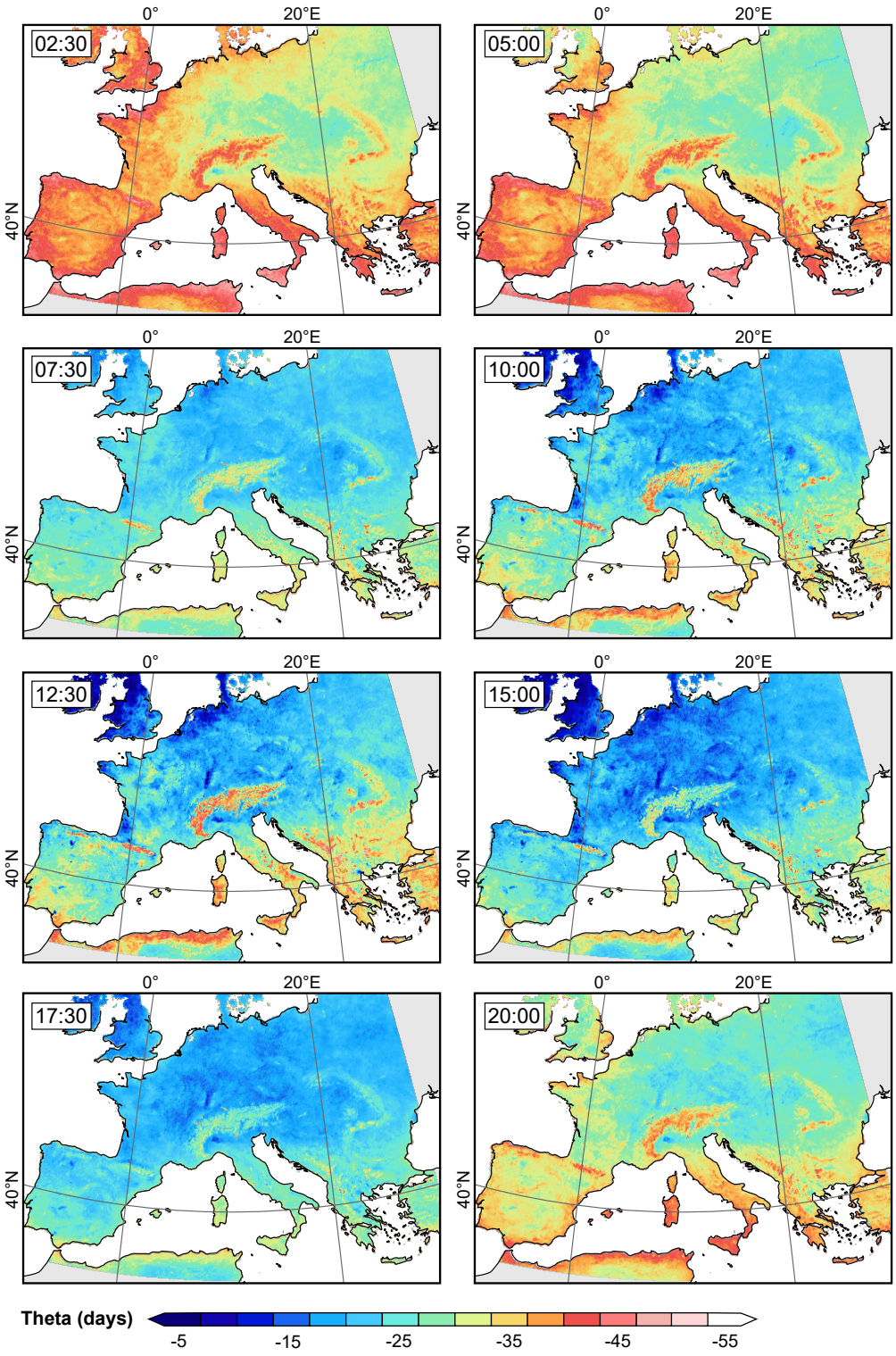

Figure 4.7: The 2009-2013 SEVIRI Theta parameter for mainland Europe for 02:30, 05:00, 07:30, 10:00, 12:30, 15:00, 17:30 and 20:00 local solar time.

and Eastern Europe, which is probably due to land cover and proximity to the sea (water has a high heat capacity). To that end, the spatial variability of Theta is also more heterogeneous over the Mediterranean region, where several clusters of high and low Theta values can populate an area of limited extend as it can be seen over the Balkans in Figure 4.7 (at 10:00 local solar time). In Central and Eastern Europe the spatial distribution of Theta is considerably more uniform and the daytime and nighttime Theta spatial clusters cover much larger areas. Another interesting observation is that Theta exhibits the most uniform spatial distribution close to sunrise and sunset as it can be seen from Figure 4.7 at 07:30 and 17:30 local solar time. Similar to MAST and YAST, the influence of topography is also evident in Theta. In detail, Europe's mountains exhibit large absolute Theta values, which imply that the LST of mountainous regions peaks later in the year in respect to the rest of Europe. This observation agrees well with the fact that the peak temperature in alpine regions is delayed due to the persistence of coldness and the high albedo of snow cover.

Together these three datasets can be used to reconstruct the full annual and diurnal LST climatology of each SEVIRI pixel over mainland Europe. An example for a randomly selected pixel is presented in Figure 4.8.

4.3.2 ACP Feature Space

To assess the information content of the half-hourly SEVIRI ACP data, their differences among the four primary biogeographic regions of mainland Europe are studied (Figure 4.4). In particular it is hypothesised that the half-hourly ACP data form a MAST-YAST-Theta feature space where the atlantic, continental, mediteranean and pannonian biogeographic regions populate distinct subspace. To that end Figure 4.9 shows that the MAST-YAST-Theta data form a unified cluster where there is a clear distinction between the atlantic (blue), continental (purple) and Mediterranean (green) subspaces, while the Pannonian region cluster (red) is partially nested inside the continental cluster. The position of each cluster is in accordance with the observations made above using the Figures 4.5, 4.6 and 4.7. In particular, the mediterranean biogeographic region corresponds to a subspace of high MAST and Theta values but moderate YAST, while the alpine to a subspace of low MAST, moderate YAST and high Theta (in absolute values). The atlantic region corresponds to a subspace of low MAST, YAST and Theta and the continental region to a subspace of low MAST, moderate Theta but high YAST. For every case the employed Kruskal-Wallis

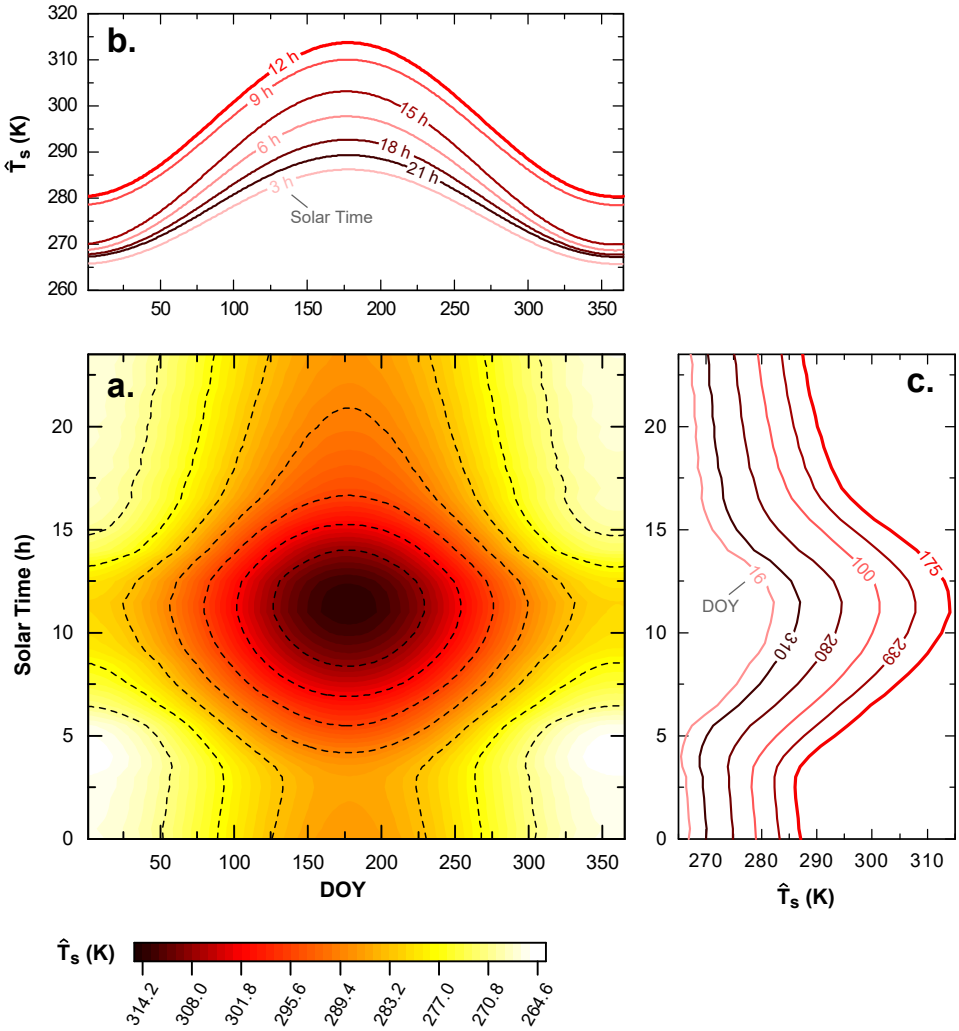

Figure 4.8: Combined climatological annual and diurnal LST cycle for an example SEVIRI pixel over Europe based on the proposed methodology.

test was against the null hypothesis at the 0.01 significance level, which suggests that the four samples are not from the same ACP population.

4.3.3 Similarity of SEVIRI-MODIS ACP and Accuracy of Fused ACP

The SEVIRI and MODIS ACP used in this work are highly compatible, as evident in Figure 4.10 and Table 4.1. For MAST, Rho is close to 0.95 for all cases but the bias, MAE and RMSE statistics are greater for the daytime data than the nighttime data. In particular the daytime SEVIRI MAST is warmer by about 2.0 K in respect to the corresponding MODIS MAST (a similar observation is made in [97]), while the nighttime MAST is colder by approximately 0.6 K. The RMSE and MAE between the SEVIRI and MODIS daytime MAST are close to 2.3 K and 2.0 K, respectively, while the corresponding nighttime values are 1.2 K and 0.9 K (Table 4.1). For YAST

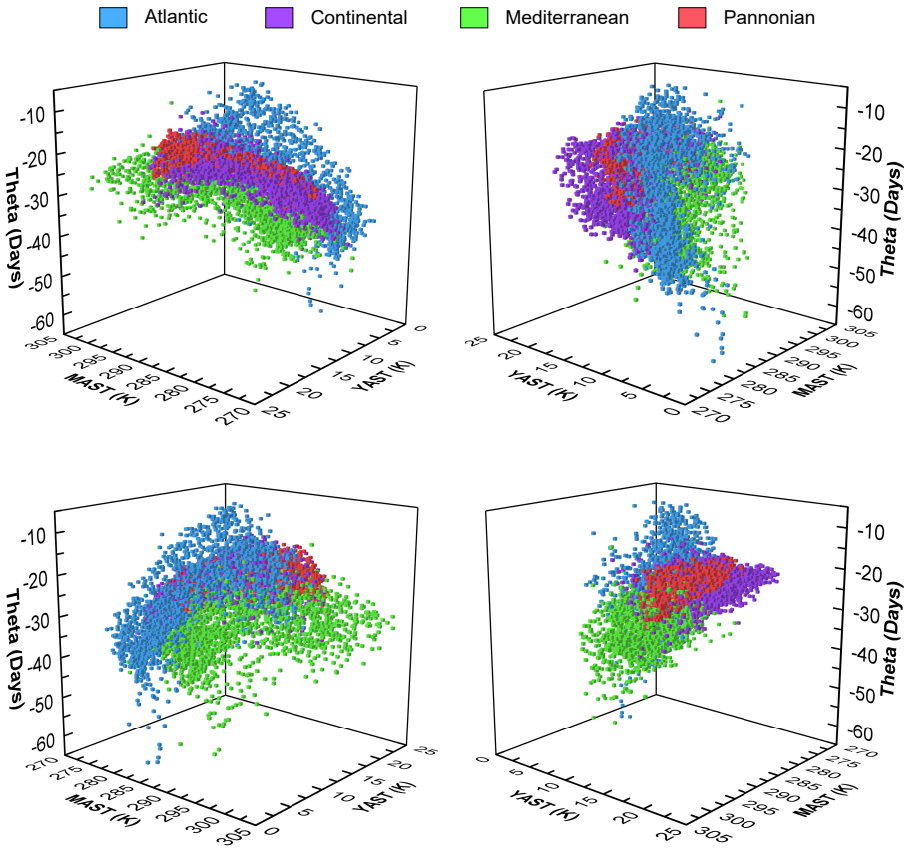

Figure 4.9: The MAST-YAST-Theta 3D feature space for the Atlantic (blue), Continental (purple), Mediterranean (green) and Pannonian (red) biogeographic regions.

and Theta, the SEVIRI-MODIS ACP differences are minor too. In particular, the YAST nighttime Rho is approximately 0.94, but it drops to 0.84 for the Terra daytime data and 0.79 for the Aqua daytime. The corresponding bias, RMSE and MAE are $0.0\,\mathrm{K}$, $0.5\,\mathrm{K}$ and $0.4\,\mathrm{K}$, respectively, for the nighttime YAST data and $0.4\,\mathrm{K}$, $1.1\,\mathrm{K}$ and $0.8\,\mathrm{K}$ for the daytime data. Theta exhibits also a similar behaviour, where the statistics of the nighttime data are superior than those from the daytime data. In particular the nighttime Rho is above 0.9, while the daytime Rho is around 0.87 (see also Figure 4.10). The Terra and Aqua daytime MAE and RMSE are close to 3.3 and 2.4 days, respectively, while the corresponding nighttime values are 1.4 and 1.9 days, respectively. Overall the aforementioned results suggest that the SEVIRI and MODIS ACP are very similar and thus they can be effectively fused into a single dataset.

The performance of the proposed fusion scheme is tested for MODIS tile h18v04 over south-central Europe. This tile is an ideal testbed for evaluating the fusion algorithm, since it covers an area with several land cover classes and terrain types. To that end Figures 4.11 and 4.12 present the $1\,\mathrm{km}$ fused ACP for 13:00 and 22:00

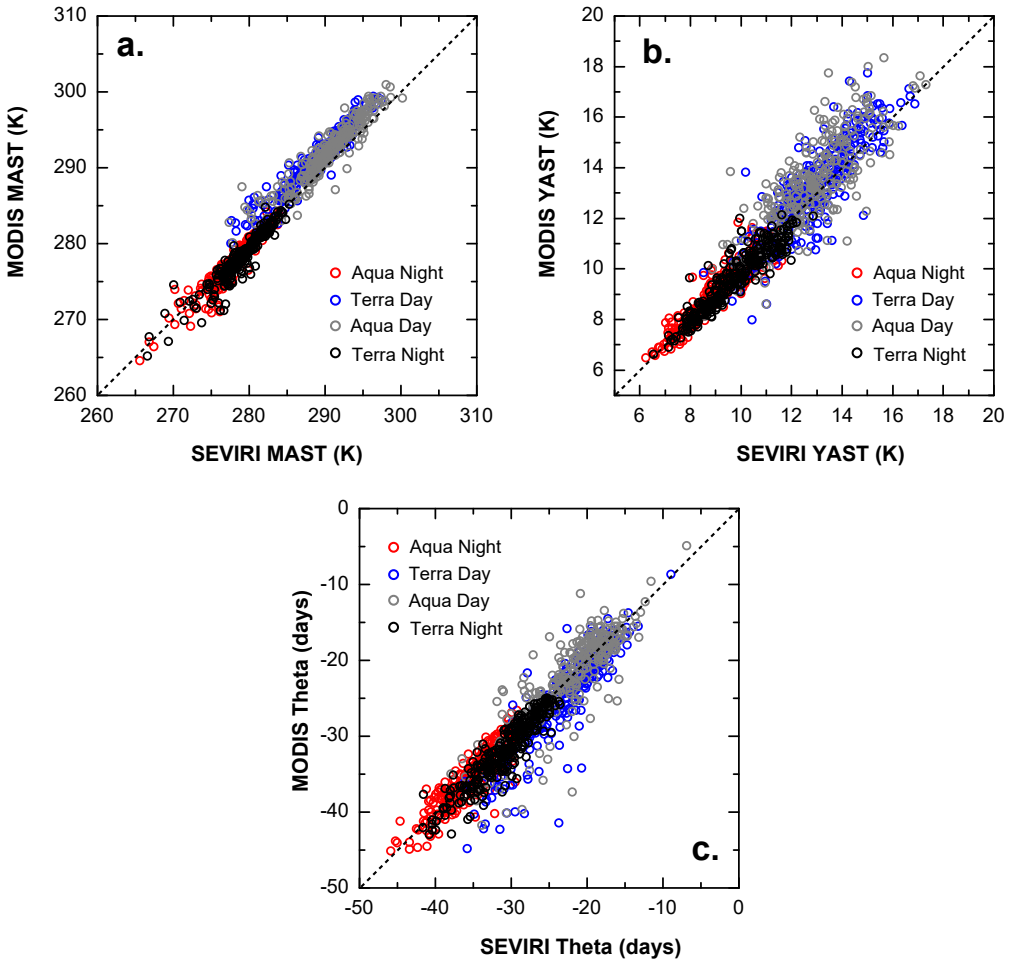

Figure 4.10: The relationship between the SEVIRI and MODIS ACP for tile h18v04. For this comparison the MODIS ACP were resampled to the SEVIRI coarse-resolution grid.

local solar time[2], respectively, alongside the corresponding reference MODIS data. Overall the spatial patterns of the fused daytime and nighttime MAST, YAST and Theta data are highly similar to the reference ACP. The fusion algorithm was able to adequately reproduce both major and minor features in the ACP data, such as the SUHIs of the various cities and the major river basins of Po in Italy and Rhine in Germany (especially pronounced in the corresponding YAST and Theta maps). Linear features, such as mountain ridges and large rivers, were also reproduced adequately by the fusion algorithm, as it can be seen over the Alps in Figures 4.11 and 4.12. In general the algorithm performs robustly over flat areas but it can produce artefacts over the coastline and also in areas with pronounced topography, such as the the Alps and the Pyrenees.

[2]For tile h18v04 the mean solar time of all the MODIS LST observations used for retrieving the ACP are approximately 02:00 for Aqua nighttime, 11:00 for Terra daytime, 13:00 for Aqua daytime and 22:00 for Terra nighttime.

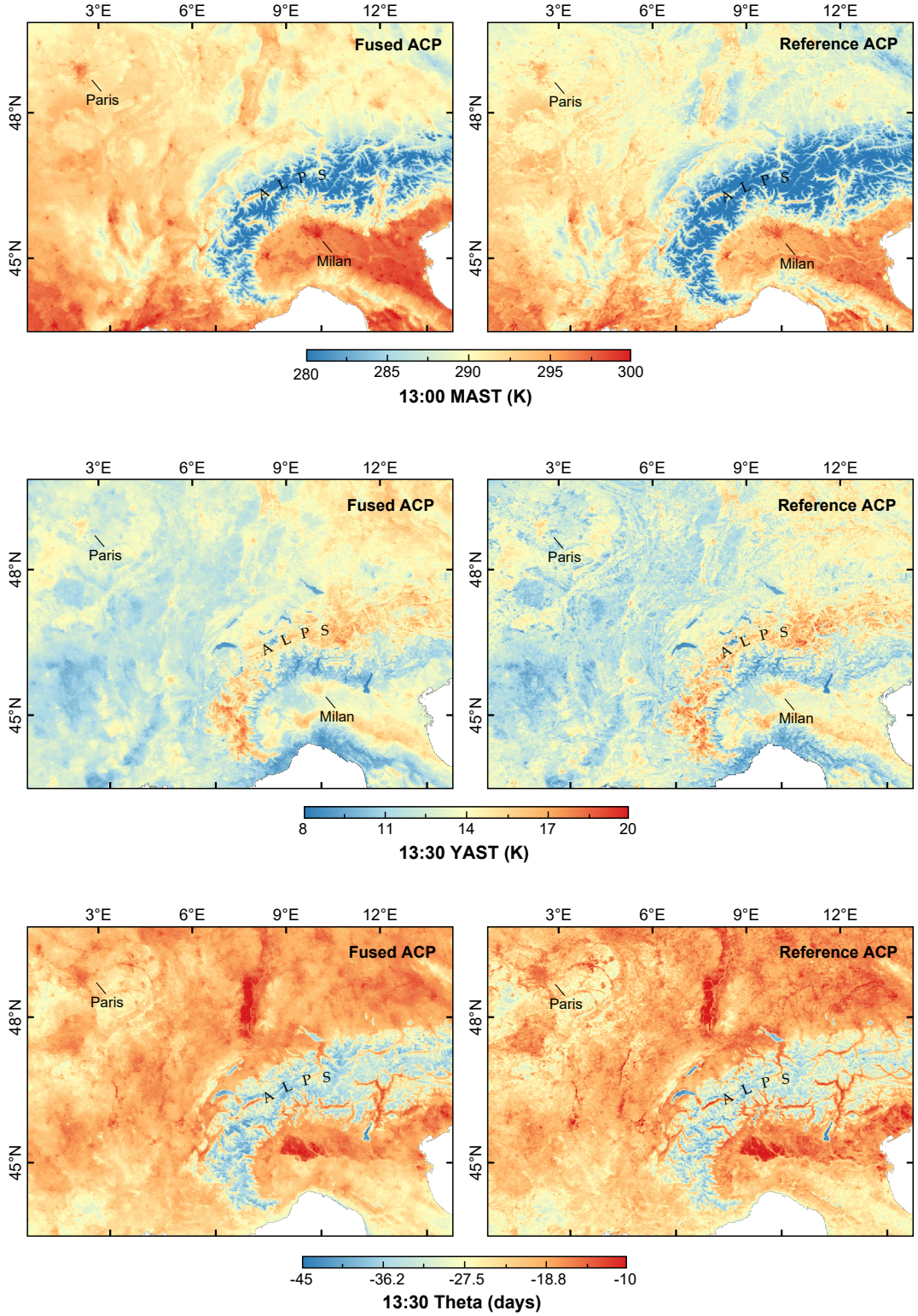

Figure 4.11: The 13:00 fused ACP over south-central Europe.

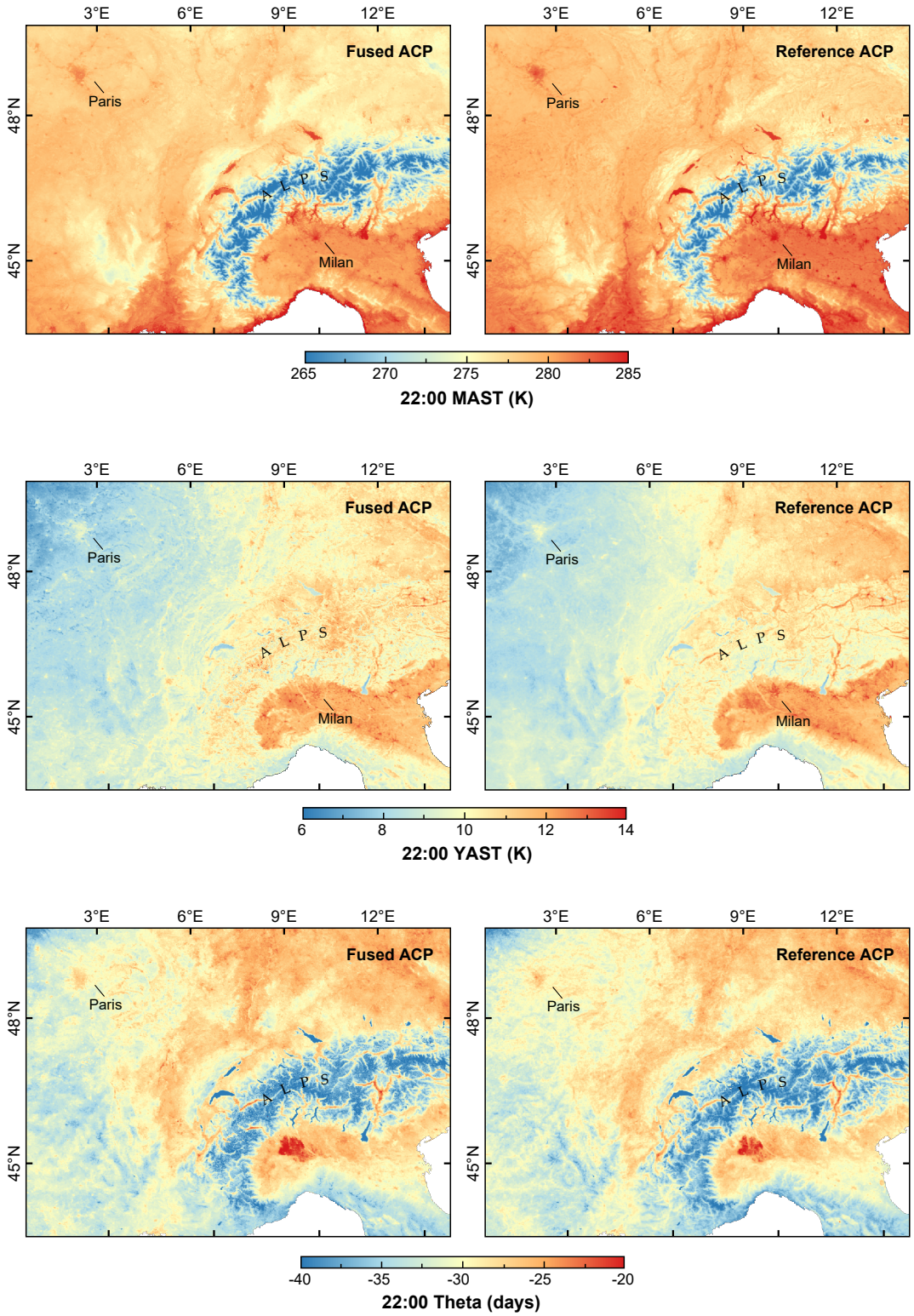

Figure 4.12: The 22:00 fused ACP over south-central Europe.

Table 4.1: Summary statistics quantifying the difference of the 2009-2013 SEVIRI and MODIS v.6 ACP for MODIS tile h18v04. The MODIS ACP were resampled to the SEVIRI coarse-resolution grid.

ACP	Data	Bias	σ	RMSE	MAE	Rho
MAST	Aqua Night	$-0.4\,\mathrm{K}$	$1.0\,\mathrm{K}$	$1.1\,\mathrm{K}$	$0.7\,\mathrm{K}$	0.96
	Terra Day	$2.1\,\mathrm{K}$	$1.3\,\mathrm{K}$	$2.5\,\mathrm{K}$	$2.1\,\mathrm{K}$	0.95
	Aqua Day	$1.6\,\mathrm{K}$	$1.5\,\mathrm{K}$	$2.2\,\mathrm{K}$	$1.8\,\mathrm{K}$	0.94
	Terra Night	$-0.8\,\mathrm{K}$	$1.1\,\mathrm{K}$	$1.3\,\mathrm{K}$	$1.0\,\mathrm{K}$	0.95
YAST	Aqua Night	$0.0\,\mathrm{K}$	$0.5\,\mathrm{K}$	$0.4\,\mathrm{K}$	$0.3\,\mathrm{K}$	0.95
	Terra Day	$0.2\,\mathrm{K}$	$0.9\,\mathrm{K}$	$1.0\,\mathrm{K}$	$0.7\,\mathrm{K}$	0.84
	Aqua Day	$0.5\,\mathrm{K}$	$1.1\,\mathrm{K}$	$1.2\,\mathrm{K}$	$0.9\,\mathrm{K}$	0.78
	Terra Night	$-0.2\,\mathrm{K}$	$0.5\,\mathrm{K}$	$0.5\,\mathrm{K}$	$0.4\,\mathrm{K}$	0.93
Theta	Aqua Night	$0.0\,\mathrm{d}$	$1.6\,\mathrm{d}$	$1.6\,\mathrm{d}$	$1.2\,\mathrm{d}$	0.92
	Terra Day	$-1.8\,\mathrm{d}$	$2.9\,\mathrm{d}$	$3.5\,\mathrm{d}$	$2.4\,\mathrm{d}$	0.88
	Aqua Day	$0.1\,\mathrm{d}$	$3.0\,\mathrm{d}$	$3.0\,\mathrm{d}$	$2.1\,\mathrm{d}$	0.86
	Terra Night	$-1.2\,\mathrm{d}$	$1.7\,\mathrm{d}$	$2.1\,\mathrm{d}$	$1.6\,\mathrm{d}$	0.91

To assess the accuracy of the fused ACP, several descriptive statistical measures are used, as shown in Table 4.2. To that end, for MAST the MAE and RMSE are close to $1.1\,\mathrm{K}$ and $1.5\,\mathrm{K}$, respectively, while Rho is 0.97. In respect to the reference MODIS data, the fused daytime MAST is warmer by $1.7\,\mathrm{K}$, while the nighttime MAST is colder by $-1.1\,\mathrm{K}$. For YAST the fusion algorithm performed better for the nighttime data than for the daytime data. In particular, the 13:00 RMSE is $0.7\,\mathrm{K}$, while the 22:00 is $0.5\,\mathrm{K}$. The corresponding Rho values are 0.88 and 0.93, respectively, while the MAE and bias are close to $0.4\,\mathrm{K}$ and $0\,\mathrm{K}$, respectively, for both cases. For Theta the bias, is close to 0, the MAE is close to 1.3 days and the RMSE to 1.7 days. The Rho for the 13:00 data is 0.92, while for the 22:00 is 0.94. The good performance of the fusion algorithm is also evident in the scatterplots of Figure 4.13, where the corresponding point clouds are distributed well over the line of equality ($y = x$). The increased MAST bias is caused by SEVIRI and MODIS differences, such as different VZA and LST retrieval methods, and needs further investigation. In particular the mean SEVIRI MAST range between 13:00 and 11:00 and 13:00 and 02:00 are $1.8\,\mathrm{K}$ and $-15.8\,\mathrm{K}$, respectively, while the corresponding MAST values are $1.4\,\mathrm{K}$ and $-12.8\,\mathrm{K}$, which implies that the key assumption that the system biases are constant has to be reexamined.

Table 4.2: Summary statistics quantifying the difference of the 2009-2013 fused SEVIRI and MODIS v.6 ACP for MODIS tile h18v04.

ACP	t_{solar}	Bias	σ	MAE	RMSE	Rho
MAST	13:00	1.7 K	1.0 K	1.0 K	1.7 K	0.97
	22:00	−1.1 K	0.9 K	1.2 K	1.4 K	0.97
YAST	13:00	0.0 K	0.8 K	0.6 K	0.7 K	0.88
	22:00	−0.1 K	0.4 K	0.3 K	0.5 K	0.93
Theta	13:00	−0.4 d	2.1 d	1.6 d	2.1 d	0.92
	22:00	0.1 d	1.3 d	1.0 d	1.3 d	0.94

4.4 Discussion

The MAST, YAST and Theta maps of this work present the diurnal and annual dynamics of Europe's LST with increased detail. This information can improve the current understanding of the thermal behavior of the Earth's surface and also land surface models, where the assimilation of LST information has been shown to improve their performance (e.g. [14]). To that end, Yang and Slingo [123] argue, that prior knowledge of the DTC amplitude and time lag can help identify and correct model deficiencies, improve model parameterization and also the representation of the interactions between the surface, the boundary layer, and the free atmosphere. An advantage of using the ACP methodology to map Europe's LST dynamics is that it provides a robust way to handle the high spatiotemporal variability of satellite LST, which if not properly addressed can lead to erroneous conclusions.

Overall, the MAST and YAST maps of this work are consistent with the established understanding of Europe's temperature gradients, while Theta provides a more complete picture of the LST peak times. In addition, the SEVIRI ACP data of this work agrees well with the MODIS ACP presented in [59]. An improvement in respect to the MODIS ACP is that the SEVIRI ACP present the MAST, YAST and Theta temporal dynamics in full (the MODIS ACP are available only four times within a day, two at noon and two at night). It has to be noted though, that Theta is the ACP most difficult to interpret and for this reason further study is necessary. Moreover, the employed two-pair spatiotemporal fusion method proved to be a robust approach for increasing the spatial resolution of the ACP data, since it achieved high Rho and low RMSE and MAE values. Future works should test new metrics as weights, propose post-processing schemes for the removal of artefacts and investigate ways to compensate system biases.

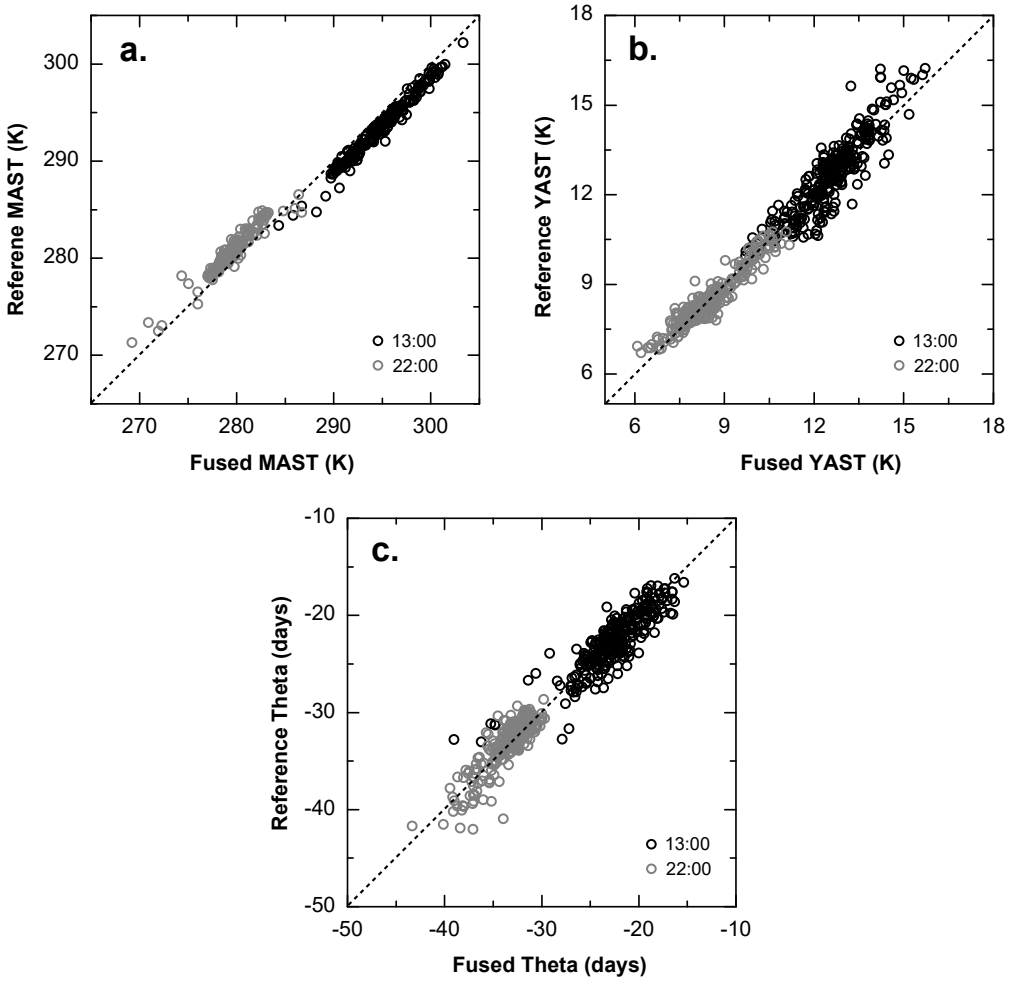

Figure 4.13: The similarity between the fused and reference ACP for tile h18v04.

This work also suggests that the ACP data form a three dimensional feature space where areas with similar characteristics in terms of climate, geography, and land cover populate distinct subspaces. To that end, evidence are provided about the shape of this feature space and the characteristics of the atlantic, continental and mediterranean subspaces. The clear distinction between the three biogeographic subspaces is in line with the findings of Bechtel in [138], where it is shown that different Köppen climates are related to the ACP. The above further suggest that the ACP can be used for effective climate classification and thermal landscape mapping, as initially proposed in [59].

4.5 Concluding Remarks

This chapter proposed a method for reducing the information content of LST time series into a set of meaningful parameters and presents a series of maps that provide a

complete picture of Europe's LST spatiotemporal dynamics and reveal how Europe's primary biogeographic regions differ in that respect. To improve the spatial resolution of the data a two-pair fusion algorithm has been proposed which performed robustly. The derived ACP data can be used to reconstruct the full annual and diurnal LST climatology for each SEVIRI pixel over mainland Europe with increased spatial resolution. Overall, the results suggest that the derived data can provide an observation-based, spatially-consistent background for studying and characterising (at continental scale) the surface's thermal behaviour and also a dataset to support climate classification at finer spatial resolution.

Chapter 5

Conclusions and Future Directions

5.1 Main Findings

This thesis provides new insights into the statistical downscaling of geostationary LST time series, which can address the lack of high spatiotemporal LST datasets (Chapters 2 and 3); and advances the methods that analyse and summarise such voluminous datasets using LST cycle models (Chapter 4). The aforementioned three chapters address the research objectives set in §1.3, as discussed below:

Research Objective 1: to identify LST disaggregation kernels that perform consistently irrespectively of time-of-day and thus are suitable for downscaling diurnal LST acquired by geostationary satellite instruments.

The LST predictors are the most important element of every downscaling scheme, since they determine the validity of the scale invariance and connectivity assumptions. This thesis tested multitemporal LST annual climatology data as LST predictors and assessed if the employed MAST, YAST and Theta ACP could robustly downscale daytime and nighttime LST. The underlying rationale is that diurnal ACP provide information about the LST spatial distribution at different times-of-day and thus their explanatory power does not vary with time, as is the case for static LST predictors like NDVI and altitude.

To test this hypothesis a controlled experiment was performed and the downscaling performance of two complementary sets of LST predictors—the first comprising NDVI, elevation, emissivity and albedo data and the second all of the above plus the ACP—was assessed. The comparison of the derived DLST suggests that the inclusion of the multitemporal ACP as LST predictors improves the DLST accuracy (both for daytime and nighttime) and also the DLST spatial patterns in terms of shape, size

and location. Furthermore, the results of this work show that the ACP can increase the proportion of the variance that is explained by the derived LST data-predictor models and that the use of multitemporal ACP as predictors ensures that the LST interrelationships are replicated more accurately. This is particularly evident in the assessment of the DLST diurnal range, where the ACP improved the distribution of the daytime-minus-nighttime DLST values and the shape of the corresponding spatial patterns.

Furthermore, the land cover analysis of Chapter 2 shows that the ACP can improve the calculation of the DLST diurnal range in urban, rural and vegetated regions and make the spatial distribution of the RMSE more homogeneous. This is because the ACP, being derived from LST data, incorporate the location-specific variability and also how this variability changes with time. This in turn implies that they can perform consistently over various land cover types, landscapes and climatic conditions, which can facilitate the development of LST downscaling schemes that are not limited to regions with specific landscape and climatic characteristics.

The research findings of Chapter 2 (also published in [62]) contribute to the ongoing debate about what ancillary data should be used as LST predictors and how they should be configured into sets, considering that their performance depends on various interdependent factors. In addition, this work provides new insights into the design of downscaling schemes that are not limited to specific landscapes, times-of-day and land covers.

Research Objective 2: to investigate if and how well a DLST time series can reproduce the spatiotemporal features of the original coarse-scale temporally dense LST.

In Chapter 3 a quarter-hourly, $4\,\mathrm{km} \times 5\,\mathrm{km}$, three-month long LST time series was statistically downscaled to a GSD of $1\,\mathrm{km} \times 1\,\mathrm{km}$ and (i) the accuracy, reliability, and consistency of the downscaling method; (ii) the shape, size, and location of the DLST spatial patterns; and (iii) the capability of the DLST time series to emulate the diurnal and seasonal characteristics of the original LST data were assessed. To investigate these issues, ten assessment tests were used that either compared the DLST data with corresponding reference data, or exploited the high temporal resolution of the SEVIRI data so as to assess the DLST spatiotemporal interrelationships.

The image-per-image comparisons with the reference MODIS data revealed that LST downscaling can indeed perform consistently and reliably and systematically

provide DLST data with similar RMSE and Rho values. Nevertheless, increased errors should be expected during daytime hours and over areas with pronounced morphology, such as urban areas and mountainous regions. This is due to thermal anisotropy effects and because the LST patterns are more complex and heterogeneous in daytime than in nighttime, which further implies that more powerful LST predictors are required for these times-of-day. Furthermore, the assessment of the DLST spatial patterns revealed that LST downscaling algorithms can produce diurnal DLST data, where the DLST hotspots and coldspots appear/disappear and expand/contract in a smooth manner during the diurnal cycle. To that end the comparison of the DLST patterns with the corresponding reference ones, showed that the DLST data present the major spatial features at correct locations but with less detailed shapes. Regarding this issue, the findings of Chapter 2 point out that TIR-based LST predictors can facilitate the formation of DLST hotspots/coldspots that have more accurate shapes and sizes.

To assess the spatiotemporal interrelationships of the DLST data, Chapter 3 proposed the use of autocorrelation tests. In particular a series of evaluation tests that estimate the Rho (i) between sequential images and (ii) between the first image of the time series and the rest were used. The aim of these tests is to assess the capability of the DLST data to emulate seasonal and diurnal features. The results revealed that the diurnal evolution of the clear-sky DLST was smooth and artefact-free and that the downscaling algorithm was able to produce DLST data that emulate long-term trends. Nevertheless the similarity of the DLST was higher than of the reference data, suggesting that the DLST data cannot represent subtle spatial thermal changes as pronouncedly as the measured data can. The proposed autocorrelation tests proved useful in assessing the DLST data and the information content of the derived DLST time series. It was also realised that other studies (e.g. [139]) have adopted these tests for evaluating the derived high spatiotemporal DLST data.

The work presented in Chapter 3 (and also published in [63]) is one of the first assessment studies that is concerned with the downscaling of LST time series and with the assessment of how LST downscaling can affect—in unforeseen ways—the information content of the derived datasets. The findings of this work can inform the development of improved downscaling algorithms and progress the research efforts that are underway so as to make their use operational.

Research Objective 3: to develop a method for simultaneously modelling the diurnal and annual cycle of temporally dense LST or DLST and reducing the model to a set of key cycle parameters.

Chapter 4 presents a novel methodology for modelling the diurnal and annual LST cycle with fine spatial and temporal detail. The proposed method iteratively fits the ACP sine model to geostationary multitemporal LST and then retrieves the corresponding diurnal MAST, YAST and Theta data. To increase the GSD of the derived cycle parameters the use of a two-pair spatiotemporal fusion scheme is used that blends the geostationary ACP with corresponding finer-resolution ACP retrieved from MODIS. The derived cycle parameters provide a gap-free representation of the surface's thermal characteristics and temporal dynamics and can be used for reconstructing the LST annual and diurnal climatological cycles for every $1\,\mathrm{km} \times 1\,\mathrm{km}$ land pixel.

This work is the first that extracts ACP from temporally-dense geostationary data (the corresponding results are presented in [64]). The derived MAST, YAST and Theta data share the same temporal resolution as the original half-hourly LST and provide a complete picture of how the latitude, the topography, the land cover and the distance from the sea impact the surface thermal landscape at various times-of-day. This information can help identify and correct land surface model deficiencies and also enable the study of how these cycle parameters vary through the day. A better understanding of these variations can prove useful to climate classification and also for characterising and generalising the thermal behaviour of similar land covers, e.g. urban, rural etc. To that end the results presented in Chapter 4 support this hypothesis and suggest that the derived MAST, YAST and Theta data form a feature space where areas with similar characteristics in terms of climate, geography, and land cover populate distinct subspaces.

The employed two-pair spatiotemporal fusion scheme proved to be effective and robust and was able to reproduce both major and minor spatial features in the fine-resolution MAST, YAST and Theta data. The selection of similar pixels using information from all three ACP proved rigorous and simpler to implement than the land cover-based approaches currently in use. The employed spatiotemporal weighting scheme performed also well but further fine-tuning is required so as to compensate for the artefacts that resulted near the coastline and at regions with pronounced topography, e.g. the Alps. Further research is still required on how to compensate

the differences between the multisource ACP data that arise due to differences in the VZA, the acquisition time and the calibration between the two satellite instruments. In this work, these differences made the MAST diurnal variations to differ between SEVIRI and MODIS which caused the fused MAST data to be warmer than the corresponding MODIS data during daytime and colder during nighttime. This observation also hints that the main assumption of spatiotemporal fusion, i.e. that the difference between the two data sources are systematic, should be reassessed for the case of SEVIRI and MODIS.

Chapter 4 addresses the final research objective of this thesis and presents a methodology that can reduce a long LST/DLST time series to a set of cycle parameters that represent the surface's thermal characteristics. These parameters can then be used to simultaneously model the climatological diurnal and annual cycle of LST. This work advances the research on time series analysis and provides an effective approach for handling the pronounced spatiotemporal variability of LST data.

5.2 Contribution to Science and Impact

This thesis provides a solution to the lack of LST predictors that perform consistently and robustly over various times-of-day, land covers and landscapes and demonstrates that multitemporal LST annual climatology data offer these attributes. The use of such versatile all-around predictors makes the configuration of LST predictor sets simpler and less laborious and the corresponding downscaling schemes not limited to areas with a specific land cover type or to LST data acquired at certain times-of-day, as is the case presently. The downscaling of a three-month long diurnal LST time series confirmed that the production of high spatiotemporal datasets from geostationary LST is feasible and was a step forward in comparison to the state-of-the-art, where LST downscaling algorithms are tested only on a few carefully-selected scenes. In particular it provided a more comprehensive view of how downscaling algorithms can impact the spatiotemporal interrelationships of the LST data—and consequently the information content of the derived DLST time series—, which using individual scenes is impossible to assess. To that end this thesis showed that LST downscaling can result in autocorrelated time series and suggested new evaluation tests that are not limited by the availability of ground-truth LST data. Furthermore, this thesis also combined two established methods, namely the ACP retrieval and

the spatiotemporal fusion, and proposed a new method for simultaneously modelling the climatological diurnal and annual cycle of LST. This is a step forward compared to the state-of-the-art where the LST cycles are modelled separately. To that end, this work was the first to apply the ACP model to diurnal geostationary data and revealed in unprecedented spatial and temporal detail how mainland Europe responds to the heating of the sun and the nighttime LST decay and how Europe's biogeographic regions differ in that respect.

The findings of this thesis advance thermal remote sensing and in particular the research fields of LST disaggregation and LST cycle characterisation. They contribute to the ongoing discussion about *"What are the well-behaved kernels and how should kernels be configured into sets?"* (LST Downscaling Open Issue 1, according to the review of Zhan et al. [53]) and *"What role can auxiliary data and models other than optical images play in benefiting LST downscaling?"* (LST Downscaling Open Issue 2) and help make the use of the ACP as LST disaggregation kernels more wide (alongside [82]). Furthermore, the research findings of this work can inform practitioners to select appropriate LST predictors and design downscaling schemes that perform robustly over extensive heterogeneous areas. This thesis also advances the research efforts that aim to make LST downscaling schemes operational and for non-experts. The work on LST cycle characterisation resulted to a new way to exploit data from geostationary satellites and to a new dataset (i.e. the SEVIRI ACP) that was made available to the scientific community. To that end the proposed fused ACP overcome the limitation of the already-released MODIS ACP and can provide a complete set of ACP LST predictors that is not limited by time gaps, which is currently missing. To a large extent the findings of this thesis have already been put in good use and improved the online LST downscaling service of IAASARS/NOA. The research presented in this dissertation has informed the update of the employed LST predictor set and improved the accuracy of the spatial information of the generated DLST data. It also helped the service to expand and include new cities with considerably different climates, land covers and landscapes. The proposed diurnal ACP model has also been tested with the T_{air} product that the IAASARS/NOA service also generates (see [140]) and used for summarising the information of long T_{air} time series into climatological datasets that are of more easily manageable and require less storage space.

5.3 Open Issues and Future Directions

Even though significant improvements have been achieved in the last two datasets, many challenges related to thermal remote sensing in general and LST downscaling in particular remain. The most important are:

- *The bias of LST/DLST datasets to clear-sky conditions*. On average, 60% of the land surface is covered by clouds, which reduce or block the incoming shortwave radiation and thus influence the LST. In addition, clouds are usually associated with other weather phenomena, such as precipitation, which also affect the surface energy balance and the land surface emissivity. Because clouds block the surface-emitted TIR radiation, the retrieval of LST over cloud-covered areas in not possible (instruments measuring the thermal microwave radiation can overcome this problem). This raises a very important issue in TIR remote sensing, which is that all the available datasets correspond to clear-sky (i.e. warm) conditions and thus their analysis would always give biased results. The lack of all-weather LST also impacts LST downscaling by making the derived LST data-predictor models to apply only for clear-sky conditions. This implies that if these models are applied to pixels corresponding to cloud-covered areas the retrieved DLST values will be warmer than they are in reality. To address this issue further research efforts are required on the retrieval of all-weather LST/DLST.

- *The lack of high-quality spectral emissivity data*. Presently most emissivity data are retrieved using classification-based methods. Such approaches are well-suited for land-cover types such as dense evergreen canopies, lake surfaces, snow, and soils, which have stable emissivities that are known with high accuracy (usually within 1%). However such data are less reliable over arid and semi-arid regions and also over urban areas with pronounced morphology and heterogeneity. Because the emissivity is key for retrieving LST/DLST data that meet the $1\,\mathrm{K}$ accuracy goal, better land surface emissivity products are required. A step towards this direction is the forthcoming MOD21 LST and emissivity data product which is based on TES (see §1.2.4).

- *Thermal anisotropy*. Thermal anisotropy refers to the angular variation of TIR radiation and is stronger during daytime than nighttime. Thermal anisotropy

can make the LST of the same target to vary more than $2\,\mathrm{K}$ to $4\,\mathrm{K}$ when viewed by different direction. This can hamper the comparison of LST data retrieved from different sensors or the use of multi-source LST datasets. Further research should focus on how to compensate these effects or to propose strategies on how to properly control them.

- *Spatial scale and downscaling to finer spatial resolutions*. In general, the success of LST downscaling is determined by the spatial scale and the ability of the satellite instrument to acquire TIR data that carry the composite effect of various environmental factors in such a way that it does not prohibit the disaggregation of the LST to finer spatial resolutions. Hence, to ensure a successful downscaling it is important to understand better how the spatial scale affects the relationship between the LST and the LST predictors, what effects and environmental factors dominate each spatial scale, and if spatial scale poses any limitations on reaching the target spatial resolution. Answering these questions can inform the selection of LST predictors and and also how to bridge large scale differences, e.g. downscaling $4\,\mathrm{km}$ LST to $0.1\,\mathrm{km}$.

- *The inadequate representation of urban 3D features*. The morphology of the urban surface is characterised by a complex three-dimensional structure consisting of buildings, open spaces, and street canyons. This canyon-block structure is unique for each city and has a pronounced influence on the urban thermal environment. Unfortunately, many of these vertical surfaces remain unseen by the satellite during the data acquisition process. These facets comprise a significant portion of the active urban surfaces, and thus the resulting two-dimensional representation of LST/DLST is an incomplete dataset. Hence, the development of LST/DLST products that describe the true thermal status of the urban surface is required (e.g. such as the *complete urban temperatures* [119, 141]). To that end, remotely sensed LST/DLST image data may be able to provide the basis for the production of such a dataset.

5.4 Outlook

Recent advancements in TIR remote sensing provide the ability to utilise previously unsuitable Earth Observation datasets to scientific investigations that have special

requirements in spatial and temporal resolution. Such an advancement is the statistical downscaling of geostationary LST data, the primary function of which, is to disaggregate coarse-resolution LST into its finer-resolution components. In addition, the increasing availability of long global time series of remote sensing data drives the development of a new generation of methods for time series analysis. The wealth of information that can be made available can support the development of new data products, especially over urban areas where the majority of the world population resides, while the new methods can facilitate the study of past and present events from local through global scales. To that end the new generation of geostationary satellites, e.g. the Meteosat Third Generation Flexible Combined Imager (MTG-FCI) and the Geostationary Operational Environmental Satellite-R Series (GOES-R), offer increased capabilities that will open new research opportunities for scientists and researchers.

Bibliography

[1] Z.-L. Li et al. "Satellite-derived land surface temperature: Current status and perspectives". In: *Remote Sensing of Environment* 131 (2013), pp. 14–37. DOI: 10.1016/j.rse.2012.12.008.

[2] T. R. Oke. *Boundary layer climates*. 2nd. London: Taylor and Francis, 1987, p. 460. ISBN: 0203407210.

[3] A. B. Kahle. "Surface emittance, temperature, and thermal inertia derived from Thermal Infrared Multispectral Scanner (TIMS) data for Death Valley, California". In: *Geophysics* 52.7 (1987), pp. 858–874. DOI: 10.1190/1.1442357.

[4] H. R. Holbo and J. C. Luvall. "Modeling surface temperature distributions in forest landscapes". In: *Remote Sensing of Environment* 27.1 (1989), pp. 11–24. DOI: 10.1016/0034-4257(89)90033-3.

[5] Y. H. Kerr et al. "Land surface temperature retrieval techniques and applications". In: *Thermal remote sensing in land surface processes*. Ed. by D. A. Quattrochi and J. C. Luvall. Boca Raton, Florida: CRC Press, 2004. Chap. 2, pp. 33–109.

[6] D. A. Quattrochi and N. S. Goel. "Spatial and temporal scaling of thermal infrared remote sensing data". In: *Remote Sensing Reviews* 12.3-4 (1995), pp. 255–286. DOI: 10.1080/02757259509532287.

[7] T. J. Schmugge. *52: Estimation of Surface Temperature and Surface Emissivity*. Vol. 2. Chichester, UK: John Wiley & Sons, 2006, pp. 771–781. ISBN: 0471491039. DOI: 10.1002/0470848944.

[8] D. A. Roberts et al. "Relationships between dominant plant species, fractional cover and Land Surface Temperature in a Mediterranean ecosystem". In: *Remote Sensing of Environment* 167 (2015), pp. 152–167. DOI: 10.1016/j.rse.2015.01.026.

[9] J. C. Luvall and H. R. Holbo. "Measurements of short-term thermal responses of coniferous forest canopies using thermal scanner data". In: *Remote Sensing of Environment* 27.1 (1989), pp. 1–10. DOI: 10.1016/0034-4257(89)90032-1.

[10] J. C. Luvall and H. R. Holbo. "Thermal remote sensing methods in landscape ecology". In: *Quantitative Methods in Landscape Ecology*. Ed. by M. G. Turner and R. H. Gardner. 1st ed. New York: Springer-Verlag New York, 1991. Chap. 6, pp. 127–152. ISBN: 978-0-387-94241-4.

[11] J. C. Luvall et al. "The use of ATLAS data to quantify surface radiative budget alteration through urbanization for San Juan, Puerto Rico". In: *SPIE Remote Sensing for Agriculture, Ecosystems, and Hydrology VIII*. Vol. 6359. Stockholm, Sweden: SPIE Publications, 2006, 63590A. DOI: 10.1117/12.689124.

[12] J. C. Luvall et al. "BOUNDARY LAYER (ATMOSPHERIC) AND AIR POLLUTION | Urban Heat Islands". In: *Encyclopedia of Atmospheric Sciences*. Ed. by G. R. North, J. Pyle, and F. B. Zhang. 2nd. Oxford: Academic Press, 2015, pp. 310–318. ISBN: 978-0-12-382225-3.

[13] J. A. Voogt and T. Oke. "Thermal remote sensing of urban climates". In: *Remote Sensing of Environment* 86.3 (2003), pp. 370–384. DOI: 10.1016/S0034-4257(03)00079-8.

[14] D. Ghent et al. "Assimilation of land surface temperature into the land surface model JULES with an ensemble Kalman filter". In: *Journal of Geophysical Research Atmospheres* 115.19 (2010), pp. 1–16. DOI: 10.1029/2010JD014392.

[15] D. E. Comarazamy et al. "Climate impacts of land-cover and land-use changes in tropical islands under conditions of global climate change". In: *Journal of Climate* 26.5 (2013), pp. 1535–1550. DOI: 10.1175/JCLI-D-12-00087.1.

[16] D. E. Comarazamy, J. E. González, and J. C. Luvall. "Quantification and mitigation of long-term impacts of urbanization and climate change in the tropical coastal city of San Juan, Puerto Rico". In: *International Journal of Low-Carbon Technologies* 10.1 (2015), pp. 87–97. DOI: 10.1093/ijlct/ctt059.

[17] J. Townshend et al. "The 1 km resolution global data set: needs of the International Geosphere Biosphere Programme". In: *International Journal of Remote Sensing* 15.17 (1994), pp. 3417–3441. DOI: 10.1080/01431169408954338.

[18] A. J. Prata et al. "Thermal remote sensing of land surface temperature from satellites: Current status and future prospects". In: *Remote Sensing Reviews* 12.3-4 (1995), pp. 175–224. DOI: 10.1080/02757259509532285.

[19] T. M. Lillesand, R. W. Kiefer, and J. W. Chipman. *Remote sensing and image interpretation*. 6th. New York: John Wiley and Sons, 2008, p. 756. ISBN: 0471026093.

[20] J. B. Campbell and R. H. Wynne. *Introduction to remote sensing*. 5th. New York: The Guilford Press, 2011, p. 718. ISBN: 9781609181765.

[21] F. Becker and Z.-L. Li. "Surface Temperature and Emissivity at Various Scales: Definition, Measurement and Related Problems". In: *Remote Sensing Reviews* 12 (1995), pp. 225–253. DOI: 10.1080/02757259509532286.

[22] J. M. Norman and F. Becker. "Terminology in thermal infrared remote sensing of natural surfaces". In: *Agricultural and Forest Meteorology* 77.3-4 (1995), pp. 153–166. DOI: 10.1016/0168-1923(95)02259-Z.

[23] C. Elachi and J. J. van Zyl. *Introduction to the Physics and Techniques of Remote Sensing*. 2nd. Hoboken, New Jersey: Wiley-Interscience, 2006, p. 616. ISBN: 0471475696.

[24] K.-N. Liou. *An Introduction to Atmospheric Radiation*. 2nd. San Diego: Academic Press, 2002, p. 583. ISBN: 0124514510.

[25] R. A. Schowengerdt. *Remote Sensing: Models and Methods for Image Processing*. 3rd. London, UK: Academic Press, 2006, p. 560. ISBN: 0123694078.

[26] G. Thomas and K. Stamnes. *Radiative Transfer in the Atmosphere and Ocean*. Cambridge, United Kingdom: Cambridge University Press, 2012, p. 517.

[27] Z.-L. Li et al. "Land surface emissivity retrieval from satellite data". In: *International Journal of Remote Sensing* 34.9-10 (2013), pp. 3084–3127. DOI: 10.1080/01431161.2012.716540.

[28] F. J. Kelly. "On Kirchoff's Law and It's Generalized Application to Absorption and Emission by Cavities". In: *Journal of Research of the national Bureau of Standards - B. Mathematics and Mathematical Physics* 69.3 (1965), pp. 165–171. DOI: doi:10.2514/6.1965-135.

[29] G. C. Hulley, S. J. Hook, and A. M. Baldridge. "Validation of the North American ASTER Land Surface Emissivity Database (NAALSED) version 2.0 using pseudo-invariant sand dune sites". In: *Remote Sensing of Environment* 113.10 (2009), pp. 2224–2233. DOI: 10.1016/j.rse.2009.06.005.

[30] Z. Wan and J. Dozier. "A Generalized Split-Window Algorithm for Retrieving Land-Surface Temperature from Space". In: *IEEE Transactions on Geoscience and Remote Sensing* 34.4 (1996), pp. 892–905. DOI: 10.1109/36.508406.

[31] J. M. Wallace and P. V. Hobbs. *Atmospheric Science: An introductory survey*. 2nd. San Diego: Academic Press, 2006, p. 504. ISBN: 9780127329512.

[32] J. A. Shaw and P. W. Nugent. "Physics principles in radiometric infrared imaging of clouds in the atmosphere". In: *European Journal of Physics* 34.6 (2013), S111. ISSN: 0143-0807. DOI: 10.1088/0143-0807/34/6/S111.

[33] D. G. Andrews. *An Introduction to Atmospheric Physics*. 2nd. Cambridge: Cambridge University Publications, 2010, p. 248. ISBN: 9780521872201.

[34] V. G. Kunde et al. "The Nimbus 4 infrared spectroscopy experiment: 2. Comparison of observed and theoretical radiances from 425 - 1450 cm^{-1}". In: *Journal of Geophysical Research* 79.6 (1974), pp. 777–784. ISSN: 2156-2202. DOI: 10.1029/JC079i006p00777.

[35] Z. Qin et al. "Derivation of split window algorithm and its sensitivity analysis for retrieving land surface temperature from NOAA-advanced very high resolution radiometer data". In: *Journal of Geophysical Research: Atmospheres* 106.D19 (2001), pp. 22655–22670.

[36] P. Dash et al. "Land surface temperature and emissivity estimation from passive sensor data: Theory and practice-current trends". In: *International Journal of Remote Sensing* 23.13 (2002), pp. 4511–4518. DOI: 10.1080/01431160210146659.

[37] G. B. Franc and A. P. Cracknell. "Retrieval of land and sea surface temperature using NOAA-11 AVHRR data in north-eastern Brazil". In: *International Journal of Remote Sensing* 15.September (1994), pp. 1695–1712. DOI: 10.1080/01431169408954201.

[38] G. C. Hulley, C. G. Hughes, and S. J. Hook. "Quantifying uncertainties in land surface temperature and emissivity retrievals from ASTER and MODIS thermal infrared data". In: *Journal of Geophysical Research* 117.D23 (2012), p. D23113. DOI: 10.1029/2012JD018506.

[39] Z. Mitraka et al. "Improving the estimation of urban surface emissivity based on sub-pixel classification of high resolution satellite imagery". In: *Remote Sensing of Environment* 117 (2012), pp. 125–134. DOI: 10.1016/j.rse.2011.06.025.

[40] W. C. Snyder et al. "Classification-based emissivity for land surface temperature measurement from space". In: *International Journal of Remote Sensing* 19.14 (1998), pp. 2753–2774. DOI: 10.1080/014311698214497.

[41] Z. Qin, A. Karnieli, and P. Berliner. "A mono-window algorithm for retrieving land surface temperature from Landsat TM data and its application to the Israel-Egypt border region". In: *International Journal of Remote Sensing* 22.18 (2001), pp. 3719–3746. DOI: 10.1080/01431160010006971.

[42] J. C. Jiménez-Muñoz and J. A. Sobrino. "A generalized single-channel method for retrieving land surface temperature from remote sensing data". In: *Journal of Geophysical Research* 108.D22 (2003), p. 4688. DOI: 10.1029/2003JD003480.

[43] M. Atitar and J. A. Sobrino. "A split-window algorithm for estimating LST from Meteosat 9 data: Test and comparison with in situ data and MODIS LSTs". In: *IEEE Geoscience and Remote Sensing Letters* 6.1 (2009), pp. 122–126.

[44] D. Sun and R. T. Pinker. "Estimation of land surface temperature from a Geostationary Operational Environmental Satellite (GOES-8)". In: *Journal of Geophysical Research* 108.D11 (2003), p. 4326. DOI: 10.1029/2002JD002422.

[45] D. Sun and R. T. Pinker. "Retrieval of surface temperature from the MSG-SEVIRI observations: Part I. Methodology". In: *International Journal of Remote Sensing* 28.23 (2007), pp. 5255–5272. DOI: 10.1080/01431160701253246.

[46] A. Gillespie et al. "A temperature and emissivity separation algorithm for Advanced Spaceborne Thermal Emission and Reflection Radiometer (ASTER) images". In: *IEEE Transactions on Geoscience and Remote Sensing* 36.4 (1998), pp. 1113–1126. DOI: 10.1109/36.700995.

[47] G. C. Hulley, S. Veraverbeke, and S. J. Hook. "Thermal-based techniques for land cover change detection using a new dynamic MODIS multispectral emissivity product (MOD21)". In: *Remote Sensing of Environment* 140 (2014), pp. 755–765. DOI: 10.1016/j.rse.2013.10.014.

[48] G. C. Hulley et al. *Moderate Resolution Imaging Spectroradiometer (MODIS) MOD21 Land Surface Temperature and Emissivity Algorithm Theoretical Basis Document*. Tech. rep. Pasadena, California, USA: Jet Propulsion Laboratory, California Institute of Technology, 2016, p. 102.

[49] A. P. Cracknell. "Synergy in remote sensing - what is in a pixel?" In: *International Journal of Remote Sensing* 19.11 (1998), pp. 2025–2047. DOI: 10.1080/014311698214848.

[50] A. H. Strahler, C. E. Woodcock, and J. A. Smith. "On the nature of models in remote sensing". In: *Remote Sensing of Environment* 20.2 (1986), pp. 121–139. DOI: 10.1016/0034-4257(86)90018-0.

[51] J. Wu and H. Li. "Concepts of scale and scaling". In: *Scaling and Uncertainty Analysis in Ecology: Methods and Applications*. Ed. by J. Wu et al. Dordrecht, The Netherlands: Springer, 2006. Chap. 1, pp. 3–15. DOI: 10.1007/1-4020-4663-4.

[52] W. Zhan et al. "Disaggregation of remotely sensed land surface temperature: A new dynamic methodology". In: *Journal of Geophysical Research: Atmospheres* 121 (2016), pp. 1–17. DOI: 10.1002/2016JD024891.

[53] W. Zhan et al. "Disaggregation of remotely sensed land surface temperature: Literature survey, taxonomy, issues, and caveats". In: *Remote Sensing of Environment* 131.19 (2013), pp. 119–139. ISSN: 00344257. DOI: 10.1016/j.rse.2012.12.014.

[54] M. Stathopoulou and C. Cartalis. "Downscaling AVHRR land surface temperatures for improved surface urban heat island intensity estimation". In: *Remote Sensing of Environment* 113.12 (2009), pp. 2592–2605. DOI: 10.1016/j.rse.2009.07.017.

[55] K. Zakšek and K. Oštir. "Downscaling land surface temperature for urban heat island diurnal cycle analysis". In: *Remote Sensing of Environment* 117 (2012), pp. 114–124. DOI: 10.1016/j.rse.2011.05.027.

[56] I. Keramitsoglou, C. T. Kiranoudis, and Q. Weng. "Downscaling Geostationary Land Surface Temperature Imagery for Urban Analysis". In: *IEEE Geoscience and Remote Sensing Letters* 10.5 (2013), pp. 1253–1257. DOI: 10.1109/LGRS.2013.2257668.

[57] F. M. Göttsche and F. S. Olesen. "Modelling the effect of optical thickness on diurnal cycles of land surface temperature". In: *Remote Sensing of Environment* 113.11 (2009), pp. 2306–2316. DOI: 10.1016/j.rse.2009.06.006.

[58] F. M. Göttsche and F. S. Olesen. "Modelling of diurnal cycles of brightness temperature extracted from meteosat data". In: *Remote Sensing of Environment* 76.3 (2001), pp. 337–348. DOI: 10.1016/S0034-4257(00)00214-5.

[59] B. Bechtel. "A New Global Climatology of Annual Land Surface Temperature". In: *Remote Sensing* 7.3 (2015), pp. 2850–2870. ISSN: 2072-4292. DOI: 10.3390/rs70302850.

[60] J. Schmetz et al. "An introduction to Meteosat Second Generation (MSG)". In: *Bulletin of the American Meteorological Society* 83.7 (2002), pp. 977–992. DOI: 10.1175/BAMS-83-7-Schmetz-1.

[61] D. M. Aminou. *MSG 's SEVIRI Instrument*. Tech. rep. Noordwijk, The Netherlands, 2002, pp. 15–17.

[62] P. Sismanidis et al. "Improving the Downscaling of Diurnal Land Surface Temperatures Using the Annual Cycle Parameters as Disaggregation Kernels". In: *Remote Sensing* 9.1 (2017), p. 23. DOI: 10.3390/rs9010023.

[63] P. Sismanidis et al. "Assessing the Capability of a Downscaled Urban Land Surface Temperature Time Series to Reproduce the Spatiotemporal Features of the Original Data". In: *Remote Sensing* 8.4 (2016), p. 274. DOI: 10.3390/rs8040274.

[64] P. Sismanidis et al. "Mapping the Spatiotemporal Dynamics of Europe's Land Surface Temperatures". In: *IEEE Geoscience and Remote Sensing Letters* 15.2 (2018), pp. 202–206. DOI: 10.1109/LGRS.2017.2779829.

[65] W. Zhan et al. "Sharpening thermal imageries: A generalized theoretical framework from an assimilation perspective". In: *IEEE Transactions on Geoscience and Remote Sensing* 49.2 (2011), pp. 773–789. DOI: 10.1109/TGRS.2010.2060342.

[66] W. R. Tobler. "A Computer Movie Simulating Urban Growth in the Detroit Region". In: *Economic Geography* 46 (1970), pp. 234–240. DOI: 10.2307/143141.

[67] Y. Chen et al. "Disaggregation of Remotely Sensed Land Surface Temperature : A Generalized Paradigm". In: *IEEE Transactions on Geoscience and Remote Sensing* 52.9 (2014), pp. 5952–5965. DOI: 10.1109/TGRS.2013.2294031.

[68] A. K. Inamdar and A. French. "Disaggregation of GOES land surface temperatures using surface emissivity". In: *Geophysical Research Letters* 36.2 (2009), pp. 1–5. DOI: 10.1029/2008GL036544.

[69] S.-b. Duan and Z.-l. Li. "Spatial Downscaling of MODIS Land Surface Temperatures Using Geographically Weighted Regression : Case Study in Northern China". In: *IEEE Transactions on Geoscience and Remote Sensing* 54.11 (2016), pp. 6458 –6469. DOI: 10.1109/TGRS.2016.2585198.

[70] C. Jeganathan et al. "Evaluating a thermal image sharpening model over a mixed agricultural landscape in India". In: *International Journal of Applied Earth Observation and Geoinformation* 2 (), pp. 178–191. DOI: 10.1016/j.jag.2010.11.001.

[71] D. Sun and M. Kafatos. "Note on the NDVI-LST relationship and the use of temperature-related drought indices over North America". In: *Geophysical Research Letters* 34.24 (2007), pp. 1–4. ISSN: 00948276. DOI: 10.1029/2007GL031485.

[72] F. Yuan and M. E. Bauer. "Comparison of impervious surface area and normalized difference vegetation index as indicators of surface urban heat island effects in Landsat imagery". In: *Remote Sensing of Environment* 106.3 (2007), pp. 375–386. ISSN: 00344257. DOI: 10.1016/j.rse.2006.09.003.

[73] W. P. Kustas et al. "Estimating subpixel surface temperatures and energy fluxes from the vegetation index–radiometric temperature relationship". In: *Remote Sensing of Environment* 85.4 (2003), pp. 429–440. DOI: 10.1016/S0034-4257(03)00036-1.

[74] N. Agam et al. "A vegetation index based technique for spatial sharpening of thermal imagery". In: *Remote Sensing of Environment* 107.4 (2007), pp. 545–558. ISSN: 00344257. DOI: 10.1016/j.rse.2006.10.006.

[75] W. Essa et al. "Evaluation of the DisTrad thermal sharpening methodology for urban areas". In: *International Journal of Applied Earth Observation and Geoinformation* 19.1 (2012), pp. 163–172. DOI: 10.1016/j.jag.2012.05.010.

[76] A. Dominguez et al. "High-resolution urban thermal sharpener (HUTS)". In: *Remote Sensing of Environment* 115.7 (2011), pp. 1772–1780. DOI: 10.1016/j.rse.2011.03.008.

[77] O. Merlin et al. "Disaggregation of MODIS surface temperature over an agricultural area using a time series of Formosat-2 images". In: *Remote Sensing of Environment* 114.11 (2010), pp. 2500–2512. DOI: 10.1016/j.rse.2010.05.025.

[78] Q. Weng and P. Fu. "Modeling diurnal land temperature cycles over Los Angeles using downscaled GOES imagery". In: *ISPRS Journal of Photogrammetry and Remote Sensing* 97 (2014), pp. 78–88. ISSN: 09242716. DOI: 10.1016/j.isprsjprs.2014.08.009.

[79] C. Hutengs and M. Vohland. "Downscaling land surface temperatures at regional scales with random forest regression". In: *Remote Sensing of Environment* 178 (2016), pp. 127–141. DOI: 10.1016/j.rse.2016.03.006.

[80] B. Bechtel. "Robustness of Annual Cycle Parameters to Characterize the Urban Thermal Landscapes". In: *IEEE Geoscience and Remote Sensing Letters* 9.5 (2012), pp. 876–880. ISSN: 1545-598X. DOI: 10.1109/LGRS.2012.2185034.

[81] B. Bechtel and P. Sismanidis. "Time Series Analysis of Moderate Resolution Land Surface Temperatures". In: *Remote Sensing Time Series Image Processing*. Ed. by Q. Weng. CRC Press, 2018. Chap. 5, pp. 89–120. ISBN: 9781138054592.

[82] B. Bechtel, K. Zakšek, and G. Hoshyaripour. "Downscaling Land Surface Temperature in an Urban Area: A Case Study for Hamburg, Germany". In: *Remote Sensing* 4.12 (2012), pp. 3184–3200. ISSN: 2072-4292. DOI: 10.3390/rs4103184.

[83] Z. Wan. *Collection-5 MODIS Land Surface Temperature Products: Users' Guide*. Tech. rep. California, United States: ICESS, University of California, Santa Barbara, 2006, p. 30.

[84] Z. Wan and Z.-l. Li. "Radiance-based validation of the V5 MODIS land-surface temperature product". In: *International Journal of Remote Sensing* 29.17-18 (2008), pp. 5373–5395. DOI: 10.1080/01431160802036565.

[85] P. Sismanidis, I. Keramitsoglou, and C. T. Kiranoudis. "Evaluating the Operational Retrieval and Downscaling of Urban Land Surface Temperatures". In: *IEEE Geoscience and Remote Sensing Letters* 12.6 (2015), pp. 1312–1316. DOI: 10.1109/LGRS.2015.2397450.

[86] P. Sismanidis, I. Keramitsoglou, and C. T. Kiranoudis. "A Satellite-based System for Continuous Monitoring of Surface Urban Heat Islands". In: *Urban Climate* 14 (2015), pp. 141–153. DOI: 10.1016/j.uclim.2015.06.001.

[87] I. F. Trigo et al. "The Satellite Application Facility for Land Surface Analysis". In: *International Journal of Remote Sensing* 32.10 (2011), pp. 2725–2744. DOI: 10.1080/01431161003743199.

[88] G. C. Hulley and S. J. Hook. "Intercomparison of versions 4, 4.1 and 5 of the MODIS Land Surface Temperature and Emissivity products and validation with laboratory measurements of sand samples from the Namib desert, Namibia". In: *Remote Sensing of Environment* 113.6 (2009), pp. 1313–1318. DOI: 10.1016/j.rse.2009.02.018.

[89] B. Rabus et al. "The shuttle radar topography mission - A new class of digital elevation models acquired by spaceborne radar". In: *ISPRS Journal of Photogrammetry and Remote Sensing* 57.4 (2003), pp. 241–262. DOI: 10.1016/S0924-2716(02)00124-7.

[90] R. Solano et al. *Collection-5 MODIS Vegetation Indices (MOD13): User's Guide*. Tech. rep. Arizona, United States: University of Arizona, 2010, p. 38.

[91] A. H. Strahler and J. P. Muller. *MODIS BRDF Albedo Product: Algorithm Theoretical Basis Document*. Tech. rep. Boston, MA, United States: Boston University, 1999, p. 53.

[92] E. E. Maeda. "Downscaling MODIS LST in the East African mountains using elevation gradient and land-cover information". In: *International Journal of Remote Sensing* 35.9 (2014), pp. 3094–3108. DOI: 10.1080/01431161.2014.903442.

[93] M. Bisquert, J. M. Sánchez, and V. Caselles. "Evaluation of Disaggregation Methods for Downscaling MODIS Land Surface Temperature to Landsat Spatial Resolution in Barrax Test Site". In: *IEEE Journal of Selected Topics in Applied Earth Observations and Remote Sensing* 9.4 (2016), pp. 1430–1438. DOI: 10.1109/JSTARS.2016.2519099.

[94] T. Holderness et al. "An evaluation of thermal Earth observation for characterizing urban heatwave event dynamics using the urban heat island intensity metric". In: *International Journal of Remote Sensing* 34.3 (2013), pp. 864–884. DOI: 10.1080/01431161.2012.714505.

[95] K. Y. Vinnikov et al. "Angular anisotropy of satellite observations of land surface temperature". In: *Geophysical Research Letters* 39.23 (2012), pp. 1–7. DOI: 10.1029/2012GL054059.

[96] L. Hu et al. "A first satellite-based observational assessment of urban thermal anisotropy". In: *Remote Sensing of Environment* 181 (2016), pp. 111–121. DOI: 10.1016/j.rse.2016.03.043.

[97] I. F. Trigo et al. "An assessment of remotely sensed land surface temperature". In: *Journal of Geophysical Research* 113 (2008), p. D17108. DOI: 10.1029/2008JD010035.

[98] E. Kalnay and M. Cai. "Impact of urbanization and land-use change on climate." In: *Nature* 423.6939 (2003), pp. 528–531. DOI: 10.1038/nature01675.

[99] K. Braganza, D. J. Karoly, and J. M. Arblaster. "Diurnal temperature range as an index of global climate change during the twentieth century". In: *Geophysical Research Letters* 31.13 (2004), pp. 2–5. DOI: 10.1029/2004GL019998.

[100] J. D. Kalma, T. R. McVicar, and M. F. McCabe. "Estimating land surface evaporation: A review of methods using remotely sensed surface temperature data". In: *Surveys in Geophysics* 29.4-5 (2008), pp. 421–469. DOI: 10.1007/s10712-008-9037-z.

[101] S. B. Idso et al. "The Utility of Surface Temperature Measurements for the Remote Sensing of Surface Soil Water Status". In: *Journal of Geophysical Research* 80.21 (1978), pp. 3044–3049. DOI: 10.1029/JC080i021p03044.

[102] L. Nguyen and G. Henebry. "Urban Heat Islands as Viewed by Microwave Radiometers and Thermal Time Indices". In: *Remote Sensing* 8.10 (2016), p. 831. DOI: 10.3390/rs8100831.

[103] D. B. Lobell. "Changes in diurnal temperature range and national cereal yields". In: *Agricultural and Forest Meteorology* 145.3-4 (2007), pp. 229–238. DOI: 10.1016/j.agrformet.2007.05.002.

[104] H. Kan et al. "Diurnal temperature range and daily mortality in Shanghai, China". In: *Environmental Research* 103.3 (2007), pp. 424–431. DOI: 10.1016/j.envres.2006.11.009.

[105] F. Gao, W. P. Kustas, and M. C. Anderson. "A data mining approach for sharpening thermal satellite imagery over land". In: *Remote Sensing* 4.11 (2012), pp. 3287–3319. DOI: 10.3390/rs4113287.

[106] J. Verbesselt, A. Zeileis, and M. Herold. "Near real-time disturbance detection using satellite image time series". In: *Remote Sensing of Environment* 123 (2012), pp. 98–108. DOI: 10.1016/j.rse.2012.02.022.

[107] J. Tan et al. "The urban heat island and its impact on heat waves and human health in Shanghai". In: *International journal of biometeorology* 54.1 (2010), pp. 75–84. DOI: 10.1007/s00484-009-0256-x.

[108] C. P. Lo, D. A. Quattrochi, and J. C. Luvall. "Application of high-resolution thermal infrared remote sensing and GIS to assess the urban heat island effect". In: *International Journal of Remote Sensing* 18.2 (2010), pp. 287–304. DOI: 10.1080/014311697219079.

[109] I. Keramitsoglou et al. "Identification and analysis of urban surface temperature patterns in Greater Athens, Greece, using MODIS imagery". In: *Remote Sensing of Environment* 115.12 (2011), pp. 3080–3090. DOI: 10.1016/j.rse.2011.06.014.

[110] M. Bisquert et al. "Estimating high resolution evapotranspiration from disaggregated thermal images". In: *Remote Sensing of Environment* 187 (2016), pp. 423–433. DOI: 10.1016/j.rse.2016.10.049.

[111] L. Anselin. "Local indicators of spatial association - LISA". In: *Geographical Analysis* 27.2 (1995), pp. 93–115. DOI: 10.1111/j.1538-4632.1995.tb00338.x.

[112] J. H. Friedman. "Greedy Function Approximation: A gradient Boosting Machine". In: *The Annals of Statistics* 29.5 (2001), pp. 1189–1232. DOI: 10.1214/aos/1013203451.

[113] T. Joachims. *Making Large-Scale SVM Learning Practical*. Tech. rep. 1999, pp. 41–56. DOI: 10.1109/ICEMI.2009.5274151.

[114] C.-C. Chang and C.-J. Lin. "LIBSVM: A Library for Support Vector Machines". In: *ACM Transactions on Intelligent Systems and Technology* 2.3 (2011), p. 27. DOI: 10.1145/1961189.1961199.

[115] V. Vapnik. *The nature of statistical learning theory*. New York: Springer, 1995, p. 314. DOI: 10.1007/978-1-4757-3264-1.

[116] G. Mountrakis, J. Im, and C. Ogole. "Support vector machines in remote sensing: A review". In: *ISPRS Journal of Photogrammetry and Remote Sensing* 66.3 (2010), pp. 259–247. DOI: 10.1016/j.isprsjprs.2010.11.001.

[117] A. Natekin and A. Knoll. "Gradient boosting machines, a tutorial". In: *Frontiers in Neurorobotics* 7 (2013), p. 21. DOI: 10.3389/fnbot.2013.00021.

[118] O. Arino et al. "GlobCover: ESA service for Global Land Cover from MERIS". In: *Geoscience and Remote Sensing Symposium*. Barcelona, Spain: IEEE, 2007, pp. 2412–2415. DOI: 10.1109/IGARSS.2007.4423328.

[119] J. A. Voogt and T. R. Oke. "Complete urban surface temperatures". In: *Journal of Applied Meteorology* 36 (1997), pp. 1117–1132.

[120] R. Fabrizi, S. Bonafoni, and R. Biondi. "Satellite and ground-based sensors for the Urban Heat Island analysis in the city of Rome". In: *Remote Sensing* 2 (2010), pp. 1400–1415. DOI: 10.3390/rs2051400.

[121] S. Muster et al. "Spatio-temporal sensitivity of MODIS land surface temperature anomalies indicates high potential for large-scale land cover change detection in Arctic permafrost landscapes". In: *Remote Sensing of Environment* 168 (2015), pp. 1–12. DOI: 10.1016/j.rse.2015.06.017.

[122] R. Van De Kerchove et al. "Spatio-temporal variability in remotely sensed land surface temperature, and its relationship with physiographic variables in the Russian Altay Mountains". In: *International Journal of Applied Earth Observation and Geoinformation* 20.1 (2013), pp. 4–19. DOI: 10.1016/j.jag.2011.09.007.

[123] G.-Y. Yang and J. Slingo. "The Diurnal Cycle in the Tropics". In: *Monthly Weather Review* 129.4 (2001), pp. 784–801. DOI: 10.1175/1520-0493(2001)129<0784:TDCITT>2.0.CO;2.

[124] A. K. Inamdar et al. “Land surface temperature retrieval at high spatial and temporal resolutions over the southwestern United States”. In: *Journal of Geophysical Research* 113.D7 (2008), pp. 1–18. DOI: 10.1029/2007JD009048.

[125] S.-B. Duan et al. “Estimation of Diurnal Cycle of Land Surface Temperature atHigh Temporal and Spatial Resolution from Clear-Sky MODISData”. In: *Remote Sensing* 6.4 (2014), pp. 3247–3262. DOI: 10.3390/rs6043247.

[126] J. Quan et al. “A hybrid method combining neighborhood information from satellite data with modeled diurnal temperature cycles over consecutive days”. In: *Remote Sensing of Environment* 155 (2014), pp. 257–274. DOI: j.rse.2014.08.034.

[127] A. Soliman et al. “Pan-Arctic Land Surface Temperature from MODIS and AATSR: Product Development and Intercomparison”. In: *Remote Sensing* 4.12 (2012), pp. 3833–3856. DOI: 10.3390/rs4123833.

[128] P. Fu and Q. Weng. “Temporal Dynamics of Land Surface Temperature From Landsat TIR Time Series Images”. In: *IEEE Geoscience and Remote Sensing Letters* 12.10 (2015), pp. 2175–2179. DOI: 10.1109/Lgrs.2015.2455019.

[129] F. Huang et al. “Temporal upscaling of surface urban heat island by incorporating an annual temperature cycle model: A tale of two cities”. In: *Remote Sensing of Environment* 186 (2016), pp. 1–12. DOI: 10.1016/j.rse.2016.08.009.

[130] B. Bechtel. “Multitemporal Landsat data for urban heat island assessment and classification of local climate zones”. In: *Proceedings of the Joint Urban Remote Sensing Event*. Munich, Germany: IEEE, 2011, pp. 129–132. DOI: 10.1109/JURSE.2011.5764736.

[131] S. B. Duan et al. “Evaluation of six land-surface diurnal temperature cycle models using clear-sky in situ and satellite data”. In: *Remote Sensing of Environment* 124 (2012), pp. 15–25. DOI: 10.1016/j.rse.2012.04.016.

[132] F. Gao et al. “On the blending of the landsat and MODIS surface reflectance: Predicting daily Landsat surface reflectance”. In: *IEEE Transactions on Geoscience and Remote Sensing* 44.8 (2006), pp. 2207–2218. DOI: 10.1109/TGRS.2006.872081.

[133] P. Wu et al. "Integrated fusion of multi-scale polar-orbiting and geostationary satellite observations for the mapping of high spatial and temporal resolution land surface temperature". In: *Remote Sensing of Environment* 156 (2015), pp. 169–181. DOI: 10.1016/j.rse.2014.09.013.

[134] Q. Weng, P. Fu, and F. Gao. "Generating daily land surface temperature at Landsat resolution by fusing Landsat and MODIS data". In: *Remote Sensing of Environment* 145 (2014), pp. 55–67. DOI: 10.1016/j.rse.2014.02.003.

[135] B. Huang et al. "Generating High Spatiotemporal Resolution Land Surface Temperature for Urban Heat Island Monitoring". In: *IEEE Geoscience and Remote Sensing Letters* 10.5 (2013), pp. 1011–1015. DOI: 10.1109/LGRS.2012.2227930.

[136] S. C. Freitas et al. "Quantifying the uncertainty of land surface temperature retrievals from SEVIRI/Meteosat". In: *IEEE Transactions on Geoscience and Remote Sensing* 48.1 (2010), pp. 523–534.

[137] S.-B. Duan et al. "Generation of a time-consistent land surface temperature product from MODIS data". In: *Remote Sensing of Environment* 140 (2014), pp. 339–349. DOI: 10.1016/j.rse.2013.09.003.

[138] B. Bechtel. "The Climate of The Canary Islands by Annual Cycle Parameters". In: *ISPRS - International Archives of the Photogrammetry, Remote Sensing and Spatial Information Sciences* XLI-B8 (2016), pp. 243–250. DOI: 10.5194/isprs-archives-XLI-B8-243-2016.

[139] J. Quan et al. "An integrated model for generating hourly Landsat-like land surface temperatures over heterogeneous landscapes". In: *Remote Sensing of Environment* 206.March (2018), pp. 403–423. DOI: 10.1016/j.rse.2017.12.003.

[140] I. Keramitsoglou et al. "An Online System for Nowcasting Satellite Derived Temperatures for Urban Areas". In: *Remote Sensing* 8.4 (2016), p. 306. DOI: 10.3390/rs8040306.

[141] L. Jiang et al. "Remote estimation of complete urban surface temperature using only directional radiometric temperatures". In: *Building and Environment* 135.March (2018), pp. 224–236. DOI: 10.1016/j.buildenv.2018.03.005.

[142] P. Sismanidis, I. Keramitsoglou, and C. T. Kiranoudis. "Identifying and Characterising the Diurnal Evolution of Urban Land Surface Temperature Patterns". In: *Joint Urban Remote Sensing Event 2017*. Dubai, United Arab Emirates: IEEE, 2017, pp. 1–4. DOI: 10.1109/JURSE.2017.7924598.

[143] P. Sismanidis, I. Keramitsoglou, and C. T. Kiranoudis. "Diurnal Analysis of Surface Urban Heat Island Using Spatially Enhanced Satellite derived LST Data". In: *Joint Urban Remote Sensing Event 2015*. Lausanne, Switzerland: IEEE, 2015, pp. 13–16. DOI: 10.1109/JURSE.2015.7120498.

Appendix A

Brief Biography

Panagiotis Sismanidis holds an Engineering Diploma in Rural and Surveying Engineer (2012) from the National Technical University in Athens (NTUA). He works at the Institute for Astronomy, Astrophysics, Space Applications and Remote Sensing of the National Observatory of Athens since 2014, where he has participated in several research and civil protection projects funded by the European Commission and the Greek state. During April and May 2018 he was a visiting researcher at the Institute of Geography of the University of Hamburg in Germany. He has co-authored eleven journal articles (he is first author in seven of them), one book chapter and seven conference papers. Panagiotis is a reviewer in several remote sensing journals, including Remote Sensing of Environment and Remote Sensing; and is the recipient of two PhD educational grants from the A.G. Leventis Foundation (2016, 2017), one PhD grant from the German Academic Exchange Service (2018) and two awards, one from NTUA (2013) and one from the European Meteorological Society (2016).

Appendix B

List of Publications

The list below includes the publications related to this thesis. The complete list of publications of Panagiotis Sismanidis can be found using the ORCID: 0000-0003-2185-1034.

B.1 Journal Articles

1. P. Sismanidis et al. "Mapping the Spatiotemporal Dynamics of Europe's Land Surface Temperatures". In: *IEEE Geoscience and Remote Sensing Letters* 15.2 (2018), pp. 202–206. DOI: 10.1109/LGRS.2017.2779829

2. P. Sismanidis et al. "Improving the Downscaling of Diurnal Land Surface Temperatures Using the Annual Cycle Parameters as Disaggregation Kernels". In: *Remote Sensing* 9.1 (2017), p. 23. DOI: 10.3390/rs9010023

3. P. Sismanidis et al. "Assessing the Capability of a Downscaled Urban Land Surface Temperature Time Series to Reproduce the Spatiotemporal Features of the Original Data". In: *Remote Sensing* 8.4 (2016), p. 274. DOI: 10.3390/rs8040274

4. P. Sismanidis, I. Keramitsoglou, and C. T. Kiranoudis. "A Satellite-based System for Continuous Monitoring of Surface Urban Heat Islands". In: *Urban Climate* 14 (2015), pp. 141–153. DOI: 10.1016/j.uclim.2015.06.001

5. P. Sismanidis, I. Keramitsoglou, and C. T. Kiranoudis. "Evaluating the Operational Retrieval and Downscaling of Urban Land Surface Temperatures". In: *IEEE Geoscience and Remote Sensing Letters* 12.6 (2015), pp. 1312–1316. DOI: 10.1109/LGRS.2015.2397450

B.2 Book Chapters

1. B. Bechtel and P. Sismanidis. "Time Series Analysis of Moderate Resolution Land Surface Temperatures". In: *Remote Sensing Time Series Image Processing*. Ed. by Q. Weng. CRC Press, 2018. Chap. 5, pp. 89–120. ISBN: 9781138054592

B.3 Conference Proceedings

1. P. Sismanidis, I. Keramitsoglou, and C. T. Kiranoudis. "Identifying and Characterising the Diurnal Evolution of Urban Land Surface Temperature Patterns". In: *Joint Urban Remote Sensing Event 2017*. Dubai, United Arab Emirates: IEEE, 2017, pp. 1–4. DOI: 10.1109/JURSE.2017.7924598

2. P. Sismanidis, I. Keramitsoglou, and C. T. Kiranoudis. "Diurnal Analysis of Surface Urban Heat Island Using Spatially Enhanced Satellite derived LST Data". In: *Joint Urban Remote Sensing Event 2015*. Lausanne, Switzerland: IEEE, 2015, pp. 13–16. DOI: 10.1109/JURSE.2015.7120498